Title
Environmental Quenching in Clusters at High Redshift

Author
Foltz, Ryan

Publication Date
2017

UNIVERSITY OF CALIFORNIA
RIVERSIDE

Environmental Quenching in Clusters at High Redshift

A Dissertation submitted in partial satisfaction
of the requirements for the degree of

Doctor of Philosophy

in

Physics

by

Ryan Michael Foltz

December 2017

Dissertation Committee:

Dr. Gillian Wilson, Chairperson
Dr. Naveen Reddy
Dr. Laura Sales

The Dissertation of Ryan Michael Foltz is approved:

Committee Chairperson

University of California, Riverside

Acknowledgments

I am humbled to acknowledge those who have made this work possible through their kindness and support, and those who took a chance on me and gave me an opportunity to succeed.

I'd like thank my family for their love and support.

I'd like to thank my advisor Gillian Wilson for her support and direction, for the opportunity she provided, and for the data. Thanks to my collaborators Andrew Degroot, Adam Muzzin, and Mike Cooper, who provided helpful advice and feedback on my research. Thanks to my undergraduate research advisor Rafael Garcia, for driving me to excel, and for instilling in me an appreciation for the finer points of physics. Thanks to my mentor, Steve Corman. Thanks to Naveen Reddy and Laura Sales for being members of my dissertation committee.

I'd like to thank Katie Curnyn, and my classmates Evan Sosenko, William Freeman, Kira Burt, Kennedy Elizabeth, Bobby Schafer, Irene Shivaei, Calvin Cordozar Broadus, Jr., and Shaolong Chen.

I'd like to thank the staff of the Chandra Director's Office: Harvey Tananbaum, Belinda Wilkes, Paul Green, Andrea Prestwich, and Nancy Evans. My life has been shaped dramatically by the opportunity they selflessly afforded me.

I especially thank all of my friends. Over the years they have fed and sheltered me, and enthusiastically believed in me. I could not have done this without them.

The data presented in this work were obtained at the W.M. Keck Observatory, which is operated as a scientific partnership among the California Institute of Technology,

the University of California and the National Aeronautics and Space Administration. The Observatory was made possible by the generous financial support of the W.M. Keck Foundation. I would like to recognize and acknowledge the very significant cultural role and reverence that the summit of Mauna Kea has always had within the indigenous Hawaiian community. We are most fortunate to have the opportunity to conduct observations from this mountain.

Dedicated to the memory of Greg Foltz

ABSTRACT OF THE DISSERTATION

Environmental Quenching in Clusters at High Redshift

by

Ryan Michael Foltz

Doctor of Philosophy, Graduate Program in Physics
University of California, Riverside, December 2017
Dr. Gillian Wilson, Chairperson

We present two studies of galaxy populations in cluster samples at $z \sim 1$ and $z \sim 1.5$ with the aim of constraining galaxy formation and evolutionary processes. We study the slope, intercept, and scatter of the color-magnitude relation in the ten clusters at z ∼ 1. The quiescent galaxies in these clusters formed the bulk of their stars above $z \gtrsim 3$ with an age spread $\Delta t \gtrsim 1$ Gyr. We measure the environmental quenching timescale t_Q in a sample of four galaxy clusters at $1.35 < z < 1.65$, and the $z \sim 1$ sample. We employ a "delayed-then-rapid" quenching model that relates a simulated cluster mass accretion rate to the observed numbers of each type of galaxy in the cluster to constrain t_Q. We find a quenching timescale of $t_Q = 1.24^{+0.23}_{-0.20}$ Gyr in the $z \sim 1.5$ cluster sample, and $t_Q = 1.50^{+0.19}_{-0.18}$ Gyr at $z \sim 1$. Using values drawn from the literature, we compare the redshift evolution of t_Q to timescales predicted for different physical quenching mechanisms. For galaxies of mass $M_* \gtrsim 10^{10.5}$ $M_\odot$, the environmental quenching timescale evolves faster from $z = 0$ to $z = 1.5$ than the gas depletion timescale and slower than an SFR-outflow timescale with mass-loading factor $\eta = 2.5$, but is consistent with the evolution of the dynamical time. This suggests that environmental quenching in these galaxies is driven by the motion of satellites relative to the cluster environment. We also find t_Q to depend on host halo mass such that quenching occurs over faster timescales in clusters relative to groups, further supporting the notion that kinematic mechanisms are responsible for quenching high-mass galaxies.

Contents

List of Figures

List of Tables

Chapter 1

Introduction

In recent years, the ΛCDM paradigm has emerged as the standard cosmological description of the universe. In this model, the dynamical aspects of structure formation are well-described by the purely gravitational collapse of dissipationless dark matter, which can be studied in large N-body simulations (e.g., Springel et al., 2005; Thomas & Couchman, 1992; Navarro et al., 1995; Weinberg et al., 2004). Dark matter (DM) haloes then evolve through hierarchical assembly, being built-up from successive mergers of smaller haloes over cosmological times. (Gott & Rees, 1975a; Press & Schechter, 1974; White & Rees, 1978; Blumenthal et al., 1984; Davis et al., 1985; White & Frenk, 1991; Barnes, 1992; Cole et al., 2000). Baryonic matter traces the DM distribution, forming the visible components of these structures.

The ΛCDM framework has enjoyed dramatic successes in accounting for the observed state of the universe, from the abundance and spatial distribution of the large-scale structures of the universe (clusters, voids, and filaments), to their emergence from the extremely smooth initial conditions indicated by the cosmic microwave background (CMB) (Springel et al., 2006), as well as the temperature anisotropy of the CMB (Narlikar & Padmanabhan, 2001, and references therein), and the abundances of the light elements.

On smaller, galactic scales (100 kpc), however, the consequences of this model are complicated by the dissipative physics of baryons: radiative cooling of gas, star formation, active galactic nucleus (AGN) feedback, and chemical enrichment and energy release from supernovae (SN) are poorly-understood processes, which are currently parameterized by ad hoc recipes in galaxy formation models. Consequently, the current generation of models have lacked a complete account of the build-up of stellar mass over cosmic time, and have difficulty matching the abundance of quenched galaxies (e.g. Weinmann et al., 2011; Vulcani et al., 2014) or the star formation rates of galaxies (e.g. Font et al., 2008b; Weinmann et al., 2010). Better observational constraints on the formation and evolution of galaxies are vitally important in order to complete the description of the relevant physics, from large-scale cosmology to small-scale astrophysics.

1.1 Some Observational Constraints on Galaxy Evolution

1.1.1 Quenching

An empirical description of galaxy evolution emerges from surveys of galaxy populations and clusters to high redshift. First among the salient facts is that galaxies form a bimodal distribution in rest-frame color at $z < 2$ (Strateva et al., 2001; Baldry et al., 2004a; Bell et al., 2004a; Williams et al., 2009), meaning galaxies can be broadly categorized as either actively star-forming spirals (the “blue cloud”), or quiescent ellipticals and lenticulars (the “red-sequence”). Although these populations are roughly equivalent in total stellar mass at $z \sim 1$, the quiescent galaxy population has nearly doubled in stellar mass, stellar mass density, and number density over the past ~ 7 Gyr (Arnouts et al., 2007; Bell et al., 2004a; Borch et al., 2006; Bundy et al., 2006; Brown et al., 2007; Faber et al., 2007). The favored explanation for this is that star-forming galaxies transform into passive ones through a process of “quenching” (Blanton, 2006; Bundy et al., 2006; Faber et al., 2007; Brammer et al., 2011).

Much work is now focused on understanding the specifics of quenching: where and when it happens in the course of a galaxy’s life, and how it is physically accomplished. Quenching is at least partly driven by environmental factors. A variety of studies at intermediate redshift show that galaxy properties correlate with local environment (Cooper et al., 2006, 2007; Quadri et al., 2007; Patel et al., 2009), such that groups and clusters contain more quiescent than active galaxies above a given stellar mass (George et al., 2011; Muzzin et al., 2012; Presotto et al., 2012; Tanaka et al., 2012; Nantais et al., 2017). Moreover, with increasing cluster-centric radius, observations find a relative reduction in the number of quiescent systems (e.g. Presotto et al., 2012). Processes such as galaxygalaxy mergers (Lavery & Henry, 1988), harassment and tidal interactions (Moore et al., 1998; Bekki & Couch, 2011), strangulation (Larson et al., 1980), and ram pressure stripping (Gunn & Gott, 1972) are all likely to take place in dense cluster environments, and are possible candidates for environmental quenching mechanisms.

Quenching also correlates with galaxy mass, in that more massive galaxies are more frequently quiescent (Kauffmann et al., 2004; Baldry et al., 2006; Peng et al., 2010).

Processes intrinsic to the galaxy, such as AGN feedback, or the exhaustion of gas reservoirs by star-formation-driven gas-dynamical outflows are possible candidates for mass-driven quenching mechanisms (McGee et al., 2014; Balogh et al., 2016).

Recent simulations have difficulty matching the clustering and abundance of red galaxies, frequently predicting too many quiescent galaxies (Coil et al., 2008; Weinmann et al., 2011; Vulcani et al., 2014). This is likely a problem with the given quenching prescription, which has been the subject of some scrutiny (McGee et al., 2009, 2011; Balogh et al., 2016). Whatever the mechanism, it must shut off star formation, possibly while effecting morphological transformation (Dressler, 1980). Observations in this area have the potential to constrain the relative contributions of the various nonlinear dynamical and baryonic processes that are thought to occur in dark matter halos.

1.1.2 The Color-Magnitude Relation

The quiescent population of galaxies exhibits a clear relationship between color and magnitude, such that brighter galaxies are redder (Bower et al., 1992; van Dokkum et al., 1998; Baldry et al., 2004a; Bell et al., 2004b). The color-magnitude relation (CMR) exhibits very little scatter, even over a range of eight in magnitude (Baldry et al., 2004a). This remarkable regularity within the quenched population provides many valuable clues to how quiescent galaxies formed and evolved over cosmic time (Bower et al., 1992; Peebles, 2002).

The CMR is commonly parametrized as a linear relationship between a galaxy's color and its magnitude, with a small, normal scatter in color. A galaxy's luminosity, being the integrated light of its stellar population, is a good proxy for its stellar mass, especially in near-infrared bands where dust attenuation is minimal. The interpretation of the color of a stellar population is more subtle, as it depends in general on a galaxy's dust content, age, star formation history, and metallicity.

The slope of the CMR is predominantly the result of a mass-metallicity relation, where more massive galaxies are more metal-enriched (e.g., Bower et al., 1992; Kodama & Arimoto, 1997; Vazdekis et al., 2001; Bernardi et al., 2003). The mass-metallicity relation has been studied from the local universe to $z \sim 3$ (Tremonti et al., 2004; Kewley & Ellison, 2008; Andrews & Martini, 2013; Erb et al., 2006; Maiolino et al., 2008; DeGroot, 2016). Such studies can inform our understanding of the history of galaxy star formation, feedback, outflows, and assembly (Finlator & Davé, 2008; Font et al., 2008a; Peeples & Shankar, 2011).

The zeropoint of the CMR describes the typical color of a quiescent galaxy at a fixed mass, which evolves with redshift in a manner consistent with the passive aging of a stellar population. The absolute value of the CMR zeropoint can therefore be interpreted to yield the age of the red-sequence population, or a formation redshift. The intrinsic color scatter of the CMR is commonly interpreted as intrinsic variation in the physical properties of red-sequence galaxies, independent of the dominant mass effect. From such considerations, it appears that roughly half of present-day quiescent galaxies were assembled relatively quickly well before $z = 1$, and evolved passively to the present day (e.g., Bower et al., 1998; Peebles, 2002; Blakeslee et al., 2003a; Mei et al., 2009; Foltz et al., 2015).

The CMR also provides a sensitive diagnostic for simulations that seek to reproduce the properties and distribution of the quiescent population. Early attempts at modeling the build-up of the red-sequence failed to reproduce the redshift evolution of the CMR slope

(Romeo et al., 2008; Menci et al., 2008). In general, reproducing the correct color-magnitude relation still requires some post-processing of the outputs of semi-analytical models (see e.g. Ascaso et al., 2015). Studying the red-sequence, especially at high redshift, is therefore a basic way to inform our understanding of many aspects of galaxy formation and evolution.

1.2 Overview of Studies

In this work, we present studies of galaxies in two samples of clusters, with the aim of better understanding the history of the quiescent population.

In Chapter 2, we study the galaxy color-magnitude relation in a sample of galaxy clusters at $z \sim 1$. We use the CMR zeropoint and scatter to constrain the formation redshift for the red-sequence galaxies. We also compare properties of the CMR as a function of cluster selection method, looking for any differences in the red-sequence as a function of the host halo.

In Chapter 3, we extend our analysis to a sample of four galaxy clusters at $1.3 < z < 1.65$, using a simple model of quenching to estimate the quenching timescale. Combining our results with other studies spanning $0 < z < 1.7$, we can compare the redshift evolution of the quenching timescale to that of several relevant timescales.

Chapter 2

The Red Sequence at $z \sim 1$

Galaxy clusters form from the gravitational collapse and clustering of fluctuations in the primordial density field (Press & Schechter, 1974; Gott & Rees, 1975b; Kravtsov & Borgani, 2012). This purely gravitational process is accompanied by the interrelated evolution of cluster baryonic components, including gas-dynamical radiative cooling and dissipation (White & Rees, 1978; Rudd et al., 2008; Gnedin et al., 2004; Kravtsov & Borgani, 2012), and the formation and accretion of stellar mass in the form of galaxies. The resulting mature galaxy clusters are massive dark matter halos with deep gravitational potential wells, containing a hot intracluster medium (ICM), old, evolved galaxies, and intergalactic stars.

Surveys detect clusters via their baryonic components: originally clusters were identified by visual overdensity of galaxies in the optical regime (Gunn et al., 1986; Abell et al., 1989; Lidman & Peterson, 1996; Ostrander et al., 1998; Gal et al., 2000), and later by detection of the X-ray luminosity generated by the ICM (Gioia & Luppino, 1994a; Scharf et al., 1997; Rosati et al., 1998; Romer et al., 2000). More recently, surveys have been designed to exploit the universal presence of a population of massive, quiescent galaxies (known as the red-sequence) in clusters (Gladders & Yee, 2000, 2005; Wilson et al., 2009; Muzzin et al., 2009; Rykoff et al., 2014), while others make use of overdensities of photometric redshifts (Stanford et al., 2005; Eisenhardt et al., 2008), or Sunyaev-Zeldovich (SZ) upscattering of cosmic microwave background photons by the ICM (Reichardt et al., 2013; Hasselfield et al., 2013; Planck Collaboration et al., 2014; Bleem et al., 2015).

Because these cluster detection methods select on baryons rather than halo mass, each is inherently biased toward either gas-rich systems (as with X-ray or SZ methods) or galaxy-rich systems (for red-sequence and photometric-redshift methods). Differences between gas-selected and galaxy-selected clusters are readily apparent, for example, when comparing the X-ray luminosity of the ICM, or cluster richness (Donahue et al., 2001; Rykoff et al., 2008; Hicks et al., 2013).

As a galaxy falls into a cluster, interactions with cluster baryons can rapidly shut off its star formation in a process known as "quenching". This environmental quenching is driven by either the cluster galaxies (e.g. harassment (Moore et al., 1996), tidal stripping (Merritt, 1983), and mergers (Toomre & Toomre, 1972; Rudnick et al., 2012)) or the hot gas component (e.g. ram pressure stripping (Gunn & Gott, 1972; Quilis et al., 2000)). One might expect that quenched galaxies in galaxy-rich red-sequence- or photometric-redshift-selected clusters would differ in their properties (e.g. luminosity-weighted ages and rest-frame colors) from quenched galaxies in gas-rich X-ray- or SZ-selected clusters, due to differences in quenching mechanisms and efficiencies.

Any such difference in the quiescent cluster galaxy populations will be more apparent at high redshift, when the galaxies are younger. While X-ray cluster surveys have detected clusters out to $z \sim 1$, the launch of the Infrared Array Camera (IRAC, Fazio et al., 2004) on board the *Spitzer Space Telescope* (Werner et al., 2004) has allowed systematic infrared red-sequence surveys to detect clusters at $z > 1$. *Spitzer*/IRAC wide-area surveys have proven effective at identifying more clusters down to low masses at $1 < z < 2$ (e.g., Papovich et al., 2010; Stanford et al., 2012; Zeimann et al., 2012; Muzzin et al., 2013b; Wylezalek et al., 2013; Rettura et al., 2014), where current X-ray and SZ observations are restricted to only the most massive systems. We now have the opportunity to study quenched galaxies in red-sequence- and X-ray-selected clusters at $z = 1$, spanning the extremes of cluster baryon partitioning.

The focus of our study is the Gemini Cluster Astrophysics Spectroscopic Survey (GCLASS [1], PIs: Wilson & Yee Muzzin et al., 2012). GCLASS is a sample of 10 red-sequence-selected clusters at $0.87 < z < 1.34$, initially detected by the SpARCS optical/IR cluster survey using the cluster red-sequence detection method developed by Gladders & Yee (2000) (see Muzzin et al., 2009; Wilson et al., 2009; Demarco et al., 2010). Our comparison sample is drawn from the ACS Intermediate Redshift Cluster Survey (ACS IRCS) (Ford et al., 2004), a sample of six X-ray-selected and two optically-selected clusters at $0.8 < z < 1.3$, spanning a comparable range of redshifts and cluster masses. Five of the clusters were identified from the ROSAT Deep Cluster Survey (Rosati et al., 1998), while MS 1054-03 comes from the Einstein Extended Medium Sensitivity Survey (Gioia & Luppino, 1994b) and the clusters CL 1604+4304 and CL 1604+4321 were found in a Palomar deep near-infrared photographic survey (Gunn et al., 1986). Extensive spectroscopic follow-up campaigns were

---

[1] http://www.faculty.ucr.edu/~gillianw/GCLASS/

conducted to assign cluster membership in these systems (e.g., Demarco et al., 2005, 2007; Holden et al., 2006; Gal et al., 2008; Rettura et al., 2010).

The red-sequence of galaxies is defined by a relation between the color and magnitude of quiescent galaxies (Bower et al., 1992; van Dokkum et al., 1998; Baldry et al., 2004b; Bell et al., 2004b), and the slope and intrinsic scatter of this relation has been used to constrain the formation epochs and age spread of the early-type populations within galaxy clusters (Bower et al., 1998; Blakeslee et al., 2003a; Mei et al., 2009). We will extend this study to our sample of red-sequence-selected clusters, comparing the formation redshifts and age spread constraints derived from our sample against those found for the comparison sample and others. If the red-sequence method preferentially selects older, more evolved systems, we would expect the red-sequence in these clusters to appear redder and exhibit less intrinsic scatter than other clusters at similar redshift.

The structure of this chapter is as follows: Our data set is described in Section 2.1. In Section 2.2, we describe our cataloging and our methods for deriving galaxy rest-frame colors and stellar masses, as well as our fitting of the color-magnitude and color-mass relations. We compare spectroscopic and rest-frame UVJ selection methods in section 2.2.5. The results of our study are discussed in Section 2.3, while in Section 2.4 we summarize our conclusions.

In this work we will assume a standard ΛCDM cosmology with $H_0 = 70\mathrm{km} \cdot \mathrm{s}^{-1} \cdot \mathrm{Mpc}^{-1}$, $\Omega_M = 0.3$, and $\Omega_\Lambda = 0.7$, and a Chabrier IMF (Chabrier, 2003) throughout. Our magnitudes are reported in the AB system, unless reported otherwise.

2.1 Data

The red-sequence-selected clusters studied in this work are taken from GCLASS. GCLASS is a spectroscopic survey of 10 rich clusters at $0.85 < z < 1.34$ which were initially detected by the SpARCS optical/IR cluster survey using the cluster red-sequence detection method developed by Gladders & Yee (2000) (see Muzzin et al., 2009; Wilson et al., 2009; Demarco et al., 2010).

This cluster sample was the focus of a large spectroscopic campaign performed with the Gemini North and South Observatories. A total of 46 masks were observed over the ten clusters with the goal of identifying ~ 50 members in each cluster. Galaxies were selected for spectroscopic follow-up through a combination of three criteria: distance from the cluster center, observed z' - 3.6μm color, and 3.6μm flux. Together these criteria ensure that the spectroscopic completeness is largely a function of stellar mass and radius, with the highest completeness found for massive galaxies in the cluster core (Muzzin et al., 2012).

The spectroscopic confirmation of these clusters was followed by optical imaging in u' g' r' i' bands. For the six northern clusters, these data were taken with MegaCam at the Canada-France-Hawaii Telescope (CFHT), while for the southern clusters these data come from IMACS at Magellan/Baade (u' g' r' i') . WIRCam at CFHT provided near-infrared J- and Ks-band data for the northern clusters, while for the southern clusters these data came from HAWK-I at the Very Large Telescope (VLT) or ISPI at CTIO/Blanco (van der Burg et al., 2013a). Our photometry also includes the 3.6, 4.5, 5.8, and 8.0 μm IRAC data from the Spitzer Wide-area Extragalactic Survey (SWIRE, Lonsdale et al. (2003)) and z' band data from the SpARCS survey taken by the MOSAIC-II camera at the Cerro Tololo

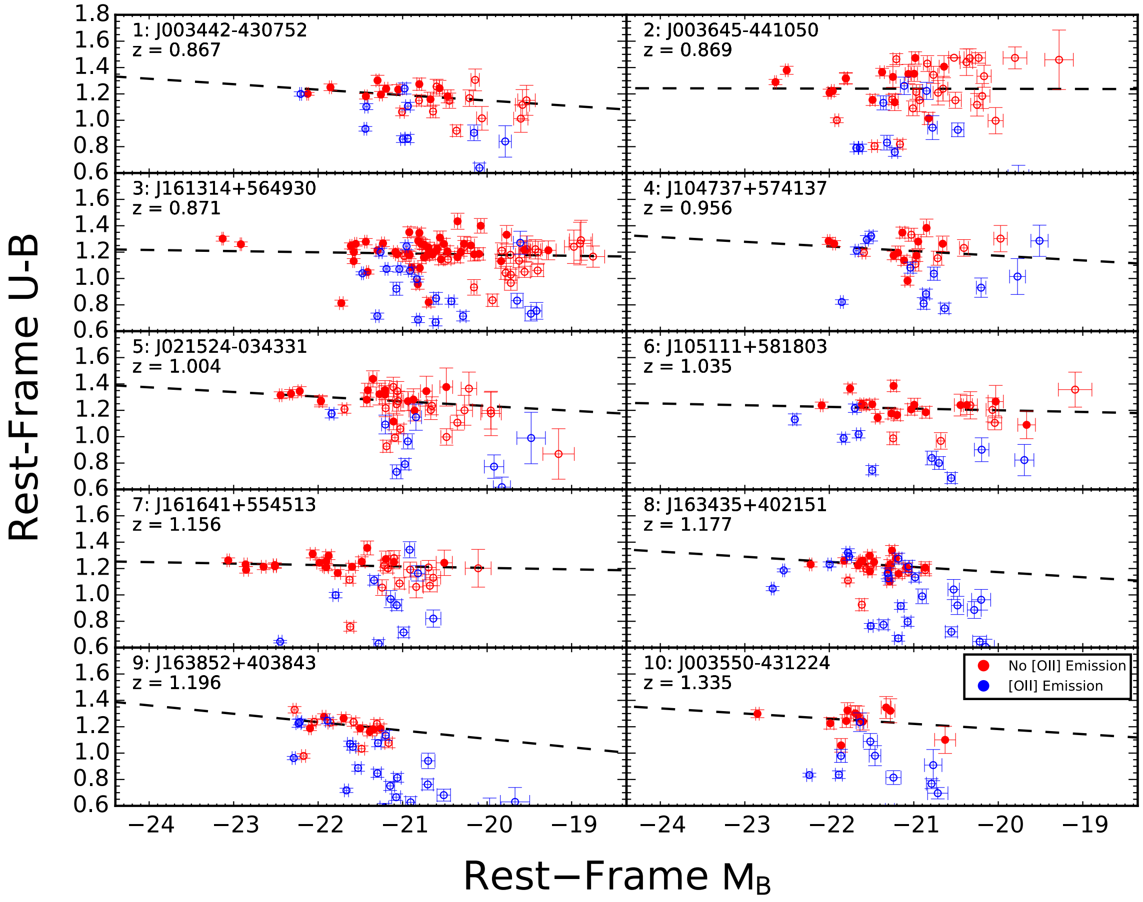

Figure 2.1 Rest-frame U-B color versus absolute rest-frame B magnitude for spectroscopic members of each of the ten clusters in the GCLASS sample. Quiescent members are shown in red. Those within R_{200} above the 80% mass completeness limit (see Table A.1) are shown as solid. [OII]-emitters are shown in blue. The dashed lines show the Bayesian maximum likelihood linear fits to the color-magnitude relation for quiescent galaxies within R_{200} above the 80% mass completeness limit (solid red circles). See also Section 2.2.4 and Table A.2. Note that some galaxies are classified as active because they have [OII] emission lines despite having colors consistent with red-sequence quiescent members. These could be be AGN, dust-obscured star-forming galaxies, or red-sequence objects with some residual star formation. They are not included in the fit.

Inter-American Observatory (CTIO) (see Muzzin et al., 2009; Wilson et al., 2009, for details on the Northern and Southern z' observations, respectively).

A summary of the GCLASS sample is presented in Table A.1. For more details on the spectroscopic and photometric observations we refer the reader to Muzzin et al. (2012) and van der Burg et al. (2013a), respectively. The GCLASS sample has been used to study brightest cluster galaxies (Lidman et al., 2012a, 2013, Rettura et al., in prep.), the relative effect of environment quenching and stellar mass quenching on galaxy evolution (Muzzin et al., 2012), cluster and field stellar mass functions at $z \sim 1$ (van der Burg et al., 2013a), cluster scaling relationships (van der Burg et al., 2014), and phase space analysis constraints on the locations and timescales of quenching (Noble et al., 2013; Muzzin et al., 2014a).

2.2 Analysis

2.2.1 Photometric Catalog

As described in detail in van der Burg et al. (2013a), the imaging data were combined into a matched catalog by first using Source Extractor to detect sources in the K_s-band data. Each object was assigned a Gaussian PSF weight function based upon the Source Extractor half-light radius in the Ks-band image. This function was used to compute the weighted Gaussian-aperture-and-PSF flux for each object (Kuijken, 2008). Robust errors were calculated by directly measuring the 1-σ variation in background flux in randomly-placed apertures that do not contain any sources.

Galaxies are considered to be cluster members if they have a velocity relative to the cluster of $\Delta v \leq 1500 \text{ km} \cdot \text{s}^{-1}$. For each cluster, this velocity dispersion was measured using the bi-weight estimator (Beers et al., 1990) from the line-of-sight velocity distributions, after rejecting outliers (Girardi et al., 1993; Fadda et al., 1996). R_{200}, the radius for which the mean density is 200 times the critical density at the cluster redshift, was calculated assuming spherical clusters and the Evrard et al. (2008) relation between M_{200} and the velocity dispersion (see Wilson et al., 2015, in prep. for details). Altogether this yields a total of 432 spectroscopically-confirmed cluster members for the full sample of ten clusters.

The photometric data were then matched to the spectroscopic catalog, such that each spectroscopic member considered in this work also has associated photometry in *u' g' r' i' z' J Ks* and 3.6, 4.5, 5.8, 8.0 μm. In the following sections, we employ this catalog to derive rest-frame colors and magnitudes, stellar masses, and to fit the color-magnitude and color-mass relations for our cluster sample.

2.2.2 Rest-Frame Colors

In order to compare the photometric properties of cluster members over the range $0.8 < z < 1.3$, we need to first derive absolute rest-frame colors and magnitudes for these galaxies, to eliminate the effects of distance and account for k-correction.

To derive rest-frame photometry, we use the publicly-available photometric redshift code EAZY (Brammer et al., 2008), to fit the broadband photometry of each cluster member to a linear combination of seven basis templates derived from the prescription in Blanton & Roweis (2007). These templates have been optimized for deep optical-NIR broad-band surveys, and this code was optimized specifically for K-selected samples such as our own. Comparing against the SEDs of galaxies in the GOODS-CDFS field, Brammer et al. (2008) have shown that this method provides rest-frame optical photometry that is accurate to within 5%.

We infer rest-frame absolute Johnson U and B magnitudes ($M_{U,z=0}$, $M_{B,z=0}$) for each cluster member in our sample by convolving this best-fit linear combination of SEDs with filter curves redshifted to the spectroscopic redshift of each galaxy. These filters are chosen in order to directly compare results with those from the X-ray selected ACS IRCS sample (Mei et al., 2009, hereafter M09). We define the rest frame color $(\mathrm{U}-\mathrm{B})_{z=0}$ as the difference between these rest-frame magnitudes. We note that the span of our 11 observed filters ensures that rest-frame magnitudes are interpolated from the available data, often overlapping with multiple observed passbands.

The rest frame $M_{B,z=0}$ magnitudes and $(\mathrm{U}-\mathrm{B})_{z=0}$ colors of cluster members are plotted in Figure 2.1. Quiescent members are shown in red. Those within R_{200} above the 80% mass completeness limit (see Table A.1) are shown as solid. [OII]-emitters are shown in blue. Some objects, while having colors consistent with red-sequence quiescent members, are nevertheless classified as active due to the presence of [OII] emission lines; these might be AGN, dust-obscured star-forming galaxies, or red-sequence objects with some residual star formation. They are not included in the CMR fit.

The estimated 1-σ uncertainties in these rest-frame colors and magnitudes are derived from 200 Monte Carlo simulations: the observed flux in each passband is varied by a random amount drawn from a normal distribution with a standard deviation given by the photometric uncertainties, and the CMR fit repeated. The central 68% of the resulting output then defines the upper and lower confidence intervals on our rest-frame $(U-B)_{z=0}$ color.

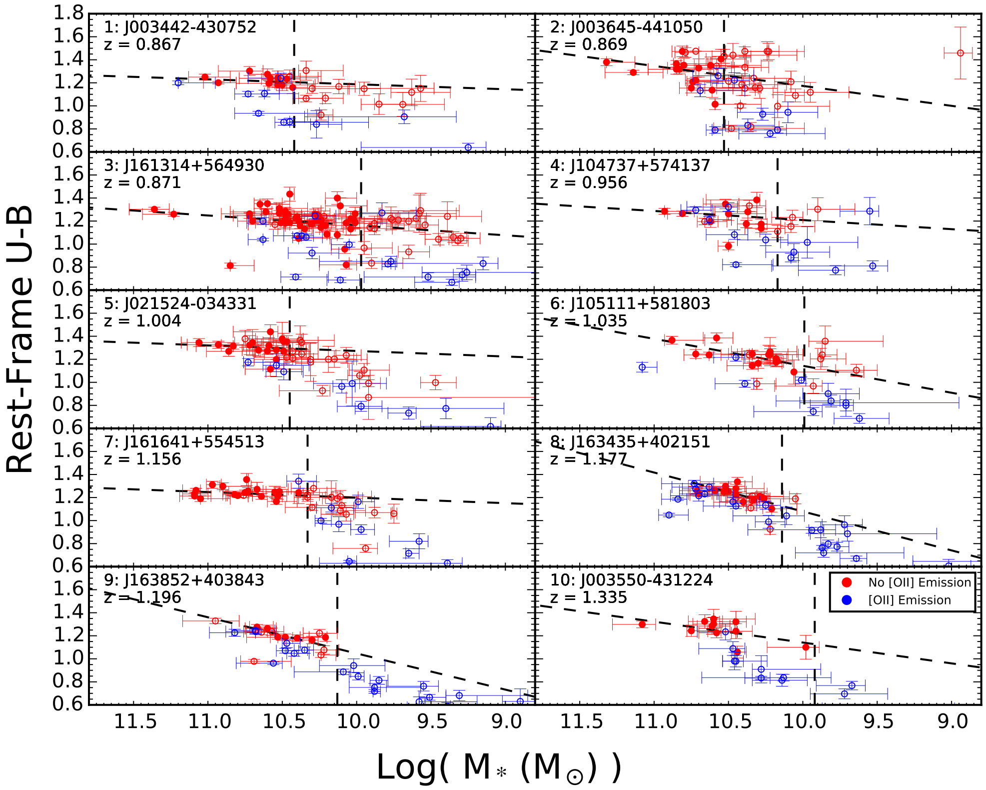

Figure 2.2 Color-mass relation for each cluster in the GCLASS sample. Symbols are as in Figure 1. The dashed lines show the Bayesian maximum likelihood linear fits to the color-mass relation for quiescent galaxies within R_{200} above the 80% mass completeness limit (solid red circles). See also Section 2.2.4 and Table A.3. Note that some galaxies are classified as active because they have [OII] emission lines despite having colors consistent with red-sequence quiescent members. These could be be AGN, dust-obscured star-forming galaxies, or red-sequence objects with some residual star formation. They are not included in the fit.

2.2.3 Stellar masses

Here we use our photometric catalogs to derive stellar masses for the cluster members for the purpose of fitting the color-mass relations.

Using the publicly-available SED fitting code FAST (Kriek et al., 2009), we fit the 11-passband photometry to Bruzual & Charlot (2003a) (BC03) stellar populations synthesis templates. Although other stellar models employ a different treatment for contributions from thermally pulsing asymptotic giant branch (TP-AGB) phase stars, there is disagreement about the significance of TP-AGB stars for galactic SEDs and inferred galactic properties (Kriek et al., 2010). The population models with a different treatment of the TP-AGB phase, such as those from Maraston (2005), yield stellar masses that are lower by 0.1 dex on average. These values are consistent within error bars with those derived from BC03, and the choice of model does not significantly impact our results at the redshift range considered in this study (see e.g. Rettura et al., 2006).

FAST proceeds by generating a grid of synthetic SEDs for stellar populations at the spectroscopic redshift of each galaxy from the given population synthesis templates, for a range of star formation histories (SFH), ages, and masses, with possible additional variation in dust attenuation and/or metallicity. Best-fit stellar populations are then selected from this grid by minimizing χ^2 when comparing the SED to the observed broad-band photometry of a given galaxy, providing us with an estimate of stellar mass.

For our grid of parameters, we use a range of ages from 10 Myr to 10 Gyr (excluding ages greater than the age of the universe at the observed redshift) and an A_V ranging from 0 to 4 mag with a Calzetti extinction law (Calzetti, 2001). An exponentially declining star formation rate is assumed with a time constant, τ, ranging from 10 Myr to 10 Gyr. A Chabrier IMF (Chabrier, 2003) and fixed (solar) metallicity of 0.02 is assumed throughout.

With the best fit stellar mass thus derived, a confidence interval is provided by a Monte Carlo simulation with 200 iterations. The color-mass relations are plotted in Figure 2.2.

2.2.4 Color-Magnitude and Color-Mass Relations

Having explained how we derive rest-frame colors and magnitudes in Section 2.2.2, and stellar masses in Section 2.2.3, we are now ready to determine the color-magnitude and color-mass relations.

From the spectroscopically-confirmed cluster members in each cluster, we select red-sequence galaxies for the purpose of fitting the CMR. A member galaxy is included in the fit if it meets the following three criteria:

1. Quiescent galaxies are selected as those galaxies without any detected [OII] emission line, where the detection limit is ~ -1Å to -3Å equivalent width, depending on signal-to-noise (see Muzzin et al., 2012).

2. We select galaxies above the 80% mass completeness limit for each cluster (calculated in van der Burg et al., 2013a).

3. For each cluster, we fit to quiescent galaxies within R_{200}. The GCLASS clusters, despite their richness, display a variety of morphologies and so the centroid of the cluster was taken to be the brightest cluster galaxy (Lidman et al., 2012a). The R_{200} radii for the GCLASS sample were taken from Wilson et al. (2015, in prep).

For each cluster, quiescent galaxies selected as described above (solid red circles in Figure 2.1) were fit by a rest-frame $(U-B)_{z=0}$ versus $M_{B,z=0}$ color-magnitude relation of the following form:

$$(U-B)_{z=0} = \text{slope} \times (M_{B,z=0} + 21.4) + c_0 \tag{2.1}$$

where $M_{B,z=0}$ is the rest-frame B magnitude, and c_0 is the CMR zeropoint. A magnitude offset of 21.4 is applied to reduce the covariance of the slope and zeropoint. The specific value of 21.4 is taken from M09, to allow for direct comparison.

It has been noted for some time that the choice of linear regression method can bias the estimate of slopes and correlation coefficients (Kelly, 2007). Where possible, we prefer to use a Bayesian maximum likelihood estimator (MLE) to yield the least biased values, and do so to arrive at the fits shown in Figures 2.1 and 2.2 and the analysis performed in Sections 2.3.2 and 2.3.3. However, in order to directly compare with M09, Bower et al. (1992), van Dokkum et al. (1998), and Ellis et al. (1997) (Section 2.3.1), we will use a total least squares (TLS) method to most closely match the comparison analysis.

Our TLS method derives uncertainties in the fit parameters using a bootstrapping method with 1000 simulations to calculate the 68% confidence interval in slopes, scatters, and zeropoints. The intrinsic scatter of the relation is calculated by subtracting in quadrature the photometric error from the biweight scale estimate of the color residuals.

For the MLE method, we calculate the posterior probability distributions of the slope, zeropoint, and intrinsic scatter with a Markov chain Monte Carlo method. These probability distributions directly yield the most likely value of each fit parameter and the associated 68% confidence interval. The MLE method has been shown to yield more unbiased fits and confidence intervals than other linear regression methods (Kelly, 2007).

The regression parameters reported by each method are compatible within error bars, although the uncertainty of the MLE-derived CMR parameters increases by as much as $\sim 35 - 45\%$, as expected. The TLS method finds a slope that is $\sim 20\%$ steeper on average, and smaller intrinsic scatters throughout, while there is agreement to within $\sim 2\%$ for the average zeropoints. The slopes, scatters, and zeropoints of the CMRs derived for each of the GCLASS clusters using both methods are reported in Table A.2.

The properties of the CMR depend in part on the morphology of the galaxies that are included in the red-sequence. A red-sequence including both lenticular and elliptical galaxies (E+S0) typically exhibits $\sim 30\%$ more scatter than a purely elliptical sample (see e.g. Bower et al., 1992, M09). In all cases, our results will be compared to literature values derived for E+S0 galaxies, and we discuss this comparison in Section 2.3.1.

In addition to making a fit to the color-magnitude relation for each cluster (Figure 2.1), we also make a fit to the color-mass relation (Figure 2.2). We employ a fit of the form:

$$(U - B)_{z=0} = \text{slope} \times (\text{Log}(M_*/M_\odot) - 10.6) + c_0 \tag{2.2}$$

where we have chosen the mass offset of 10.6 dex so that the average color-mass zeropoint corresponds to the average color-magnitude zeropoint, described in greater detail in Section 2.3.4.

We employ a Bayesian maximum likelihood estimator to obtain the fit parameters. As we do not compare our color-mass fits to literature values, this single fitting method will

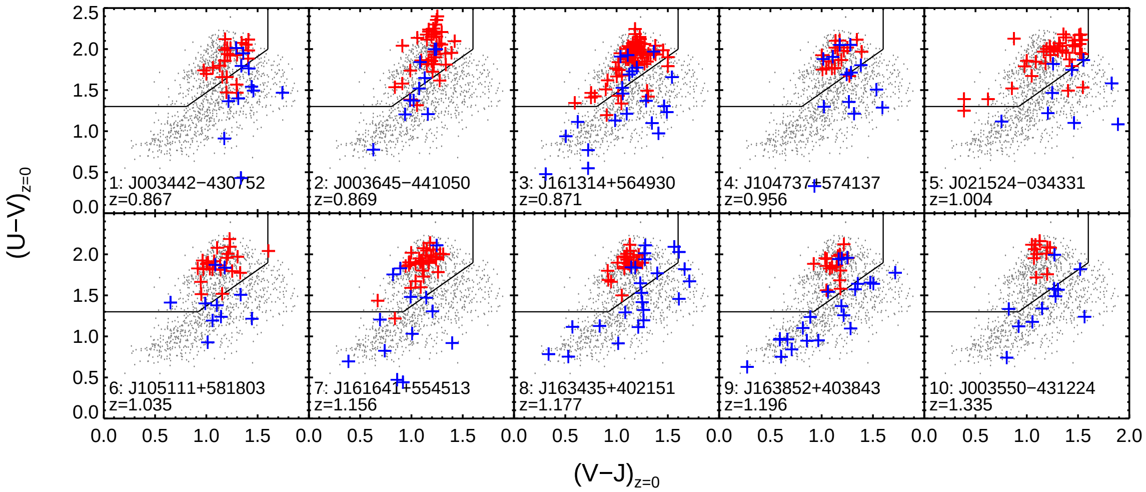

Figure 2.3 Rest-frame U-V versus V-J color for each cluster in the GCLASS sample. Quiescent cluster members (without [OII] emission lines) are plotted as red crosses, while star-forming cluster members are plotted in blue. The solid lines show the color-color cut used by Williams et al. (2009) for distinguishing quiescent from star-forming galaxies, where the upper-left quadrant is typically populated by quiescent galaxies. We plot in gray a sample of field galaxies from GCLASS with masses $M_* > 10^{9.5}\ M_\odot$ that are between $0.85 < z < 1.35$, to illustrate the color space occupation at the redshift of the clusters. 14% of the UVJ-quiescent population show [OII] emission, while 16% of the UVJ-star-forming galaxies exhibit no [OII] emission.

be sufficient for our purposes and yield the least biased results.

We show the color-mass relations in Figure 2.2. The fit parameters are reported in Table A.3, and discussed in Section 2.3.4.

2.2.5 Rest-frame UVJ Diagrams

Rest-frame UVJ color-color selection is often used to distinguish quiescent and star-forming galaxies in field galaxy surveys at redshifts $0 < z < 4$ when spectroscopic or morphological information is not available (Wuyts et al., 2007; Williams et al., 2009; Whitaker et al., 2011; Patel et al., 2012; van der Burg et al., 2013a; Whitaker et al.,

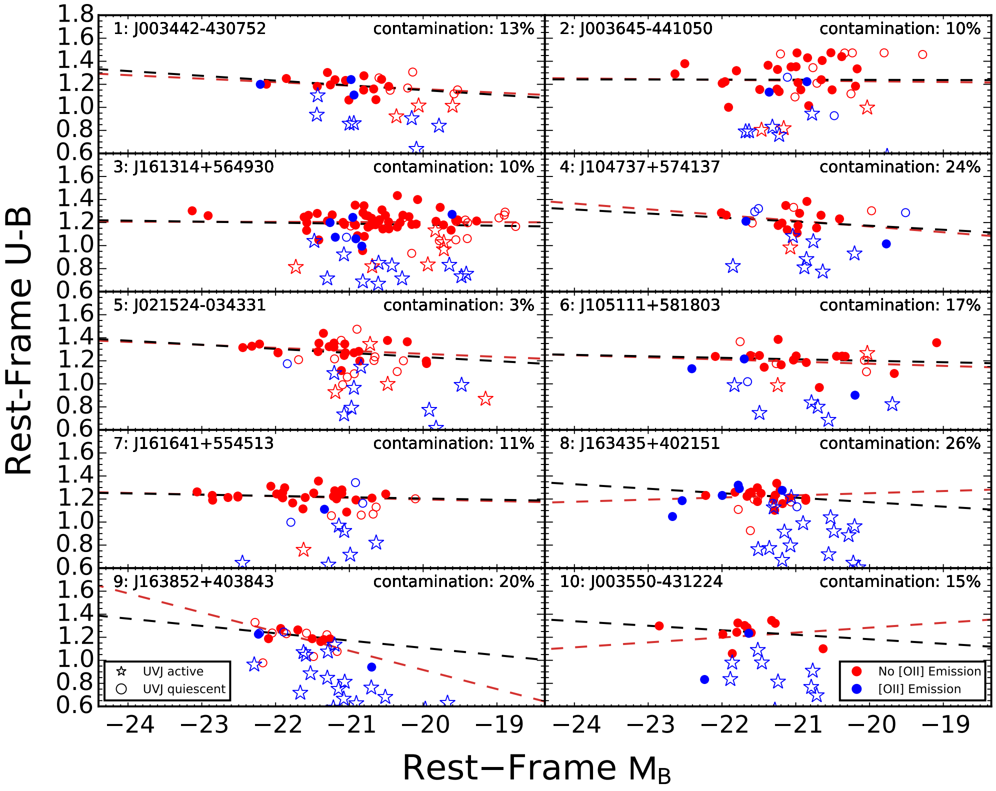

Figure 2.4 Figure showing how red sequence slope would differ if quiescent members are selected on UVJ color rather than spectroscopically (compare red line to black line from Figure 2.1). As in Figure 2.1, the figure shows rest-frame U-B versus rest-frame absolute B magnitude for spectroscopic members, color coded by spectroscopically quiescent (red) and star forming (blue), but with symbols denoting UVJ quiescent (circles) and active (stars). The indicated contamination measures the proportion of UVJ-quiescent, spectroscopically-active galaxies (blue circles). The fit shown as a dashed red line is to the solid circles which are UVJ-quiescent galaxies within R_{200} above the 80% mass completeness limit. See discussion in Section 2.2.5.

2013; Muzzin et al., 2013b; Strazzullo et al., 2013). Because the GCLASS dataset consists of a large number of both quiescent and active spectroscopically-confirmed members, the GCLASS dataset allows a unique insight into the efficacy of the UVJ selection technique, by allowing us to compare the degree of agreement between UVJ- and spectrally-classified active / quiescent members.

We plot all of the spectroscopically-confirmed cluster members in rest-frame UVJ color-color space in Figure 2.3. As in Figures 2.1 and 2.2, members are colored according to spectroscopic classification, with red being quiescent and blue showing [Oii] emission lines (see Section 2.2.4).

Those galaxies falling in the upper-left quadrant of this plot are classified as UVJ-quiescent according to the cuts described in Williams et al. (2009). There is a clear, but not exact, agreement between the spectroscopic and UVJ methods: 14% of the UVJ-quiescent population show [Oii] emission, while 16% of the UVJ-star-forming galaxies exhibit no [Oii] emission. Although we do not expect much contamination from AGN, an [Oii] selection nevertheless excludes these objects. The main source of contamination for an [Oii] selection is likely dusty star-forming galaxies. While the UVJ selection accounts for dust, uncertainty in rest-frame colors will naturally result in some cross-contamination between the quiescent and star-forming populations, especially for galaxies close to the dividing lines. For our sample, a spectroscopic [Oii]-based selection is more stringent than one based on UVJ colors, ultimately identifying fewer quiescent galaxies.

This level of contamination is similar to that found by other studies (Kriek et al., 2014). In a large sample of galaxies spanning a redshift range $0.8 \leq z \leq 1.2$, Cardamone et al. (2010) finds that 20% of galaxies on the red-sequence fall outside the UVJ-quiescent selection region. Moresco et al. (2013) study the relative agreement of different quiescent selection methods, finding [OII] emission lines for 38% of the UVJ-quiescent galaxies, and an overall $20 - 40\%$ contamination for this method. Additionally, from a total sample of of 19 cluster galaxies at $z = 1.80$, Newman et al. (2014) find 12% of members classified as UVJ-star-forming when they are spectroscopically quiescent.

To better understand the implications of UVJ versus spectroscopic selection methods, we repeat the CMR relationship fitting of Section 2.2.4, now using the UVJ classification instead of the [OII] spectral feature to select quiescent galaxies. The resulting fits are shown in Figure 2.4.

In this figure, as in Figures 2.1, 2.2, and 2.3, members with an [OII]-emission line are shown in blue while spectroscopically-quiescent members are shown in red. At the same time, we represent UVJ-quiescent members as circles and UVJ-active members as stars. Therefore, UVJ-selected quiescent galaxies that were previously excluded by the [OII]-selection of Section 2.2.4 are shown as blue circles. The relative number of these objects is labeled as the quiescent contamination for each cluster. Lastly, the UVJ-quiescent galaxies that satisfy the remaining two criteria of Section 2.2.4, being within R_{200} and above the 80% mass completeness limit, are solid symbols. The MLE CMR fit to these solid circles is shown as a dashed red line, contrasted by the black line which shows the fits derived previously in Section 2.2.4 for the [OII]-selected quiescent galaxies.

The intrinsic scatter is comparable for both selections, although the zeropoint and slope of the UVJ-selected red-sequences are more discrepant over our range of clusters, exhibiting larger uncertainties and a wider spread in values. For most clusters, the small number of contaminants introduced by UVJ selection has little impact on the CMR slope. The largest discrepancies are seen in our highest-redshift clusters which have fewer spectroscopic members overall, where the inclusion or removal of one or two galaxies can dramatically impact the resulting CMR fit (Figure 2.4).

We conclude that while the rest-frame UVJ selection technique is generally effective in separating quiescent from star-forming galaxies in the absence of spectroscopy, we caution that users should expect a non-negligible amount of contamination ($\sim 15\%$ in this case).

2.3 Discussion

2.3.1 Comparison of Color-Magnitude Relation as Function of Cluster Selection Method

Figure 2.5 shows the red-sequence slope, intrinsic scatter, and zeropoint for the ten GCLASS clusters plotted versus the cluster redshift. Also shown are the data from the ACS IRCS sample (Ford et al., 2004, M09), including six X-ray selected and two optically-selected clusters spanning a redshift range $0.83 < z < 1.3$. We also plot data from the local clusters Coma, Virgo, and CL0016 (z = 0.546) (Bower et al., 1992; van Dokkum et al., 1998; Ellis et al., 1997). For comparison, we plot the biweight mean and 1-σ variation of the ACS IRCS sample parameters. Within uncertainties, the data points for all GCLASS clusters fall within the 1-σ variation of the biweight mean values of the ACS IRCS sample.

We find no significant difference between the red-sequences found in X-ray- and

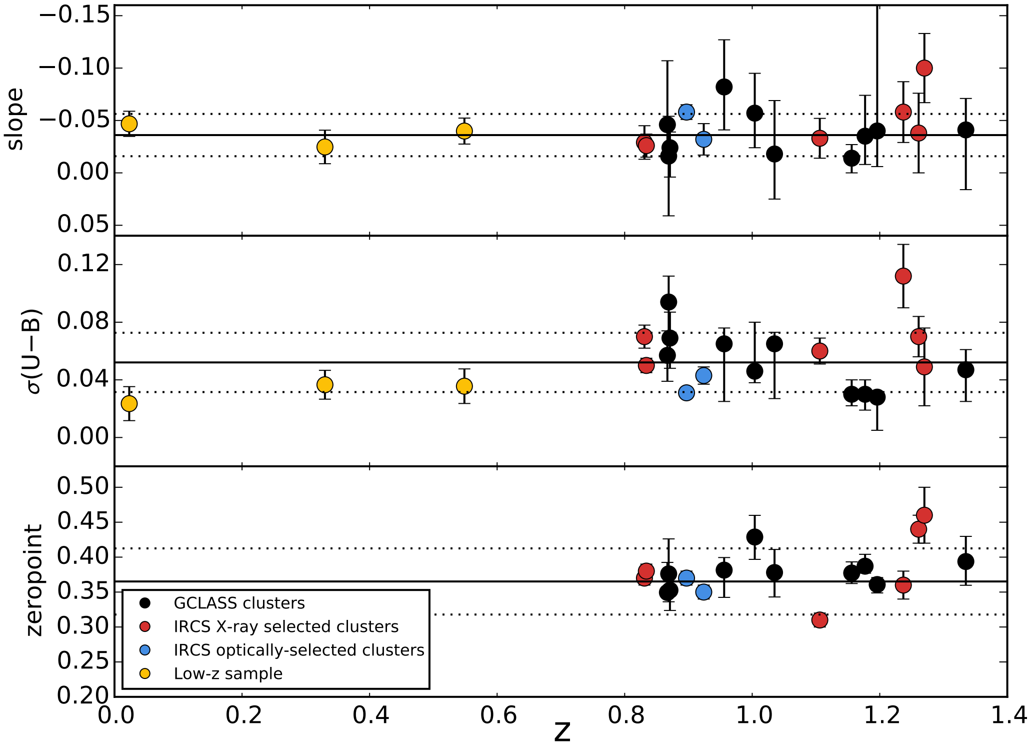

Figure 2.5 Evolution of the color-magnitude relation slope (top), scatter (middle), and zeropoint (bottom) with redshift, compared to values drawn from the literature. Data points from the GCLASS clusters are plotted as black circles, data from the ACS Intermediate Redshift Survey as red circles (X-ray-selected) or blue circles (optically-selected) (M09), and data from a local sample (Bower et al., 1992; van Dokkum et al., 1998; Ellis et al., 1997) as yellow circles. The biweight mean value of the parameters from the ACS IRCS sample of X-ray-detected clusters is plotted as a solid line, with dotted lines indicating the 1-σ range. We find no measurable difference in the slope, zeropoint or scatter of the CMR in clusters selected by the X-ray or red-sequence technique (see Section 2.3.1) The zeropoints shown here are Vega magnitudes.

red-sequence-selected galaxy clusters. A Student's t-test reveals agreement between the fit parameters we report versus those drawn from the ACS IRCS sample ($t = 0.89, p = 38\%$). We conclude that the stellar populations of quiescent galaxies in these clusters selected by different methods have comparable histories of stellar formation and evolution. We can detect no indication that these quiescent populations have experienced different quenching histories or processes, and it is likely that the dominant quenching process does not depend on the baryon partitioning of the cluster. If differences in the quenching mechanism or history are present, they are not detectable in the resultant red-sequence properties at $z \sim 1$, at least at the resolution of our observations.

Overall, the X-ray and red-sequence methods are selecting clusters with relatively similar CMRs and small intrinsic scatters, which indicates a high formation redshift for the bulk of the massive galaxy populations in these clusters. Perhaps surprisingly, the agreement in CMR zeropoint between these samples indicates that the red-sequence method is not selecting clusters with older, more evolved populations. While the methods may still select different clusters by mass, evolutionary state, or virialization, those properties do not seem to correlate with the stellar populations of the galaxies.

In addition, we find that the CMR slope and scatter have not significantly evolved since redshift $z \sim 1.3$. This is in agreement with prior studies of clusters for z < 1.5 (e.g. M09, Snyder et al., 2012). For these parameters, a Bayesian model comparison substantially favors a constant over a model that is linear with redshift. Over the redshift range we sample, we find no measurable evolution in the zeropoint ($0.8 < z < 1.3$).

2.3.2 Red-Sequence Ages

The $(U - B)_{z=0}$ color of the galaxies we have been studying is the result of several competing influences: principally, it will be determined by the galaxy metallicity in a mass-dependent fashion; it will also redden as young, blue stars die out or transition onto the red giant branch, or become bluer as ongoing star formation provides new, massive stars. The redshift evolution of the CMR (in slope, zeropoint, and scatter) is therefore sensitive to all of these factors, and we can partially constrain the formation and evolution of early-type galaxies by comparing our results to models.

Our models have two parameters: their formation redshift and star formation history (SFH). For the choice of SFH, we generate models with both single-burst simple stellar populations (SSP) and exponentially-declining star formation histories (eSFH). The formation redshifts range from $2 \leq z_f \leq 9$. For details on the construction of these models, see Appendix A.

The zeropoint of the CMR models is simply the $(U - B)_{z=0}$ color evaluated at $M_B = -21.4$. The zeropoint is a measure of the average color of the red-sequence and therefore is sensitive to both the age of the galaxies and the extent of their most recent star formation. For this reason it can constrain the star formation weighted age, $\langle t \rangle_{\text{SFH}}$, which gives the average age of the bulk of the stars. From this age we can also establish a star formation weighted formation redshift, $\langle z_f \rangle_{\text{SFH}}$. See Appendix A for the definition of these quantities.

Altogether, within the error bars of our measurement, we find no significant evolution of the zeropoint with redshift for our clusters. As $(U-B)_{z=0}$ color evolves most rapidly for young stellar populations, this implies that the bulk of the stars must have formed at sufficiently high redshift so that their color is only slowly evolving by $z \sim 1$. We note that this is a constraint on the overall age of the stars, while the galaxies were likely assembled some time after the initial star formation.

Although the eSFH models redden more slowly, both SSP and eSFH models agree on a lower-bound for $\langle z_f \rangle_{\mathrm{SFH}} \sim 3$ for our highest redshift clusters. Essentially, this means that if the red-sequence galaxies were still forming stars below $z \sim 3$, the high-redshift CMRs would appear bluer than what we observe in GCLASS.

If we assume that the principle cause of the intrinsic scatter about the CMR is due to a spread in galaxy ages, it is then possible to constrain this spread by comparing our observed intrinsic scatter with red-sequence models. To do this, we first quantify the difference in $(U-B)_{z=0}$ color between two galaxies, $\Delta(U-B)_{z=0}$, as a function of time and of the difference in the galaxies' ages, Δt, and relate this to the observed scatter.

Since $(U-B)_{z=0}$ color evolves most quickly for young stellar populations, the largest $\Delta(U-B)_{z=0}$ color differences are apparent when both galaxies are young. However, a larger difference in galaxy ages also yields a higher $\Delta(U-B)_{z=0}$ overall, leading to a degeneracy in the color difference / age difference relation which can be partially broken by using our previous zeropoint constraint to require that our galaxies be at least as old as $\langle t \rangle_{\mathrm{SFH}}$. At $z \sim 1$, our lower bound of $\langle z_f \rangle_{\mathrm{SFH}} \sim 3$ corresponds to a minimum galaxy age of 3.6 Gyr. The age of the universe at $z \sim 1$ provides an upper bound on galaxy age differences to be below $\Delta t < 2$ Gyr at the most extreme.

The time evolution of $\Delta(U-B)_{z=0}$ color differences for pairs of galaxies of different

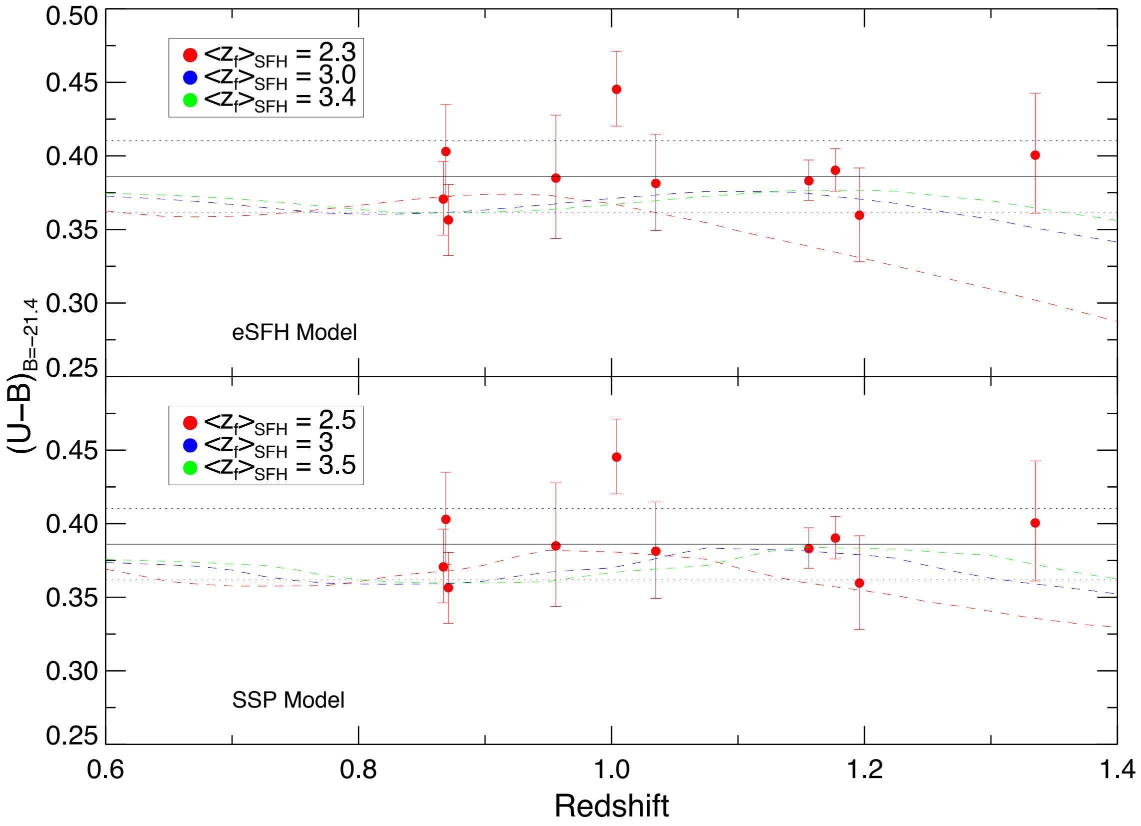

Figure 2.6 Evolution of the color-magnitude relation zeropoint with redshift, compared with exponential SFH (top) and SSP (bottom) model red-sequences. Measured zeropoints of the GCLASS clusters are plotted as red circles in the same manner as the bottom panel of figure 2.5. Model values are plotted as dashed lines, while the biweight mean and 1-σ variation of our zeropoint values are plotted as solid and dotted lines, respectively. The minimal value for $\langle z_f \rangle_{\rm SFH}$ that agrees with the data is ~ 3.

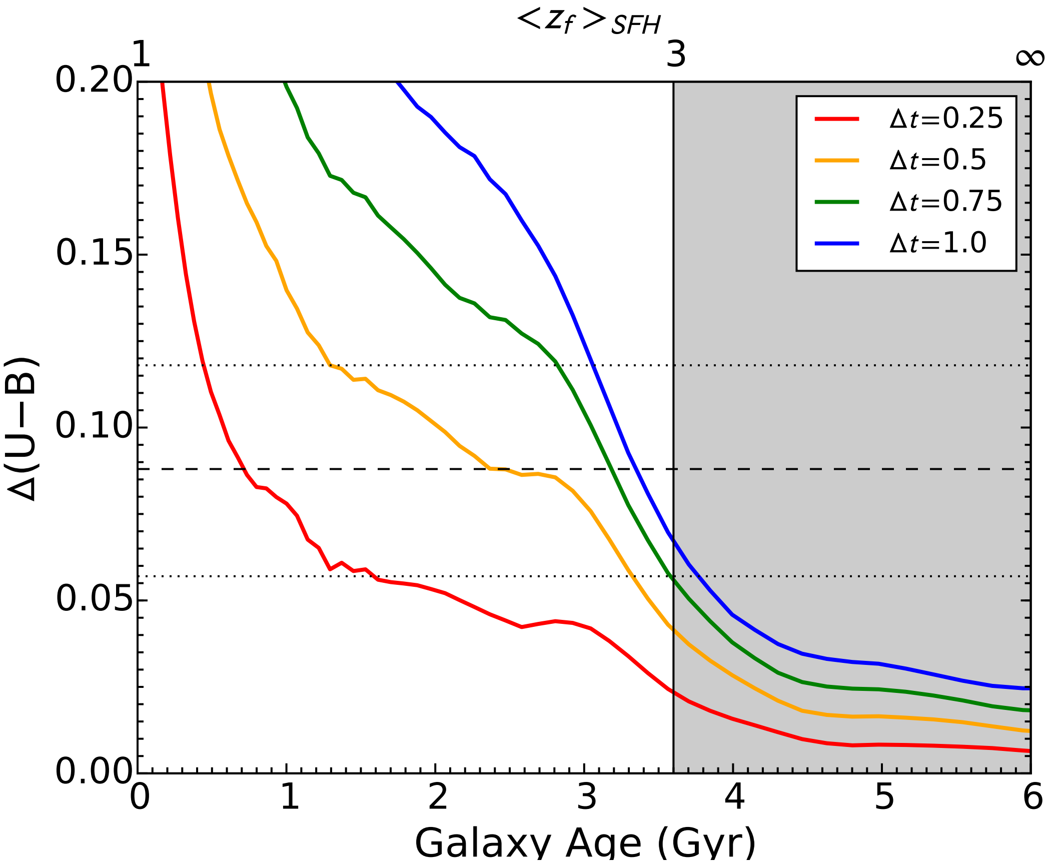

Figure 2.7 Difference in $(U-B)_{z=0}$ color for pairs of model stellar populations with age differences $\Delta t = 0.25, 0.5, 0.75$, and 1.0 Gyr. The age of the younger galaxy model is plotted on the x axis. The vertical solid line is placed at the lower-limit age constraint derived from our zeropoint considerations, such that all viable models must lie in the shaded region. The horizontal lines indicate the biweight mean and 1-σ variation in our MLE-measured $(U-B)_{z=0}$ scatters. From this plot, we see that our measured intrinsic scatter is consistent with an age spread $\Delta t > 1$ Gyr.

ages is plotted in Figure 2.7.

The evolution of this color scatter, and our determination of an age spread, depends on our choice of star formation history. Generally, models with larger τ evolve more slowly, allowing our average $\Delta(U-B)_{z=0}$ color scatter to correspond to a larger spread in age. However, taking all models into account, and assuming that the intrinsic scatter is an age effect, we can constrain the average age spread to be $\Delta t \gtrapprox 1$ Gyr. Note that this is a lower bound : if we allow our galaxies to be older than our lower bound limit of $\langle t \rangle_{\mathrm{SFH}} = 3.6$ Gyr, we could recover the same $\Delta(U-B)_{z=0}$ color scatter by simply allowing a larger spread in ages.

2.3.3 Scatter Evolution

It is clear from Figure 2.7 that color differences due to galaxy age differences are larger when galaxies are younger, and for this reason we expect the intrinsic scatter of the CMR to increase with redshift. However, this is at odds with the apparent lack of evolution in scatter with redshift over our sample (Figure 2.5).

In Figure 2.8 we plot the intrinsic scatter of our sample against that measured by Snyder et al. (2012) and the data compiled by Hilton et al. (2009), including clusters from Mei et al. (2006) and Blakeslee et al. (2003b), and high-redshift clusters from Papovich et al. (2010), Stanford et al. (2012), Zeimann et al. (2012). The scatter data are reported for the $(U-V)_{z=0}$ CMR, so we repeat our rest-frame color derivation and CMR fitting using Johnson U and V filters.

In general, the rest-frame colors and intrinsic scatters for these clusters are not

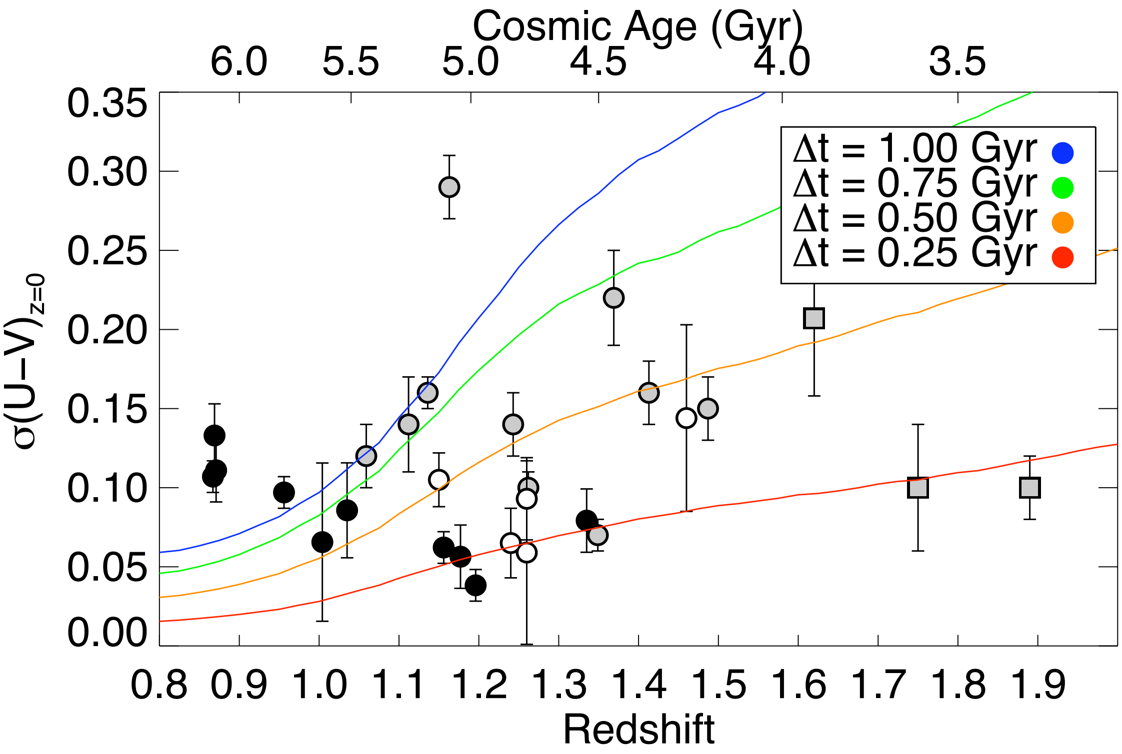

Figure 2.8 Evolution of the color-magnitude relation $(U - V)_{z=0}$ scatter with redshift, compared against values drawn from Snyder et al. (2012) (gray circles), Hilton et al. (2009) (white circles), and Papovich et al. (2010), Stanford et al. (2012), Zeimann et al. (2012) (gray squares). Data from the GCLASS sample are plotted as black circles. The overlaid models show the difference in $(U - V)_{z=0}$ color for pairs of galaxies of different ages (Δt), and therefore trace the passive evolution of a purely age-dependent scatter. The models are averaged over galaxies for $\langle z_f \rangle_{\mathrm{SFH}} > 2$.

determined in a homogeneous manner. Where we have estimated the rest-frame colors from 11-band SED-fitting, rest-frame colors frequently are determined by a linear conversion of an observed color using a synthetic color model. Intrinsic scatter has historically been measured in a variety of different ways, sometimes employing reduced chi-square normalization, although the technique used in this work is more common today. Various criteria are also used to select red-sequence galaxies, either photometrically or morphologically, with different completeness limits. The use of color or σ cuts can bias the measurement of intrinsic scatter.

The overlaid models represent the simple evolution of the $\Delta(U-V)_{z=0}$ color difference between pairs of galaxies of different ages (Δt). The color differences of these model galaxy pairs can be interpreted as evolution tracks of the CMR intrinsic scatter for passively-evolving red-sequences, if we allow that the color scatter is a measure of the red-sequence age spread. While these predicted scatters are dependent to some degree on the formation redshift, the effect is small relative to the inherent uncertainty involved in calculating the intrinsic scatter of the CMR, and so we average the color evolution models over formation redshifts for $\langle z_f \rangle_{\mathrm{SFH}} > 2$.

The models show an increase in scatter with redshift in a manner that depends on Δt. As a whole, the reported scatter values broadly exhibit an increasing trend, in agreement with Hilton et al. (2009), possibly indicating the expected passive evolution. Clearly, no single evolutionary track can connect all of the galaxy clusters in the GCLASS sample, nor is this larger literature sample consistent with a single history.

A possible explanation for this is that our sample exhibits progenitor bias (van

Dokkum et al., 2000; Franx & van Dokkum, 2001) and that younger, bluer galaxies are migrating onto the red-sequence as they are quenched. This would naturally result in an age spread that increases with redshift, which is consistent with the trend seen in Figure 2.8. Furthermore, clusters continuously accrete field galaxies, which may have metallicities and ages that are different from the galaxies within the cluster. The introduction of these galaxies would also potentially increase the scatter.

2.3.4 The Color-Mass Relation

Historically, studies have compared galaxy color as a function of magnitude, with models to infer the properties of quiescent members. However, galaxy properties such as morphology, size, and color also correlate with stellar mass, and it is a more physically meaningful parameter than magnitude. In Figure 2.2 we show the color-mass relation and linear fits for the ten GCLASS clusters (see Table A.3). While previous studies have presented color-mass relations (Borch et al., 2006; Cardamone et al., 2010; Huertas-Company et al., 2010; Strazzullo et al., 2010; Bassett et al., 2013; Cimatti et al., 2013; Moresco et al., 2013), this is the first time to our knowledge that the red-sequence color-mass relation has been fit.

The redshift evolution of this relation's slope, scatter, and zeropoint is shown in Figure 2.9. We plot the biweight mean values of our fit parameters and their 1-σ variation (see Table A.3). We have been unable to find any comparable mass-color fits in the literature to compare with at low redshift, so we are only able to investigate the redshift evolution of the fit over the redshift range spanned by the GCLASS sample. Over this redshift range,

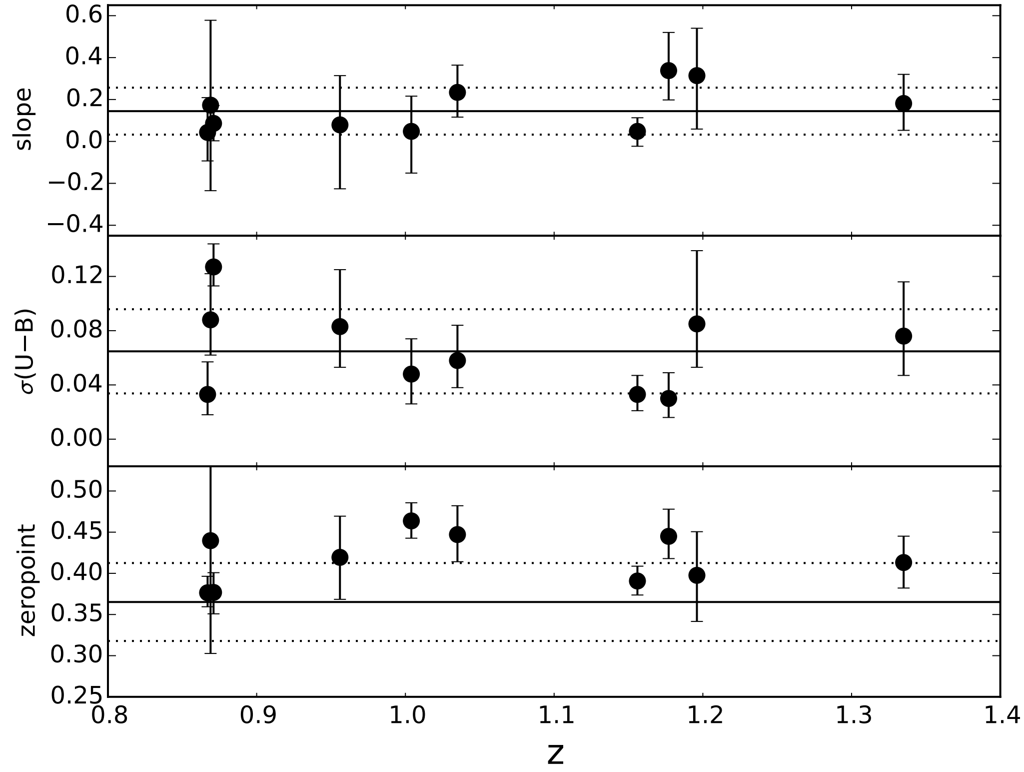

Figure 2.9 Evolution of the color-mass relation slope (top), scatter (middle), and zeropoint (bottom) with redshift. The biweight mean value of the parameters is plotted as a solid line, with dotted lines indicating the 1-σ range.

$0.8 < z < 1.3$, we do not detect any evolution in the color-mass relation. We note that we also do not find any evolution in the color-mag relation over this redshift range (see Section 2.3.1).

2.4 Conclusions

In this chapter we studied the rest-frame U-B color-magnitude and color-mass relations for 10 red-sequence-selected clusters between redshifts $0.8 < z < 1.3$. We compared these results with those from the X-ray-selected ACS IRCS sample (Mei et al., 2009), to look for differences in the properties of red-sequence galaxies in galaxy-selected and gas-selected clusters at $z \sim 1$. From the data analysis presented in this work, we find the following conclusions:

- The fact that we observe no measurable differences between the ages and CMR properties of quiescent cluster members in clusters selected by different methods suggests that, at least at z $\sim$ 1, the dominant quenching mechanism is insensitive to cluster baryon partitioning, favoring processes such as preprocessing or strangulation. The remarkable agreement in color-magnitude zeropoint throughout these cluster samples indicates that the red-sequence method does not preferentially select older, more evolved systems.

- The CMR zeropoints measured for $0.8 < z < 1.3$ allow us to constrain the quiescent members' period of last major star formation to be above $z \sim 3$ for our high-redshift clusters. The observed intrinsic scatters of the CMR in our cluster sample are indicative of an average age spread greater than 1 Gyr.

- The lack of evolution in the intrinsic scatter over $0.8 < z < 1.3$ cannot be explained by simple passive evolution of the red-sequence, indicating possibly a progenitor bias created by younger galaxies migrating onto the red-sequence. This process would result in intrinsic scatters that are consistent with larger age spreads at the lower-redshift end of the sample.

- UVJ color-color classification of quiescent and star-forming galaxy populations broadly agrees with spectroscopic classification based on [O II] emission. From a total sample of 432 spectroscopically-confirmed cluster members, 14% of the UVJ-quiescent population show [O II] emission, while 16% of the UVJ-star-forming galaxies exhibit no [O II] emission.

- We present the color-mass relationship and linear fit parameters for the GCLASS sample. We detect no measurable evolution of the color-mass relationship over the redshift range of the sample, $0.8 < z < 1.3$. The intrinsic scatter of the color-mass relationship agrees with that measured for the color-magnitude relation.

Chapter 3

Quenching timescale

Galaxies form a bimodal distribution in rest-frame color at $z < 2$ (Strateva et al., 2001; Baldry et al., 2004a; Bell et al., 2004a; Williams et al., 2009), meaning galaxies can be broadly categorized as either actively star-forming spirals (the "blue cloud"), or quiescent ellipticals and lenticulars (the "red-sequence"). Although these populations are roughly equivalent in total stellar mass at $z \sim 1$, the quiescent galaxy population has nearly doubled in stellar mass, stellar mass density, and number density over the past ~ 7 Gyr (Bell et al., 2004a; Borch et al., 2006; Bundy et al., 2006; Arnouts et al., 2007; Brown et al., 2007; Faber et al., 2007).

Meanwhile, a variety of studies at intermediate redshift show that galaxy properties correlate with local environment (Cooper et al., 2006, 2007; Quadri et al., 2007; Patel et al., 2009), such that groups and clusters contain more quiescent than active galaxies (George et al., 2011; Muzzin et al., 2012; Presotto et al., 2012; Tanaka et al., 2012; Nantais et al., 2017). Moreover, with increasing cluster-centric radius (decreasing time since infall), observations find a relative reduction in the number of quiescent systems (e.g. Presotto et al., 2012). Together, these results suggest that dense environments shut off (or "quench") star formation in galaxies – a process typically termed "environmental quenching" (Peng et al., 2010).

Environment has been studied extensively as a driver of galaxy evolution (for a review see Blanton & Moustakas, 2009), but the physical mechanism or mechanisms responsible for quenching have yet to be identified, although several candidates have been proposed. Whatever the underlying cause, it must disrupt the process by which a galaxy converts cold gas into stars.

As a galaxy forms stars, its cold gas reservoir is replenished by cooling flows from its surrounding hot gas halo (Bauermeister et al., 2010). One possibility is that this gas is directly removed from a galaxy by ram-pressure stripping as it falls at high speed into the hot intra-cluster medium (ICM) of a cluster environment (Gunn & Gott, 1972). "Strangulation" refers to the removal of the hot gas halo by the cluster environment (Larson et al., 1980; Merritt, 1983; Byrd & Valtonen, 1990). Following the interruption of cooling flows, a galaxy would quench as star formation exhausts the remaining cold gas reservoir over a molecular gas depletion time, $t_{\mathrm{depl}}(\mathrm{H}_{\mathrm{mol}})$. If the hot gas halo is not stripped, the role of the environment may be simply to prevent the accretion of fresh gas onto the galaxy, which would then quench over a longer total gas depletion time $t_{\mathrm{depl}}(\mathrm{H}_{\mathrm{I}} + \mathrm{H}_{\mathrm{mol}})$.

It is also possible that gas-dynamical feedback and outflows play a central role in removing the gas from galaxy halos (McGee et al., 2014; Balogh et al., 2016). In this "overconsumption" scenario, the depletion of gas is augmented by outflows produced by star formation, either directly through radiation pressure or from subsequent supernovae McGee et al. (2014). Quenching then proceeds over an accelerated gas depletion timescale that is inversely proportional to the star formation rate (SFR).

These processes would quench galaxies over different timescales. Measuring the quenching timescale, t_Q, is therefore one approach to identifying which possible mechanisms may be responsible for quenching. This strategy benefits from the fact that the redshift dependence of these timescales is such that differences will become more apparent at high redshift. Nantais et al. (2016, 2017) finds a strong evolution in environmental quenching efficiency between $0.9 < z < 1.6$, while over a similar redshift range Cerulo et al. (2016, 2017) reports an accelerated build-up of the red-sequence in clusters, and Balogh et al. (2016) finds evidence for a change in the environmental quenching mechanism at $z \sim 1$. Measuring t_Q at high redshift is clearly essential to our understanding of environmental quenching.

In this work, we will measure the quenching timescale in a sample of four galaxy clusters at $z \sim 1.6$, a higher redshift than has been studied previously. We will use our results, together with studies drawn from the literature, to investigate the redshift evolution of t_Q and compare with the timescales predicted by various quenching mechanisms.

The structure of this chapter is as follows: Our data set is described in Section 3.1. In Section 3.2, we summarize our toy model of environmental quenching, which is described in detail in Appendix B. In Section 3.3 we report the results of our technique, which we discuss in Section 3.4. In Section 3.5 we summarize our conclusions.

In this work we will assume a standard ΛCDM cosmology with $H_0 = 70\text{km} \cdot \text{s}^{-1} \cdot$

Mpc^{-1}, $\Omega_M = 0.3$, and $\Omega_\Lambda = 0.7$, and a Chabrier IMF (Chabrier, 2003) throughout. Our magnitudes are reported in the AB system (Oke & Gunn, 1983).

3.1 Data

The galaxy clusters studied in this work were identified using the Stellar Bump Sequence technique described in detail in Muzzin et al. (2013a, see also Papovich 2008). Four high-redshift cluster candidates (see Table 3.1) were identified within the *Spitzer* Adaptation of the Red-Sequence Cluster Survey (SpARCS; Wilson et al., 2009; Muzzin et al., 2009) using a two-color cut on *Spitzer* IRAC 3.6 μm - 4.5 μm color and z' - 3.6 μm color. Spectroscopic follow-up was performed using the MOSFIRE (McLean et al., 2010, 2012) spectrograph on the Keck Telescopes and the Focal Reduction and Imaging Spectrograph 2 (FORS2, Appenzeller et al. 1998) on the European Southern Observatory (ESO) Very Large Telescope (VLT). Spectra were also obtained from the OzDES survey (Yuan et al., 2015; Childress et al., 2017).

3.1.1 Photometric Catalogs

Spectroscopic confirmation of these clusters was followed by collecting optical imaging data in u' g' r' i' bands. For SpARCS-J0330, SpARCS-J0224, and SpARCS-J0335, these data were taken with IMACS at Magellan/Baade, while for SpARCS-J0225 these data come from the Canada-France-Hawaii Telescope (CFHT) Legacy Survey (CFHTLS) which used MegaCam on CFHT. All four clusters were imaged in near-infrared Y-, and Ks-band with HAWK-I at VLT, with additional J-band photometry taken for SpARCS-J0224 and

Table 3.1. Description of the $z \sim 1.6$ SpARCS cluster sample

Cluster	R.A.	Decl.	z	Spectroscopy	Photometry	Spectra[a]	N^{b}_{spec}
SpARCS-J0224	02:24:26.33	-03:23:30.8	1.633	MOSFIRE, FORS2, OzDES	*ugrizYJKs* [3.6] [4.5] [5.8] [8.0]	187	52
SpARCS-J0330	03:30:55.87	-28:42:59.5	1.626	MOSFIRE, FORS2, OzDES	*ugrizYJKs* [3.6] [4.5] [5.8] [8.0]	535	40
SpARCS-J0225	02:25:45.55	-03:55:17.1	1.598	MOSFIRE, FORS2, OzDES	*ugrizYKs* [3.6] [4.5] [5.8] [8.0]	126	22
SpARCS-J0335	03:35:03.58	-29:28:55.6	1.369	FORS2, OzDES	*grizYKs* [3.6] [4.5] [5.8] [8.0]	81	22

[a] Number of spectra.

[b] Number of spectroscopically-confirmed cluster members.

SpARCS-J0330. Our photometry also includes the IRAC data from the Spitzer Wide-area Extragalactic Survey (SWIRE; Lonsdale et al., 2003) with additional deeper observations in IRAC 3.6 and 4.5 μm bands as part of the *Spitzer* Extragalactic Representative Volume Survey (SERVS), and z'-band data from the SpARCS survey taken by the MOSAIC-II camera at the Cerro Tololo Inter-American Observatory (CTIO).

As described in detail in Nantais et al. (2016), the imaging data were combined into a PSF-matched photometric catalog by first using Source Extractor (Bertin & Arnouts, 1996) to detect sources in the K_s-band data. Astrometric and pixel-scale matching was performed on all images using SWarp (Bertin et al., 2002) prior to photometry. PSF matching was performed using IRAF to generate convolution kernels before matching u' g' r' i' z' Y J Ks band data to the poorest image quality among these bands. Aperture photometry was performed using Source Extractor in dual-image mode and was corrected for Galactic extinction using Schlegel et al. (1998) dust maps and a Schlafly & Finkbeiner (2011) extinction law. Robust photometric errors were calculated by directly measuring the 1-σ variation in background flux in randomly-placed apertures that do not contain any sources.

The resulting catalog has photometry in u' g' r' i' z' Y J Ks and 3.6, 4.5, 5.8, 8.0 μm. We perform an RA/DEC matching to the FORS2 and MOSFIRE spectroscopic data to associate spectroscopic redshifts to galaxies where possible. Altogether there are 136 spectroscopically-confirmed members across the four clusters in this sample (see Table 3.1).

3.1.2 Photometric Redshifts

With the publicly-available photometric redshift code EAZY (Brammer et al., 2008), we fit the broadband photometry of each object in our photometric catalog to a linear combination of seven basis templates derived from the prescription in Blanton & Roweis (2007). These templates have been optimized for deep optical-NIR broad-band surveys, and this code was optimized specifically for K_s-selected samples such as our own. The output of this code includes the best-fit SED, a photometric redshift, and the photometric redshift probability distribution function of the object. When a spectroscopic redshift is available, EAZY fixes the best-fit redshift to this value.

Photometric Redshift Membership Criteria

For our analysis, we require a cluster galaxy selection that minimizes bias for either star-forming or quiescent galaxies. We therefore adopt the photometric cluster membership criteria that van der Burg et al. (2013b) and Nantais et al. (2016, 2017) used previously with this data set, and consider galaxies to be cluster members if $(z_{\mathrm{phot}} - z_{\mathrm{cluster}})/(1 + z_{\mathrm{cluster}}) \leq 0.05$. This membership criteria attempts to avoid biasing our sample, while using a range in photometric redshifts that closely matches the scatter of our photometric redshifts ($\sigma \sim 0.04$). The choice of 0.05 does not drive the results of this work, and repeating the analysis for cutoff values between 0.05 and 0.1 does not change our conclusions.

The selection necessarily introduces some contamination by field galaxies due to uncertainty in the photometric redshift estimates. The present work relies on ratios of the star-forming and quiescent population, which will be largely unaffected if this contamination is not biased toward either galaxy type. A previous analysis by van der Burg et al. (2013b) of a comparable data set and method shows that the overall rate of false positives and negatives is small and largely insensitive to galaxy type at $z \sim 1$, suggesting that this selection introduces minimal error to our conclusions.

3.1.3 Rest-Frame Colors and UVJ Classification

We perform a preliminary classification of star-forming and quiescent galaxies using the rest-frame UVJ method. First we infer rest-frame absolute magnitudes for each cluster member by convolving its best-fit SED (derived using EAZY) with filter curves at the redshift of each galaxy. We note that the span of the observed filters ensures that rest-frame magnitudes are interpolated from the available data, often overlapping with multiple observed passbands.

The classification is accomplished by dividing the space of rest-frame U-V and V-J colors into a star-forming and a quiescent region. The cuts we use to define these regions have been empirically calibrated by Williams et al. (2009) for the redshift ranges of our clusters, and are tuned to maximally reflect the bimodality of galaxy populations out to $z \sim 2.5$. UVJ-based classification is frequently used to classify star forming and quiescent galaxies in surveys when spectroscopic or morphological information is not available (Wuyts et al., 2007; Williams et al., 2009; Whitaker et al., 2011; Patel et al., 2012; van der Burg et al., 2013a; Whitaker et al., 2013; Muzzin et al., 2013b; Strazzullo et al., 2013).

In Figure 3.1, we plot rest-frame U-V vs M_J color-magnitude diagrams for all cluster members in the sample, with inset rest-frame U-V versus V-J color-color diagrams. Galaxies are colored according to their UVJ classification, separating into a red-sequence and blue cloud.

3.1.4 Stellar Masses and Dust Reddening

Using the publicly-available SED fitting code FAST (Kriek et al., 2009), we fit the 12-passband photometry of each cluster to Bruzual & Charlot (2003b, hereafter BC03) stellar population synthesis templates. FAST proceeds by generating a grid of synthetic SEDs of stellar populations at the redshift of each galaxy from the given population synthesis templates, for a range of star formation histories (SFH), ages, and masses, with possible additional variation in dust attenuation and/or metallicity. Best-fit stellar populations are then selected from this grid by minimizing χ^2 when comparing the synthetic SED to the observed broad-band photometry of a given galaxy.

For our grid of parameters, we use a range of ages from 100 Myr to 10 Gyr (excluding ages greater than the age of the universe at the observed redshift) and an $\mathrm{A_V}$ ranging from 0 to 3 mag with a Calzetti extinction law (Calzetti, 2001). Throughout, we assume an exponentially-declining star formation history, along with a Chabrier IMF (Chabrier, 2003) and fixed (solar) metallicity of 0.02.

In the U-V versus M_J color-magnitude diagram of Figure 3.1, galaxies segregate into a blue cloud and red-sequence. The colors of these two populations reflect the underlying bimodal distribution in star formation rate, but this picture is complicated by the presence of star-forming galaxies with dust-reddened colors. We therefore find it illustrative to plot the dust-corrected U-V versus M_J color-magnitude diagram in Figure 3.2. To correct the photometry for dust, we first calculate the dust extinction in U and V bands for each galaxy from the total V-band extinction ($\mathrm{A_V}$, determined through SED fitting),

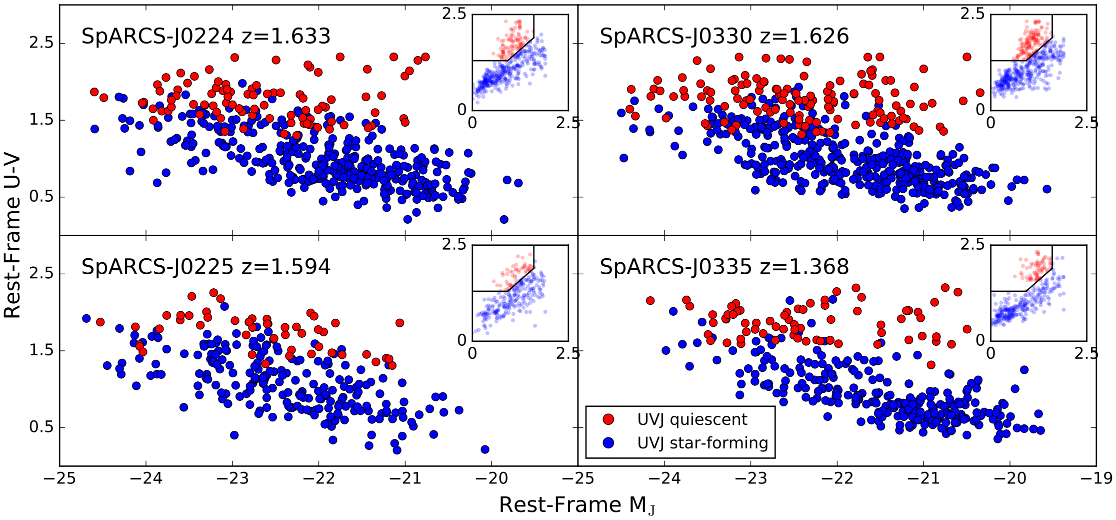

Figure 3.1 Rest-frame U-V versus absolute J magnitude ($\mathrm{M_J}$) diagram for all photometric-redshift-selected cluster members of the four clusters in the sample (see Table 3.1). The inset panels show rest-frame U-V versus V-J color-color diagrams, and galaxies are colored red (quiescent) or blue (star-forming) according to their U-V and V-J colors (see Section 3.1.3). The mass completeness of our sample corresponds roughly to a magnitude limit of $M_J \lesssim -23$.

using a Calzetti extinction law (Calzetti, 2001). We then subtract the contribution from dust from each galaxy's rest-frame U and V magnitudes to derive the dust-corrected values of these magnitudes and colors.

Comparing Figures 3.1 and 3.2, we note that the red-sequence is mostly unaffected by dust subtraction, as the quiescent population generally exhibits little dust reddening to begin with. The blue cloud becomes brighter, with dust corrections between $0-2$ magnitudes, and spans a wider range in M_J, while exhibiting decreased scatter in U-V color. The UVJ-star-forming and UVJ-quiescent populations separate more cleanly in color-magnitude space following dust subtraction, exposing the intermediate green valley.

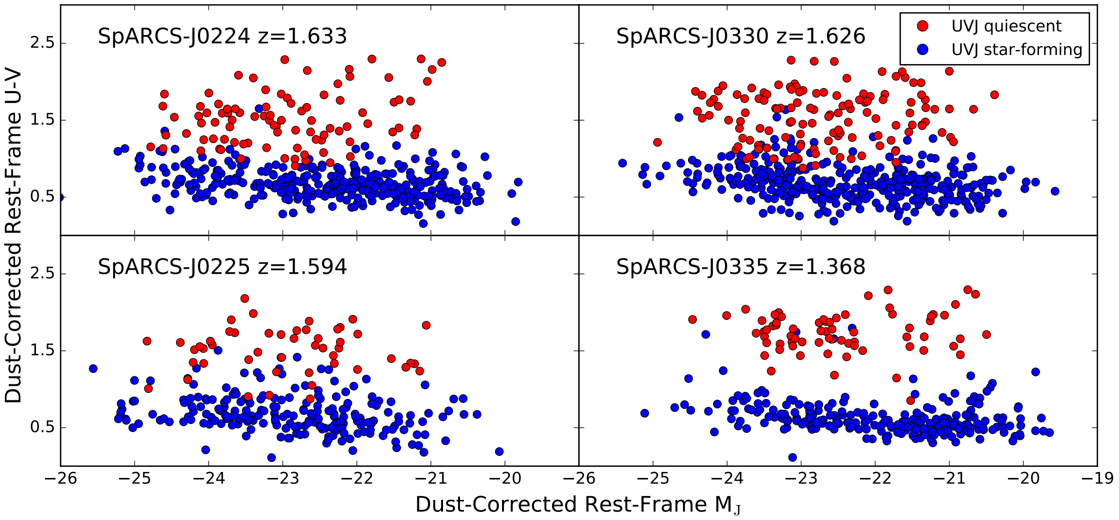

Figure 3.2 Dust-corrected rest-frame U-V versus absolute J magnitude ($\mathrm{M_J}$) diagram for the four clusters in our sample. Galaxies are colored as in Figure 3.1. Photometry is corrected for dust using a Calzetti (Calzetti, 2001) extinction law with $\mathrm{A_V}$ determined from SED fitting (see Section 3.1.4). Compared to Figure 3.1, the blue cloud reaches brighter magnitudes and exhibits smaller scatter in U-V color. The separation between the UVJ-star-forming and UVJ-quiescent populations is more apparent following dust subtraction.

3.2 Analysis

In this section we describe the method used to measure the quenching timescale t_Q. In Section 3.2.1, a toy model relates the number of star-forming, intermediate, and quiescent cluster members to a quenching timescale. In Section 3.2.2 we describe cluster member classification and counts. In Section 3.2.3 we describe our clustercentric radial cut, and a background subtraction is described in Section 3.2.4. Section 3.2.5 describes how we derive confidence intervals for t_Q with a Monte Carlo method.

3.2.1 Environmental Quenching Model and Mass Completeness Limit

A galaxy that is actively forming stars will have blue optical colors dominated by the bright contributions of short-lived O- and B-class stars. After the onset of quenching, a galaxy's colors will become redder as these high-mass stars exhaust their hydrogen fuel and leave the main sequence, without new stars to replace them. Eventually, a quiescent galaxy's color will reflect primarily the red colors of low-mass, long-lived main sequence stars and red giants. We define the quenching timescale as the time since first infall after which galaxies are quenched. In this section, we provide a conceptual summary of the method we use to measure t_Q, and refer the reader to Appendix B for details.

Recent work has shown that environmental quenching can be described by two principal timescales, a "delay time" (t_D) and a "fade time" (t_F) (Wetzel et al., 2013; McGee et al., 2014; Mok et al., 2014; Haines et al., 2015; Balogh et al., 2016; Fossati et al., 2017). In our model, a star-forming (blue) galaxy that is accreted by the cluster will remain blue for a time t_D following infall, after which the onset of quenching causes it to become an intermediate (green) galaxy. The galaxy will remain green for a time t_F, until star formation has ceased and it is quiescent (red). This model of environmental quenching is shown schematically in Figure 3.3. The total quenching time t_Q, defined as the length of time after accretion until a galaxy is completely quenched, is then $t_D + t_F$.

We assume that infalling galaxies are accreted from the field. Not every galaxy accreted from the field will be star-forming, especially at higher stellar masses, and lower redshifts. We wish to eliminate from consideration those galaxies that were quenched in the field before they were accreted by the cluster. It is possible to account for this by removing a fraction of quiescent galaxies proportional to the field quiescent fraction. This fraction can be calculated from the COSMOS/UltraVISTA (**?**) field galaxy mass functions computed by Muzzin et al. (2013c).

Following the above considerations, the observed number counts of blue and green galaxies in a cluster are proportional to the length of time a galaxy spends in the delay and fade phases. For example, a long fade time would make it easier to catch galaxies in the process of quenching, leading to larger observed numbers of green galaxies in a cluster. To fully quantify these timescales, one needs to control for the galaxy accretion rate of a cluster, as a higher accretion rate leads to larger numbers of all types of galaxies. With the added assumption of a cluster galaxy infall rate, the number counts of red, green, and blue galaxies can constrain the timescales t_D and t_F.

Given that blue galaxies have not resided in the cluster any longer than one t_D, their number will be equal to the cluster galaxy accretion rate $\mathrm{d}N/\mathrm{d}t$ integrated between the time of observation and one t_D earlier. In a similar manner, the number of green galaxies

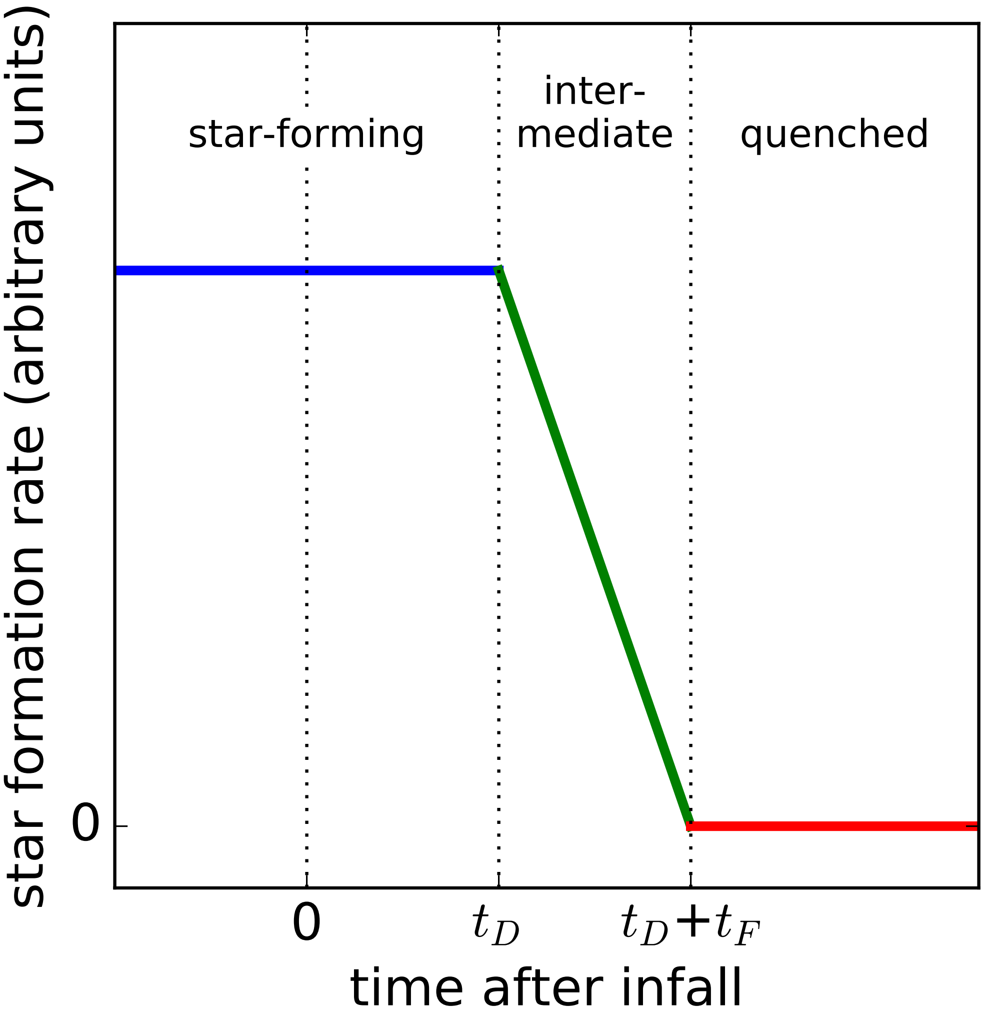

Figure 3.3 Model of galaxy star formation rate as a function of time since infall. In this model, galaxies are star-forming and blue before being accreted by a cluster. They remain blue for a time t_D, the delay time, before they start to quench and become green. After a further time t_F, the fade time, star formation has ceased and the galaxy becomes red.

will be equal to the galaxy accretion rate integrated between one t_D and one $t_D + t_F$ earlier. The red galaxies trace all mass accreted earlier than one $t_D + t_F$ ago. We write

$$\begin{aligned} B &= \int_{-t_D}^{0} \mathrm{d}N/\mathrm{d}t \; \mathrm{d}t \\ G &= \int_{-(t_D+t_F)}^{-t_D} \mathrm{d}N/\mathrm{d}t \; \mathrm{d}t \\ R &= \int_{-t_H}^{-(t_D+t_F)} \mathrm{d}N/\mathrm{d}t \; \mathrm{d}t \end{aligned}$$

where R,G, and B are the number of red, green, and blue galaxies respectively, t_H is the Hubble time, and negative signs indicate that these galaxies were accreted in the past.

We assume that the cluster galaxy accretion rate $\mathrm{d}N/\mathrm{d}t$ is proportional to the cluster halo mass accretion rate $\mathrm{d}M/\mathrm{d}t$ as derived from the Millennium-II simulation by Fakhouri et al. (2010). From there, ratios of the observed numbers of R, G, and B galaxies can be related to $\mathrm{d}M/\mathrm{d}t$, t_F, and t_D, to constrain the fade and delay times and thereby the total quenching time. In Appendix B we more fully describe this toy model, which is ultimately defined by a set of four equations, (B.1) – (B.4). Given a number of R, G, and B galaxies, a cluster redshift, and a mass accretion rate, Equations (B.1) – (B.4) can be solved for t_F, t_D, and t_Q.

Before proceeding with the analysis, we note several considerations which must be taken into account with this model. The 80% mass completeness of our sample is defined as the lowest mass for which passive galaxies yield accurate passive fractions (van der Burg et al., 2013a). This limit varies from $10^{10.3}$ to $10^{10.5}$ $\mathrm{M}_{\odot}$ within our sample (van der Burg et al., 2013a; Nantais et al., 2016), due to variations in exposure time. We must restrict our analysis to galaxies with masses above these limits, to ensure a fair comparison between the quenched and not-yet-quenched galaxies.

Second, it has been shown that the environmental quenching timescale varies with satellite galaxy mass (De Lucia et al., 2012; Wetzel et al., 2013; Wheeler et al., 2014; Fillingham et al., 2015), and it is therefore inaccurate to refer to a singular environmental quenching timescale for all galaxies. Any quenching timescale measured with the above toy model will necessarily be for an ensemble of galaxies spanning some range in stellar mass. However, the quenching timescale does not vary much over the small dynamical range in mass studied in this work, at least at low redshift (e.g. see Fig. 8 of Fillingham et al., 2015; Wetzel et al., 2013, Figure 5).

Third, the mass dependence must be considered when comparing with results of different studies. Comparing with other studies will allow us to investigate the evolution of t_Q with redshift (see Section 3.4). Other measurements of t_Q will not be comparable to our results unless they were derived for a similar mass range.

For the above reasons, when measuring t_Q we restrict our sample to galaxies with stellar masses above a mass completeness limit $M_* \geq 10^{10.5}$ $\mathrm{M}_\odot$. This cut conservatively ensures that we are sampling above the mass completeness of our photometry for each cluster, and allows comparison with various results in the literature that report the quenching timescale for this range of masses.

In general, environmental quenching is likely the result of several different mechanisms operating over different timescales and environments (Schawinski et al., 2014; Paccagnella et al., 2016, 2017). A toy model such as the one presented here is not intended to be a final description of environmental quenching, but instead to investigate which physical scenarios, if any, are consistent with a set of very simple assumptions.

3.2.2 Classification of Galaxies as Star-Forming, Intermediate, or Quiescent

The environmental quenching model described in Section 3.2.1 and Appendix B relates the number of observed star-forming (blue), intermediate (green), and quiescent (red) cluster members to the delay and fade times, t_D and t_F. A method of classifying galaxies as red, green, or blue is therefore needed before we can solve for the quenching timescale, t_Q.

A common approach to identifying star-forming, intermediate, and quiescent galaxies is to categorize them according to their colors and magnitudes, in a manner informed by galaxy evolutionary models. A successful classification scheme will distinguish between star-forming galaxies that appear red due to dust, and galaxies that are red from a lack of star formation. In this section we introduce a classification based on dust-corrected rest-frame colors derived from SED fitting (see Sections 3.1.3 and 3.1.4).

Each galaxy's best-fit SED parameters include the V-band dust reddening $\mathrm{A_V}$, which we use in conjunction with a Calzetti extinction law (Calzetti, 2001) to determine the reddening in U- and B-bands. Subtracting this reddening from the rest-frame photometry breaks the color degeneracy between dusty, star-forming galaxies and old, quiescent galaxies. Following dust-subtraction, galaxies separate more cleanly into a red-sequence, green valley, and blue cloud in a color-magnitude diagram, such as those shown in Figure 3.2. We can therefore use cuts in dust-corrected color-magnitude space to label galaxies red, green, or blue.

To define these cuts, we start by applying a spectral clustering algorithm to the dust-corrected color-magnitude diagram of all galaxy cluster members. This algorithm labels the two principal clusters of data points, identified in this case with the blue cloud and red-sequence. We then fit an elliptical region to each cluster of data points by finding the eigenvectors of the covariance matrix of the set of points, which define the semi-major and semi-minor axes of an ellipse. The width and height of this ellipse are scaled so that the ellipse represents a 95% (3-σ) confidence level.[1] Galaxies are categorized as either star-forming or quiescent according to their membership in these elliptical regions. We define the green valley as the overlapping area of these ellipses, and galaxies within this region are categorized as intermediate. In Figure 3.4 we plot the classification regions over the dust-corrected rest-frame colors and magnitudes of all cluster members.

For comparison, we include on this plot a BC03 evolutionary track for a stellar population with a star formation rate that remains constant for 6 Gyr, after which it truncates (quenches). There is a clear agreement between the model's stage of evolution and its progressive classification from blue, to green, to red. In its star-forming phase, a galaxy stays in the blue region, and doesn't enter the green (intermediate) region until it is quenched. After quenching, the model crosses the green valley in ~ 0.2 Gyr. The straightforward nature of galaxy evolution in this dust-subtracted color-magnitude space is the primary advantage of this classification scheme, which identifies an unambiguous green valley between the blue cloud and red-sequence.

These elliptical regions define the star-forming, quiescent, and intermediate popu-

---

[1] Specifically, the length of each axis is $6\sqrt{\lambda}$, where λ is the eigenvalue of the axis's eigenvector.

lations, and therefore the final value of t_Q depends on their precise contours. The total value of t_Q is set by the location of the border between the green and red population, while the blue-green border, determining the fraction of star-forming galaxies that are intermediate, affects the way t_Q is subdivided into t_D and t_F. Through repeated experimentation, we determine that the results are robust to reasonable tweaks in the contours of these ellipses, which affect the result within error bars. The red-green border necessarily lies in the green valley, a region of low galaxy number density, where adjustments to this border do not affect the bulk of galaxies considered quenched or star-forming, therefore having little effect on their ratio.

UVJ-based Classification

Rest-frame U-V versus V-J color-color diagrams can also be used to classify star-forming and quiescent galaxies (see Section 3.1.3), suggesting the possibility of using UVJ classification in place of the dust-corrected color-magnitude classification of Section 3.2.2. However, the location of the green valley in UVJ space is not clear.

This alone is not fatal to the prospect of applying UVJ classification to the quenching model, as the model can be simplified to forgo the use of green galaxies. This simplification comes at the cost of being unable to constrain separate delay and fade times t_D and t_F, instead directly measuring the total quenching time, t_Q. When this simplified model is used in conjunction with number counts of UVJ-star-forming and UVJ-quiescent galaxies, the result mostly agrees with that derived for the above dust-corrected color-magnitude classification.

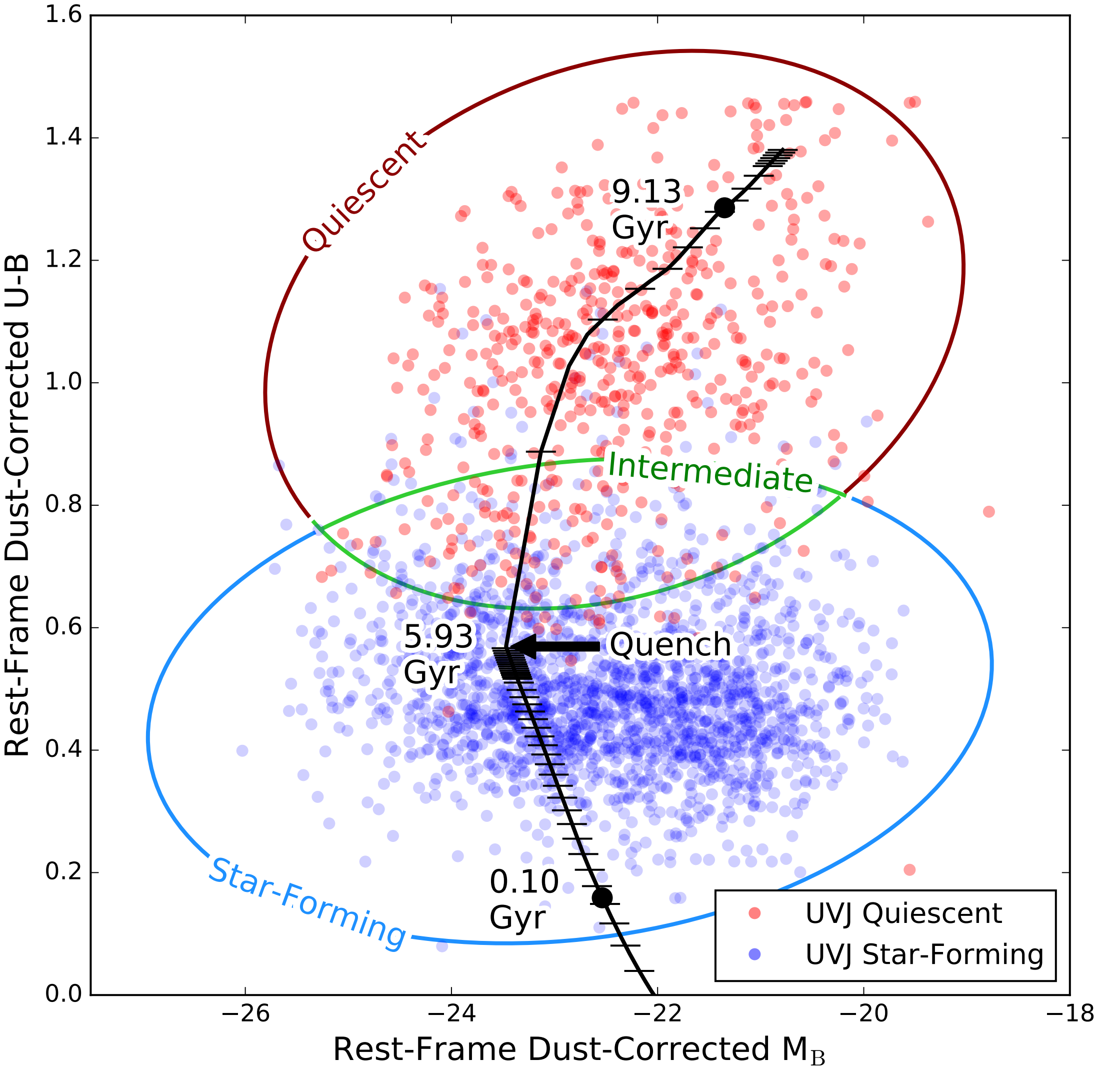

Figure 3.4 Classification of star-forming, intermediate, and quiescent galaxies. We plot the dust-corrected rest-frame *U-B* versus absolute *B* magnitude for all cluster members. Points are colored according to galaxies' *UVJ* classifications (see Section 3.1.3). The colored lines show 3-σ elliptical fits to the two principal clusters of data points identified by a spectral clustering algorithm. The elliptical regions define the quiescent, intermediate, and star-forming populations of galaxies, as labeled. The solid black line is a BC03 model evolutionary track for continual star formation that truncates after 6 Gyr. The black line is punctuated by dashes indicating time intervals evenly spaced in redshift. The black points on this line mark when the model is is 0.10 and 9.13 Gyr old. This track demonstrates good agreement between the model's star formation rate and its progressive classification from blue, to green, to red. Note that even after 6 Gyr of constantly-integrated star formation, the model remains fully within the star-forming ellipse, only leaving it after quenching.

For details on both of these points, we refer the reader to Appendix C. This subject will be further elaborated in a letter (Foltz 2018, in prep).

3.2.3 Projected Radial Distance Cut

A cluster galaxy's type correlates with clustercentric distance. We wish to compare and combine galaxy number counts across multiple clusters and cluster samples, and therefore must control for galaxies' locations within the cluster. Although a cut based on galaxies' positions relative to the cluster's virial radius is commonly used for this purpose, it is unlikely that the clusters in the high-redshift cluster sample are completely virialized structures. Because of this, it would not be meaningful to naively ascribe virial radii to the velocity dispersions that we measure.

We therefore test our method using a variety of cuts on physical clustercentric distance, $r \leq 1000$ kpc, $r \leq 1500$ kpc, and $r \leq 2000$ kpc. The choice of radial cut does not greatly affect the results of our analysis, and so we choose to restrict our consideration to galaxies with $r \leq 2000$ kpc.

3.2.4 Background Subtraction

Our number counts are contaminated by the inclusion of field galaxies due to inherent uncertainty in our photometric-redshift selection. Before determining the quenching timescale we need to subtract the field galaxy background. We therefore adjust the number counts for each cluster to correct for field contamination estimated from the field galaxy survey catalogs from UltraVISTA/COSMOS (Muzzin et al., 2013b).

To estimate the number of field galaxies included in the cluster sample, we start by cropping a randomly-selected section of the Ultra-VISTA/COSMOS dataset to match the angular size of the cluster photometry. We process the Ultra-VISTA/COSMOS photometry with EAZY and FAST (see Sections 3.1.2 and 3.1.4) to determine photometric redshifts, rest-frame colors, and masses, limiting the data set to the same photometric bands that are available in the main dataset. We then select field galaxies from this sample at the redshift of the cluster based on the same photometric redshift criterion described in Section 3.1.2. These field galaxies are classified as star-forming, intermediate, or quenched, according to the dust-corrected color-magnitude cuts detailed in Section 3.2.2. We then subtract these numbers of red, green, and blue field galaxies from the corresponding numbers of cluster galaxies.

3.2.5 Uncertainty Calculation

Shown in detail in Appendix B, the numbers of red, green, and blue cluster galaxies, together with a cluster redshift, fully determine a quenching timescale. The uncertainty in t_Q is driven by uncertainty in these number counts, and we therefore use a Monte Carlo method to estimate the 68% confidence interval for t_Q.

For each cluster, we create 200 simulated data sets consisting of numbers of red, green, and blue number counts, each drawn from Poisson distributions centered on the background-subtracted numbers of red, green, and blue galaxies. For each simulated data set we substitute the values for R, G, and B into Equations (B.1) – (B.4) and solve for t_Q, arriving at a distribution in t_Q. The central 68% of this distribution then defines the upper and lower confidence intervals for t_Q.

Table 3.2. Quenching timescale measured in the SpARCS and GCLASS cluster samples

Sample	N[a]	N[a]	$\bar{z}$	R[b]	G[b]	t_D (Gyr)	t_F (Gyr)	t_Q (Gyr)
GCLASS	10	1.04	160	42	38	$0.69^{+0.13}_{-0.13}$	$0.80^{+0.15}_{-0.18}$	$1.50^{+0.19}_{-0.18}$
SpARCS high-redshift	4	1.55	79	17	63	$0.94^{+0.20}_{-0.18}$	$0.29^{+0.14}_{-0.15}$	$1.24^{+0.23}_{-0.20}$

[a] Number of galaxy clusters in the sample.

[b] Number of red, green, or blue galaxies above the mass completeness limit.

3.3 Results

Here we report the results of the quenching timescale modeling described in Section 3.2.1. In Section 3.3.1 we report the measured quenching timescale for our high-redshift sample. In Section 3.3.2 we report the quenching timescale measured in a sample of galaxy clusters at $z \sim 1$, and compare with a previous, independent measurement of the same reported by Muzzin et al. (2014b).

The results are summarized in Table 3.2.

3.3.1 Quenching timescale at $z = 1.55$

We start by selecting cluster members according to the photometric redshift probability cut defined in Section 3.1.2. We classify galaxies as red, green, or blue according to their colors and magnitudes by the method described in Section 3.2.2. We stack the sample by taking the total number of red, green, and blue galaxies at the mean redshift of the cluster sample, $z_c = 1.55$. We substitute these values for R, G, B, and z_c into Equations (B.1) – (B.4) and solve for t_Q, finding a quenching timescale of $t_Q = 1.24^{+0.23}_{-0.20}$ Gyr for this sample.

3.3.2 Quenching timescale at $z = 1.0$

The Gemini Cluster Astrophysics Spectroscopic Survey (GCLASS, Muzzin et al., 2012) is a sample of 10 red-sequence-selected clusters at $0.87 < z < 1.34$, initially detected by the SpARCS optical/IR cluster survey using the cluster red-sequence detection method developed by Gladders & Yee (2000) (see Muzzin et al., 2009; Wilson et al., 2009; Demarco et al., 2010). GCLASS forms a complimentary data set to the $z \sim 1.6$ SpARCS sample, having a similar range of optical to far-infrared photometry and catalogs prepared in a homogeneous manner (see Muzzin et al., 2012; van der Burg et al., 2013a; Nantais et al., 2016, 2017). With this data set, we can compare quenching timescales at $z \sim 1.6$ and $z \sim 1$.

Using the GCLASS spectroscopic and photometric catalogs, we performed the same cluster member selection and categorization of Sections 3.1.2 and 3.2.2. We then use the total number of red, blue, and green galaxies above the mass completeness limit $M_* \geq 10^{10.5}$ $\mathrm{M}_\odot$ to measure a quenching timescale according to Equations (B.1) – (B.4), finding $t_Q = 1.50^{+0.19}_{-0.18}$ Gyr at $z \sim 1$.

A previous analysis by our team has independently measured the quenching timescale in this sample. Muzzin et al. (2014b) identified spectroscopic cluster members with absorption line features indicative of recent, rapidly-truncated star formation. The distribution of these "post-starburst" galaxies in phase space, when compared with the phase space of zoom simulations, indicated a quenching timescale of $\sim 1 \pm 0.25$ Gyr. This result is largely independent of the measurement performed in this present work, as it was derived using galaxies' spectroscopic features and positions within the cluster. The agreement between these methods is therefore a strong indicator that they independently measure the same timescale, corresponding to the quenching time.

3.4 Discussion

Based on the results of Section 3.3, the quenching timescale for massive satellite galaxies ($M_* \geq 10^{10.5}$ M$_\odot$), measured in a homogeneous manner across cluster samples, is ~ 1.5 Gyr at $z \sim 1$ and ~ 1.2 Gyr at $z \sim 1.6$. These quenching times are required to produce the observed number of quenched galaxies in our cluster sample, given a reasonable model of the mass accretion histories of clusters. We plot the evolution of the cluster quenching timescale with redshift in Figure 3.5.

3.4.1 Redshift Evolution of Observed Quenching Timescales

Included on Figure 3.5 are several quenching timescales drawn from other studies. We note several possible sources of confusion that must be accounted for when drawing fair comparisons between timescales reported in the literature. Historically, researchers have used several different approaches to modeling or measuring the quenching timescale, and occasionally even different definitions of the quenching timescale itself. We have taken t_Q to be the time following infall for a galaxy to be classified quiescent, and following Wetzel et al. (2013), describe it with a "delay" followed by a "fade" phase. Other formalisms have been adopted, such as "slow quenching" scenarios where galaxies begin quenching immediately upon infall, having star-formation rates that decline gradually with an exponential time constant (often also called the "quenching time").

These considerations are additional to the normal systematic differences in galaxy

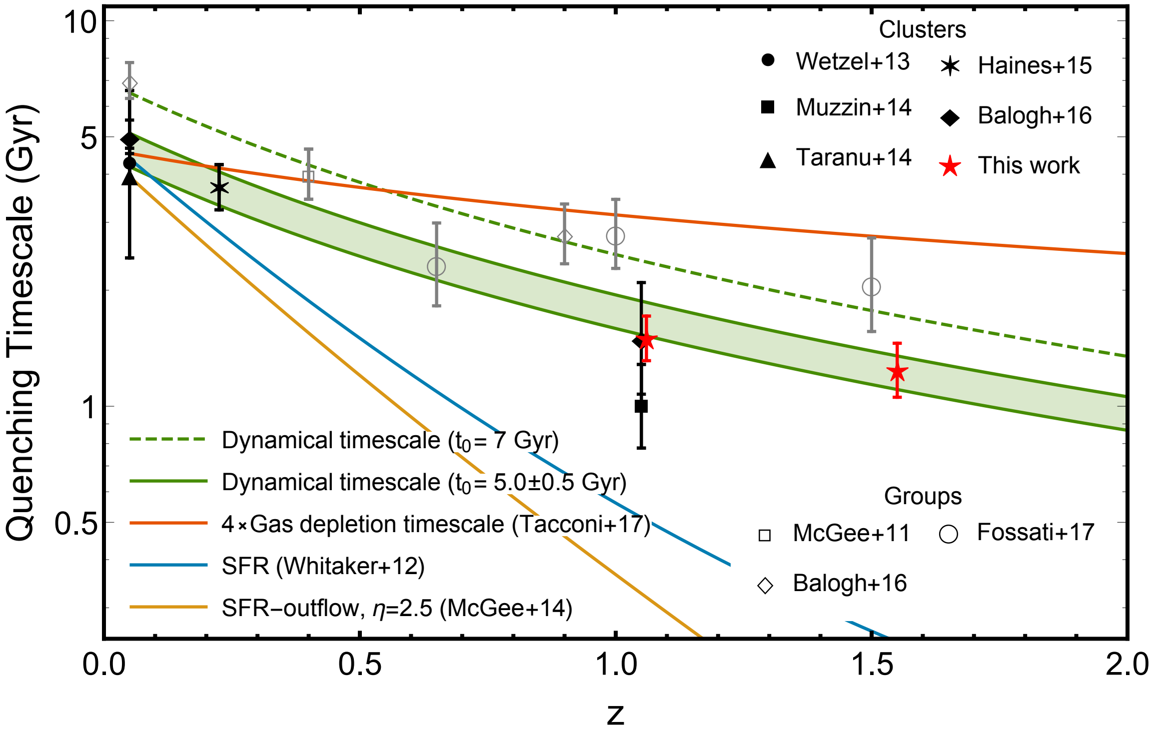

Figure 3.5 Quenching timescale as a function of redshift. Red points show the quenching timescales measured for our cluster samples at $z \sim 1$ and ~ 1.6 (see Section 3.3). Black points show the quenching timescales measured in clusters by Wetzel et al. (2013), Muzzin et al. (2014b), Taranu et al. (2014), Haines et al. (2015), and Balogh et al. (2016). Hollow gray points indicate quenching timescales measured in groups by McGee et al. (2011), Balogh et al. (2016), and Fossati et al. (2017). All data points are for galaxies with $M_* \geq 10^{10.5}$ $\mathrm{M}_\odot$. The dashed green line represents the evolution of a dynamical timescale normalized to 7 Gyr at $z = 0.05$, the quenching time in SDSS groups as reported by Balogh et al. (2016). The shaded green region represents the evolution of the dynamical timescale normalized to 5.0 ± 0.5 Gyr, spanning the range of quenching times in SDSS clusters as reported by Wetzel et al. (2013) and Balogh et al. (2016). The solid red line indicates an approximation of the total gas depletion timescale, $t_{\mathrm{depl}}(\mathrm{H_I} + \mathrm{H_{mol}})$, adapted from the molecular gas depletion timescale measured by Tacconi et al. (2017, see text). The solid blue and orange lines are estimates of the quenching time in an SFR outflow scenario. The blue line is an estimate of the gas depletion timescale with a mass loading factor of $\eta = 2.5$, described by McGee et al. (2014). The orange line shows the global evolution in star formation rates of the fundamental plane as measured by Whitaker et al. (2012), which approximates the evolution of an outflow gas depletion time, normalized to the low-redshift time of 5 Gyr.

samples and completenesses, classification systems, membership selections, and background subtractions. In the end, all models must necessarily employ various simplifying assumptions, and are approximations to a full description of galaxy quenching.

The data points described here were all measured for group or cluster galaxies in stellar mass ranges equal or comparable to our mass completeness limit, $M_* \geq 10^{10.5}$ $M_\odot$. In works where the quenching timescale was reported for separate redshift or mass bins, we take the mean quenching timescale for galaxies above our mass limit, at the mean redshift of the redshift bin. We plot cluster measurements as solid black symbols, while group measurements are plotted as hollow gray symbols.

McGee et al. (2011, 2014) studied the passive fraction in galaxy groups taken from the Group Environment Evolution Collaboration (GEEC and GEEC2, Balogh et al., 2014). McGee et al. (2014) relates the group passive fraction of $\sim$ 0.3 at $z = 0.4$ to infall histories in semi-analytic simulations (McGee et al., 2009), where 30% of galaxies became satellites more than 4.4 ± 0.6 Gyr ago. From this, it is concluded that the quenching time for these galaxies is 4.4 Gyr.

This basic approach was adapted by Wetzel et al. (2013), Balogh et al. (2016), and Fossati et al. (2017), and applied to galaxy groups and clusters in the Sloan Digital Sky Survey (SDSS, York et al., 2000), GEEC2, GCLASS, and deep-field 3D-HST/CANDELS (Grogin et al., 2011; Koekemoer et al., 2011; Brammer et al., 2012) data sets. In SDSS clusters, Wetzel et al. (2013) find a total quenching time of 4.4 ± 0.4 Gyr, where Balogh et al. (2016) finds 5.0 ± 0.5 Gyr. Balogh et al. (2016) also finds a quenching time of 7.0 ± 0.5 Gyr in SDSS groups, 2.8 ± 0.5 Gyr in GEEC2 groups, and 1.5 ± 0.5 Gyr in the

GCLASS cluster sample. Fossati et al. (2017) reports the quenching timescale for groups in the 3D-HST/CANDELS fields in three redshift bins spanning $0.5 < z < 1.80$, finding quenching times between 2 and 3 Gyr.

Muzzin et al. (2014b) employ a different method to constrain quenching timescales in the GCLASS cluster sample. Using galaxy spectral features, they identify a population of poststarburst galaxies. The distribution of this population in cluster phase space[2] can be related to the evolving phase space distribution of infalling subhalos in dark-matter zoom simulations to determine a timescale. Muzzin et al. (2014b) reports that this process indicates a rapid fade time of $t_F \simeq 0.5$ Gyr following the galaxy's first pass through 0.25-0.5 R_{200}, a passage which requires a time $t_D = 0.45 \pm 0.15$ Gyr in the simulations, for a total quenching time of $t_Q = 1.00 \pm 0.25$ Gyr.

Other studies have successfully measured quenching timescales, but use different models or assumptions that complicate direct comparison with the present work. While we define t_Q to be the time after accretion required for a galaxy to be classified quiescent, it is not uncommon to find the quenching timescale defined in other ways. In the "slow quenching" model, star-formation rates decline gradually with an exponential time constant τ_Q starting immediately upon infall. To convert from this framework to our present system of classification, we create BC03 model stellar populations with star formation rates that remain constant until infall, after which they decline with time constant τ_Q. We then plot the evolution of the model rest-frame colors and magnitudes on the classification ellipses of Figure 3.4, and take t_Q to be the time required after infall before the model is considered

---

[2] "Cluster phase space" here refers to the phase space spanned by galaxies' velocities relative to the cluster and their projected clustercentric radius.

red.

Haines et al. (2015) employ a similar phase-space approach to Muzzin et al. (2014b), comparing the radial density profiles of star-forming galaxies in clusters at $z \sim 0.2$ to the evolving radial densities of infalling halos in clusters the Millennium-II simulation, at a slightly lower mass completeness limit of 2×10^{10} $\mathrm{M}_{\odot}$. They adopt the "slow quenching" model, and find the kinematic properties of the star-forming population to be best fit by an exponentially-declining star formation rate with time constant $\tau_Q = 1.73 \pm 0.25$ Gyr. The value of t_Q corresponding to this result depends on the assumed age of the galaxy at time of infall. Cluster red-sequence galaxies at $z \lesssim 1$ have colors consistent with having been formed at $z \gtrsim 3$ (Foltz et al., 2015), and models of cluster mass-accretion rates suggest that a typical halo in a cluster at $z = 0.2$ was accreted at $z \sim 1.1$ (Fossati et al., 2017). Therefore we construct our model with an age of 3 Gyr at infall, and find that $\tau_Q = 1.73 \pm 0.25$ Gyr corresponds to $t_Q \simeq 3.7 \pm 0.5$ Gyr.

Taranu et al. (2014) employ a novel combination of observed galaxy bulge and disc colors, models of quenching star formation rates, and subhalo orbits drawn from cosmological N-body simulations. They too adopt a "slow quenching" model, and their data are best fit by an exponentially-declining star formation rate time constant of $\tau_Q =$ 3-3.5 Gyr, with quenching beginning immediately upon infall. Adopting the same conversion method as we use for Haines et al. (2015), we find this corresponds to $t_Q \simeq 4 \pm 2$ Gyr. We note that Taranu et al. (2014) use a sample of brightest cluster (and group) galaxies, an extremal population of quenched galaxies, for which our model likely breaks down.

Other notable studies preclude comparison with the present work, due to differences in mass completeness, or differences in analysis. Oman & Hudson (2016) use a phase space approach to characterize the quenching timescale in SDSS clusters. Oman & Hudson (2016) derive orbital histories for cluster and satellite galaxies from dark-matter simulations, characterizing the probability that each galaxy becomes quiescent as a function of time, $p_q(t)$. They report a typical delay time of $t_D = 3.5$-5 Gyr and a $p_q(t)$ that evolves with a time constant $\tau \lesssim 2$ Gyr. We do not attempt to interpret this in terms of a t_Q value.

Gobat et al. (2015), studying galaxies of mass $M_* \gtrsim 10^{11}$ $\mathrm{M}_\odot$ in groups in the COSMOS field at $z \sim 1.8$, find evidence for a rapid fade time of $t_F \approx 0.3$ Gyr, based on the properties of satellite galaxies. In the local universe, Schawinski et al. (2014); Paccagnella et al. (2016, 2017) conclude that quenching happens by separate rapid and slow-quenching scenarios. Paccagnella et al. (2016, 2017) find that intermediate galaxies are described by a slow-quenching scenario with a total timescale of 2-5 Gyr, although fast quenching of poststarbursts produces two times as many passive galaxies.

3.4.2 Remarks on Methods and Systematic Error

The various techniques that have been used all share two main features in common. First, they all must label a population of quenched galaxies, and/or a star-forming population. This is accomplished variously by cuts on colors and/or magnitude, inferred star formation rates, or galaxy spectral features. Second, they must relate the characteristics of the quenched or active population, or quenched fraction to timescale information. This is universally done by comparison with numerical simulations, which can relate infall times to distributions in phase space, radial surface densities, or to mass accretion histories, as in the present work.

Besides these fundamental differences in model, the next most important source of systematic error is likely the choice of how to treat the field-quenched correction (Appendix B.1 in the present work). When characterizing the quenched population of a cluster, one needs to account for the fact that the observed quenched fraction in clusters isn't entirely the result of quenching within the cluster, because quenched galaxies are found in the field as well. Therefore some number of quenched galaxies need to be subtracted from the observed count, in a manner informed by the field quenched fraction. For McGee et al. (2011), Balogh et al. (2016), and Fossati et al. (2017), this is done by calculating the quenched fraction that is in excess of the field at the observed redshift of the cluster, which is sometimes referred to as the "conversion fraction" or the "environmental quenching efficiency". The approach used by Wetzel et al. (2013) and the present work is to instead subtract off those field galaxies that were quenched at the time of accretion, not at the time of observation.

As explained in Appendix B of Balogh et al. (2016), the different approaches amount to a philosophical difference about what is being measured. By calculating the conversion fraction, one removes not only those galaxies which were quenched at the time of accretion, but also those which would have quenched in the field by the time of observation, too. The result is that the Wetzel et al. (2013) approach measures the time taken for galaxies to quench in dense environments, while the "conversion fraction" approach measures the timescale due purely to environmental quenching. Balogh et al. (2016) found t_Q to be higher by 0.5 Gyr for SDSS clusters than previous estimates by Wetzel et al. (2013), and attributes this difference to the above difference in field subtraction methods, while noting that the true answer likely lies somewhere in between. By $z \sim 1$, t_Q as measured in the GCLASS cluster sample by Balogh et al. (2016) and the present work agree within error bars.

For the present work, the field correction approach of Wetzel et al. (2013) is necessary. Our model requires a direct comparison between quenched galaxies and those which have not yet been quenched, under the assumption that these populations are the same except for the time they have spent in the cluster. In other words, the model assumes that the B, G, and R populations represent an evolutionary sequence, B $\rightarrow$ G $\rightarrow$ R. It is possible to calculate the conversion fraction of our cluster sample (see Nantais et al. 2016, 2017), arriving at the number of cluster galaxies quenched due solely to environment, but these would have to be compared to only those blue galaxies that will quench due solely to environment. It is unclear how to correct the blue population in this way without knowing the quenching timescale in advance. We therefore adopt the convention of subtracting only those galaxies that were already quenched at the time of accretion, and therefore measure the net change in galaxy properties since infall.

Of special interest within the assembled data set is a comparison between the three studies that have measured the quenching timescale in the GCLASS sample (Muzzin et al., 2014b; Balogh et al., 2016, and the present work). Specifically, at $z = 1.05$, Muzzin et al. (2014b) finds $t_Q = 1.00 \pm 0.25$ Gyr, the present work finds $1.50^{+0.19}_{-0.18}$ Gyr, and Balogh et al. (2016) finds $t_Q = 1.5 \pm 0.5$ Gyr. The results of Balogh et al. (2016) are consistent within error bars with the present work, and Muzzin et al. (2014b) very nearly so. Differences can be attributed to different approaches to measuring t_Q, including the above mentioned field corrections. The definition of quenched galaxies differs as well, where Muzzin et al. (2014b) studies quenched poststarburst galaxies identified by their spectral features, Balogh et al. (2016) uses an optical-IR color-color cut, and the present work uses a dust-corrected color-magnitude criteria. Nevertheless, these three data points point clearly to a quenching time between 1 and 1.5 Gyr.

3.4.3 Redshift Evolution of Characteristic Timescales

A clear evolutionary trend emerges from the assembled data points of Figure 3.5. The quenching timescale at low redshift is long, roughly 4-5 Gyr, but has decreased to the order of $\sim$ 1-2 Gyr at $z \sim 1.5$.

Galaxy quenching may be the result of factors internal or external to the galaxy. The former case includes scenarios where quenching occurs as a galaxy exhausts its gas reservoir (as in starvation, or overconsumption). The latter case describes scenarios where quenching is due to the interaction of a galaxy with the host halo's environment at the high speeds typical of orbits within clusters. In this section, we will endeavor to model several timescales associated with either gas depletion or kinematic effects, and plot them on Figure 3.5.

In gas depletion scenarios, the environment simply prevents cosmological accretion of fresh gas onto the galaxy, and what gas reservoir remains after infall is consumed by the galaxy over a gas depletion timescale $t_{\mathrm{depl}} = M_{gas}/\dot{M_{gas}}$, after which star formation ceases. Fillingham et al. (2015) note that measured molecular gas depletion timescales $t_{\mathrm{depl}}(\mathrm{H}_{\mathrm{mol}})$ are much shorter than measured values of t_Q, over a broad range of redshifts. This trend continues to be seen with the quenching timescales measured since the time of that study, including those in the present work. In the local universe, however, Fillingham et al. (2015) find very good agreement between the total gas depletion timescale $t_{\mathrm{depl}}(\mathrm{H}_{\mathrm{I}} + \mathrm{H}_{\mathrm{mol}})$ and the quenching times of high-mass galaxies ($M_* \geq 10^9$ M$_\odot$). The first hypothesis we will consider is that the quenching timescale is simply the total gas depletion timescale, where the galaxy's star-forming gas reservoir includes the atomic gas component.

A star-forming galaxy's molecular gas fraction is found to decrease slowly with redshift out to $z = 2$, by roughly a factor of 2 (Genzel et al., 2015; Tacconi et al., 2017), while the atomic gas density remains nearly constant (Bauermeister et al., 2010). Since in the local universe, $M_{HI} \sim 3M_{mol}$ (see, e.g., Saintonge et al., 2011), for simplicty we will take $t_{\rm depl}(\rm H_I+H_{mol}) \sim\ 4\ t_{\rm depl}(\rm H_{mol})$, with the redshift evolution of $t_{\rm depl}(\rm H_{mol})$ from Tacconi et al. (2017), and plot it on Figure 3.5.

If galaxies experience significant star-formation-driven outflows, then the gas depletion timescale will be much shorter. McGee et al. (2014) has constructed a model parametrized by the "mass-loading factor" η, such that the rate of gas mass ejected by a galaxy is a factor η of the star formation rate. We include on Figure 3.5 the gas depletion time with outflows of $\eta = 2.5$, using the cosmic evolution of the star formation rate derived by Whitaker et al. (2012). This value of η was found to best fit the quenching timescales described by McGee et al. (2014), and produces timescales that match t_Q in clusters at low redshift. While McGee et al. (2014) intend for this timescale to model the delay time rather than the full quenching time, we include it on Figure 3.5 to indicate its evolution with redshift. It is broadly the case that outflow timescales for various values of η scale with redshift approximately as SFR, and so we also include on Figure 3.5 the SFR evolution of Whitaker et al. (2012), normalized to a low-redshift timescale of 5 Gyr.

The dynamical time $t_{\rm dyn}$ is commonly used to characterize timescales that depend on the kinematics of a galaxy within a cluster, such as gas stripping scenarios. A cluster halo in virial equilibrium is characterized by relations between its radius R and the velocity V of its constituent galaxies, defining a dynamical timescale, $t_{\rm dyn} = R/V$. From considerations of cosmology, the dynamical time is expected to scale with redshift as $t_{\rm dyn} \propto (1+z)^{-1.5}$. If quenching is accomplished after a galaxy makes one or multiple passes through a particular radius of its host halo, t_Q will be proportional to $t_{\rm dyn}$. We normalize the dynamical timescale at low redshift separately to the SDSS group and cluster t_Q data points. We choose a normalization of 5.0 ± 0.5 Gyr for the cluster dynamical time scale, to span the two values for this data set reported by Wetzel et al. (2013) and Balogh et al. (2016). We normalize the group dynamical time scale to the 7 Gyr t_Q reported by Balogh et al. (2016). We plot these dynamical timescales also on Figure 3.5.

These trend lines roughly depict the expected evolution of t_Q for various possible quenching scenarios. They assume that the dominant quenching mechanism remains unchanged from low redshift, and is invariant for a given star formation rate and stellar mass. We don't intend for these timescales to conclusively identify the mechanism responsible for environmental quenching, but rather to test if the measured redshift evolution of t_Q is consistent with these possible models.

3.4.4 Interpreting the Quenching Timescale

The quenching timescale of massive galaxies ($M_* \geq 10^{10.5}$ M$_\odot$) is systematically higher in groups than in clusters. In the SDSS sample, this trend is particularly pronounced, with t_Q being higher in groups by ~ 2 Gyr (Balogh et al., 2016), although a difference is seen at all measured redshifts. This difference cannot be entirely attributed to differences in background subtraction, as demonstrated by the agreement between the present work and Balogh et al. (2016) for the GCLASS cluster sample. If t_Q truly exhibits a dependence upon the mass of the host halo, then the quenching timescale is driven in part by factors external to the galaxy.

The total gas depletion timescale $t_{\mathrm{depl}}(\mathrm{H_I} + \mathrm{H_{mol}})$ is a good fit for galaxies at low redshift, but seemingly evolves too slowly to be a good fit at higher redshift. On the other hand, both estimates of an SFR-outflow timescale evolve too quickly at high redshift. It is possible that gas is simply consumed more quickly by high-mass galaxies at high redshift, as in an overconsumption scenario, although models with fixed mass-loading factor η cannot simultaneously fit both the high- and low-redshift data points. However, the cluster data points and group data points both evolve in accordance with the appropriately-normalized dynamical timescale.

The evolution of the dynamical time represents an evolution in the properties of groups and clusters (velocity dispersions, halo masses, etc.), not galaxy properties (SFR, gas fractions, etc.). If quenching tracks t_{dyn}, then it must be determined by the dynamical properties of clusters . Such a scenario is often interpreted as being evidential of dynamical quenching scenarios such as ram-pressure stripping.

Balogh et al. (2016) find that SFR-outflow quenching is a good fit to the delay times measured in the GCLASS and GEEC2 samples at $z \sim 1$. This conclusion is based in part on the quenching timescales measured in galaxies with masses $M_* \leq 10^{10.3}$ $\mathrm{M_\odot}$, which we do not study here. For those galaxies, t_Q is found to be longer by several Gyr, and to increase with decreasing galaxy mass, in a way that is well-modeled by SFR outflows with

$1.0 \leq \eta \leq 2.0$, although the same model is a poor fit at low redshift. Balogh et al. (2016) report that the dynamical timescale is a good fit to t_Q in galaxies with $M_* \geq 10^{10.5}$ $\mathrm{M}_\odot$, as also noted by others (Tinker & Wetzel, 2010; Mok et al., 2014). No disagreement is found between the present work and Balogh et al. (2016) for the samples and analyses where these studies overlap.

In the local universe, Fillingham et al. (2015) find that t_Q in galaxies with masses $M_* \geq 10^{10.5}$ $\mathrm{M}_\odot$ is well-fit by the total gas depletion timescale, $t_{\mathrm{depl}}(\mathrm{H_I} + \mathrm{H_{mol}})$. Using a different estimate of $t_{\mathrm{depl}}(\mathrm{H_I} + \mathrm{H_{mol}})$ based on $t_{\mathrm{depl}}(\mathrm{H_{mol}})$ (Tacconi et al., 2017), we arrive at the same conclusion. However, the gas depletion timescale does not evolve quickly enough to reach times on the order of 1-2 Gyr at $z \sim 1.5$. The timescale we compare with here is a very rough extrapolation, as there are very few constraints on galaxy atomic gas budgets at $z \gtrsim 0.1$ (see discussion in Bauermeister et al., 2010). Future work may better characterize the evolution of the total gas depletion timescale.

3.5 Conclusions

In this chapter we measured numbers of star-forming, intermediate, and quenched cluster members in two samples of galaxy clusters at $0.85 < z < 1.35$ and $1.35 < z < 1.65$. A model of environmental quenching allows these number counts to constrain the quenching timescale t_Q. From the analysis presented in this work, we draw the following conclusions:

- We measure a quenching timescale of $t_Q = 1.50^{+0.19}_{-0.18}$ Gyr in a sample of 10 galaxy clusters at $0.85 < z < 1.35$, while in a sample of 4 galaxy clusters at $1.35 < z < 1.65$ we find the quenching timescale to be $t_Q = 1.24^{+0.23}_{-0.20}$ Gyr.

- The evolution of the quenching timescale in clusters from the local universe to $z = 1.55$ evolves faster than the gas depletion timescale but slower than an SFR outflow model. Instead, it appears to scale with the dynamical time, when normalized to the quenching timescale in local galaxy clusters. This suggests that kinematical quenching mechanisms such as ram-pressure stripping may dominate in galaxies with masses $M_* \geq 10^{10.5}$ M$_\odot$ in clusters at high redshift.

- The quenching timescale for galaxies with masses $M_* \geq 10^{10.5}$ M$_\odot$, measured out to $z \sim 1.55$, appears to be shorter in clusters than in groups. This indicates that environmental quenching mechanisms for these galaxies may depend on host halo mass at high redshift, as would be the case for kinematical quenching mechanisms such as ram-pressure stripping.

Chapter 4

Summary

In this work we have presented two studies of galaxy populations in cluster samples at $z \sim 1$ and $z \sim 1.5$ with the aim of constraining galaxy formation and evolutionary processes. In Chapter 2 we studied the red-sequence in a sample of ten galaxy clusters at $z \sim 1$. In Chapter 3 we modeled the quenching process for the same sample of clusters as well as a sample of four clusters at $z \sim 1.5$.

4.1 The Color-Magnitude Relation at $z \sim 1$

The linear form of the color-magnitude relation can be modeled by a metallicity sequence of simple stellar populations formed at high redshift, normalized to reproduce the CMR in the local universe. The evolution of this model CMR allows for a physical interpretation of its slope, scatter, and intercept. Starting from these considerations, we study the CMR in the GCLASS sample of ten red-sequence-selected clusters at $z \sim 1$. Extensive spectroscopy, combined with interpolated rest-frame colors, allows for a precise determination of the CMR in these clusters.

The CMR zeropoint does not evolve with redshift to $z = 1.3$. From comparison with models, this indicates that the quiescent population in these clusters is mature, and formed the bulk of its stars at $z_f \geq 3$. Interpretation of the CMR intrinsic scatter is more complicated, as it may be the result of several factors, including variation in galaxy ages and metallicities. If we assume the intrinsic scatter is due solely to a scatter in ages, then it can constrain the spread in ages for these galaxies. For galaxies with $z_f = 3$, we find the scale of the intrinsic scatter is consistent with an average age spread of $\Delta t \geq 1$ Gyr.

We compare our results with an X-ray-selected sample of clusters at a similar redshift. X-ray- or red-sequence-selected clusters are known to be inherently biased toward either gas-rich systems or galaxy-rich systems. However, within uncertainties, we find no difference in the red-sequence slope, scatter, or intercept between the two cluster samples. The quiescent galaxy populations within these cluster samples are insensitive to any cluster biases that may be present.

We compare the quiescent galaxy populations identified by spectroscopic features versus rest-frame UVJ color-color selection. 14% of the UVJ-quiescent population show [OII] emission, while 16% of the UVJ-star-forming galaxies exhibit no [OII] emission.

4.2 Evolution in Quenching Time from $z = 0$ to $z = 1.5$

We present a toy model of environmental quenching that describes the build-up of the quenched and star-forming galaxy populations in terms of a cluster mass accretion rate and a quenching time t_Q. In this model, star-forming galaxies that are accreted by the cluster remain star-forming for a delay time, t_D, after which their star formation rate decreases to zero over a fade time, t_F. With cluster halo mass accretion rates taken from the Millennium-II simulation, the numbers of observed star-forming, intermediate, and quenched galaxies can constrain the fade and delay times, and thereby the total quench time. We apply this modeling to intermediate-mass galaxies ($M_* \geq 10^{10.5}$ $\mathrm{M}_\odot$) in the $z \sim 1$ and $z \sim 1.5$ cluster samples, finding a t_Q of ~ 1.5 Gyr and ~ 1.2 Gyr, respectively.

Assembling measurements of t_Q found in the literature, we find that the quenching time has decreased significantly with redshift. While in the local universe t_Q is roughly 4-5 Gyr, it has decreased to the order of $\sim$ 1-2 Gyr at $z \sim 1.5$. We compare the redshift behavior of t_Q with the modeled time evolution of the total gas depletion time, global star-formation rates, an SFR-outflow model, and the dynamical (crossing) time, t_{dyn}. The quenching time is seen to evolve faster than the gas depletion timescale and slower than the SFR-outflow timescale, but is consistent with the evolution of the dynamical time. Additionally, t_Q exhibits dependence on the mass of the host halo: at low redshift, t_Q is longer by ~ 2 Gyr in groups than in clusters, and the group quenching time remains longer than the cluster quenching time at all redshifts probed.

Care must be taken when interpreting this result. The dynamical time is a function of the global properties of the host cluster (velocity dispersions, halo masses), not the properties of the galaxy (star formation rate, gas fraction, stellar mass). That t_Q evolves like t_{dyn}, and that it depends on host halo mass both suggest that the quenching time of these galaxies is driven by the dynamical properties of their host halos. This is expected for quenching mechanisms that rely on the galaxy making one or more passes through a certain radius of the host cluster halo, such as ram-pressure or tidal stripping scenarios. However, it is also possible that environment affects the efficiency of mass-driven quenching mechanisms, as has been suggested by Henriques et al. (2017). We caution that it may be the case that the relevant physics do not separate cleanly into environmental and intrinsic mechanisms, but instead result from an interplay between the properties of a galaxy and its host halo.

4.3 Future Work

The major results of Chapter 3 depend on comparisons drawn between values of t_Q reported in the literature. The various studies included on Figure 3.5 generally differ in their datasets, their definitions of star-forming and quenched galaxies, and their methods of associating timescales with the properties of galaxy populations. A stronger result would be obtained if our quenching-time model could be applied to a single, homogeneously-selected sample of clusters and galaxies spanning $0 < z < 1.6$. Stacking results over a larger cluster sample also serves to reduce uncertainty due to cosmic variance and differences in cluster accretion histories.

The t_Q model as presented assumes a fixed value for t_Q. This means that the value measured for t_Q is time-averaged over the past history of the cluster, weighted by the mass accretion rate. As the quenching time is short and evolves slowly over $1.0 < z < 1.6$, while the mass accretion rate increases with time, this assumption does not greatly influence our results. Because most of the mass of a cluster has been accreted in its recent past, the time-averaged t_Q is closer to the instantaneous value. This effect is not present in the studies assembled on Figure 3.5 that measure t_Q from the properties of the star-forming population, or from a short-lived quenched population, and the overall dynamical evolutionary trend of t_Q should therefore not be affected by this consideration. Nevertheless, it should be possible to modify the RGB model to account for a time-varying $t_Q(z)$. This modification would be necessary when applying the model to lower-redshift clusters where a history of variation in $t_Q(z)$ has a much larger effect on the quenched fraction.

The results of Chapter 3 suggest that ram-pressure or tidal stripping should not be discounted as possible quenching mechanisms. Models of stripping that take into account galaxy mass, orbit, structural parameters, and stripping rate have been shown to provide much better fits to observed galaxy properties than early, crude models which assumed instantaneous stripping (McCarthy et al., 2008; Font et al., 2008b; Henriques et al., 2017). It is possible that more development in this area could improve the results of future semi-analytic models.

Appendix A

Star Formation Histories

The eSFH models employ a star formation history parametrized by:

$$\Psi(t, \tau) = \mathrm{SFR}_0 \cdot e^{-t/\tau} \left[\frac{M_\odot}{\mathrm{yr}}\right], \tag{A.1}$$

where Ψ is the instantaneous star formation rate at time t after the onset of star formation, SFR_0 is the initial star formation rate, and τ is a parameter ranging from 0.5 Gyr $\leq \tau \leq$ 5 Gyr.

We begin by generating model stellar populations with the range of six metallicities provided by the BC03 population synthesis code (Z = 0.0001, 0.0004, 0.004, 0.008, 0.02 ($Z_\odot$), 0.05). These six models each exhibit a metallicity-dependent U-V, J-K, and V-K color, but the absolute $M_{B,z=0}$ magnitudes are free parameters of these stellar population models. We therefore fix each $M_{B,z=0}$ magnitude by finding the value for which the reported Coma CMRs (Bower et al., 1992) best match each model's U-V, J-K, and V-K colors, by minimizing χ^2. This essentially provides mass normalizations for each galaxy model and reproduces the CMR at $z = 0$. The galaxy models then describe a simple red-sequence which may be passively evolved backward in redshift to provide a predicted redshift evolution of CMR slope and zeropoint.

There is remarkably good agreement between the slope of the modeled red-sequence and those which we report for the GCLASS sample in Table A.2. The modeled slope does not evolve significantly or disagree with our measured slope between $0.8 < z < 1.3$, for any chosen formation redshift or star formation history, and therefore does not constrain our models.

The competing influences of age and ongoing star formation on the zeropoint color introduce a sort of degeneracy which means we cannot distinguish between young galaxies that very quickly shut off star formation and old galaxies with more recent star formation. Therefore we combine both factors into a single parameter which can be constrained by observation: the star formation weighted age, $\langle t \rangle_{\mathrm{SFH}}$, which gives the average age of the bulk of the stars, following Rettura et al. (2011):

$$\langle t \rangle_{\mathrm{SFH}} \equiv \frac{\int_0^t (t - t')\Psi(t', \tau)\mathrm{d}t'}{\int_0^t \Psi(t', \tau)\mathrm{d}t'} \tag{A.2}$$

For the star formation history defined in Equation A.1, this equals

$$\langle t \rangle_{\mathrm{SFH}} = \frac{t - \tau + \tau \cdot e^{-t/\tau}}{1 - e^{-t/\tau}}. \tag{A.3}$$

Our observed zeropoints can then place constraints on this $\langle t \rangle_{\mathrm{SFH}}$, which, together with the lookback time to the redshift of the cluster, can constrain the star-formation-weighted formation redshift $\langle z_f \rangle_{\rm SFH}$ of these stellar populations. We note that in general, the formation of the stars will be followed by their assembly into galaxies, and the age of the galaxy will be younger than the age of its component stars.

Table A.1. Description of the GCLASS cluster sample

Index	Cluster	R.A.	Decl.	z	Members[a]	R_{200}[b] (h^{-1} Mpc)	Mass ($10^{14}M_\odot$)
1	SpARCS J003442-430752	00:34:42.086	-43:07:53.360	0.866	34	$0.93^{+0.10}_{-0.18}$	$2.4^{+0.9}_{-1.2}$
2	SpARCS J003645-441050	00:36:45.039	-44:10:49.911	0.869	48	$1.1^{+0.1}_{-0.2}$	$4.4^{+1.7}_{-1.6}$
3	SpARCS J161314+564930	16:13:14.641	56:49:29.504	0.871	89	$1.8^{+0.1}_{-0.2}$	$17.6^{+4.6}_{-4.2}$
4	SpARCS J104737+574137	10:47:37.463	57:41:37.960	0.956	30	$0.76^{+0.09}_{-0.10}$	$1.5^{+0.6}_{-0.5}$
5	SpARCS J021524-034331	02:15:23.200	-03:43:34.482	1.004	46	$0.55^{+0.07}_{-0.10}$	$0.59^{+0.27}_{-0.26}$
6	SpARCS J105111+581803	10:51:11.232	58:18:03.128	1.035	32	$0.61^{+0.10}_{-0.13}$	$0.85^{+0.46}_{-0.44}$
7	SpARCS J161641+554513	16:16:41.232	55:45:25.708	1.156	45	$0.74^{+0.09}_{-0.12}$	$1.7^{+0.7}_{-0.7}$
8	SpARCS J163435+402151	16:34:35.402	40:21:51.588	1.177	46	$0.89^{+0.11}_{-0.12}$	$3.1^{+1.3}_{-1.1}$
9	SpARCS J163852+403843	16:38:51.625	40:38:42.893	1.196	39	$0.56^{+0.06}_{-0.12}$	$0.77^{+0.31}_{-0.40}$
10	SpARCS J003550-431224	00:35:49.700	-43:12:24.160	1.335	23	$1.0^{+0.2}_{-0.2}$	$5.5^{+3.0}_{-3.2}$

[a] Number of spectroscopically-confirmed member galaxies.

[b] The radius for which the mean density is 200 times the critical density. From Wilson et al. (2015, in prep).

Table A.2. Color-magnitude relation fit parameters

Index	Cluster	N[a]	Method[b]	$\frac{\Delta(U-B)_{z=0}}{\Delta M_{B,z=0}}$[c]	$\sigma(U-B)_{z=0}$[d]	c_0(AB)[e]	c_0(Vega)
1	J003442-430752	14	MLE	$-0.041^{+0.043}_{-0.044}$	$0.067^{+0.024}_{-0.017}$	$1.211^{+0.026}_{-0.023}$	$0.3720^{+0.026}_{-0.023}$
			TLS	$-0.046^{+0.030}_{-0.061}$	$0.057^{+0.017}_{-0.018}$	$1.189^{+0.043}_{-0.006}$	$0.3490^{+0.043}_{-0.006}$
2	J003645-441050	22	MLE	$-0.003^{+0.041}_{-0.042}$	$0.123^{+0.028}_{-0.022}$	$1.239^{+0.031}_{-0.028}$	$0.4020^{+0.031}_{-0.028}$
			TLS	$-0.016^{+0.057}_{-0.038}$	$0.094^{+0.018}_{-0.024}$	$1.214^{+0.050}_{-0.040}$	$0.3760^{+0.050}_{-0.040}$
3	J161314+564930	54	MLE	$-0.008^{+0.023}_{-0.024}$	$0.123^{+0.015}_{-0.013}$	$1.194^{+0.025}_{-0.023}$	$0.3570^{+0.025}_{-0.023}$
			TLS	$-0.024^{+0.028}_{-0.015}$	$0.069^{+0.018}_{-0.021}$	$1.191^{+0.018}_{-0.029}$	$0.3530^{+0.018}_{-0.029}$
4	J104737+574137	14	MLE	$-0.034^{+0.074}_{-0.077}$	$0.112^{+0.036}_{-0.025}$	$1.226^{+0.041}_{-0.042}$	$0.3870^{+0.041}_{-0.042}$
			TLS	$-0.082^{+0.041}_{-0.045}$	$0.065^{+0.011}_{-0.040}$	$1.223^{+0.018}_{-0.039}$	$0.3810^{+0.018}_{-0.039}$
5	J021524-034331	24	MLE	$-0.033^{+0.043}_{-0.044}$	$0.102^{+0.025}_{-0.020}$	$1.284^{+0.028}_{-0.026}$	$0.4450^{+0.028}_{-0.026}$
			TLS	$-0.057^{+0.033}_{-0.038}$	$0.046^{+0.034}_{-0.008}$	$1.269^{+0.031}_{-0.032}$	$0.4290^{+0.031}_{-0.032}$
6	J105111+581803	16	MLE	$-0.013^{+0.044}_{-0.041}$	$0.089^{+0.032}_{-0.024}$	$1.220^{+0.032}_{-0.033}$	$0.3820^{+0.032}_{-0.033}$
			TLS	$-0.018^{+0.043}_{-0.051}$	$0.065^{+0.008}_{-0.038}$	$1.216^{+0.033}_{-0.035}$	$0.3780^{+0.033}_{-0.035}$
7	J161641+554513	25	MLE	$-0.009^{+0.017}_{-0.018}$	$0.046^{+0.012}_{-0.011}$	$1.222^{+0.015}_{-0.014}$	$0.3840^{+0.015}_{-0.014}$
			TLS	$-0.014^{+0.014}_{-0.013}$	$0.030^{+0.010}_{-0.008}$	$1.215^{+0.016}_{-0.015}$	$0.3770^{+0.016}_{-0.015}$
8	J163435+402151	17	MLE	$-0.038^{+0.044}_{-0.044}$	$0.051^{+0.018}_{-0.013}$	$1.229^{+0.014}_{-0.015}$	$0.3900^{+0.014}_{-0.015}$
			TLS	$-0.035^{+0.027}_{-0.039}$	$0.030^{+0.010}_{-0.011}$	$1.226^{+0.017}_{-0.010}$	$0.3870^{+0.017}_{-0.010}$
9	J163852+403843	7	MLE	$-0.064^{+0.088}_{-0.100}$	$0.061^{+0.046}_{-0.023}$	$1.200^{+0.032}_{-0.031}$	$0.3590^{+0.032}_{-0.031}$
			TLS	$-0.040^{+0.034}_{-0.140}$	$0.028^{+0.001}_{-0.023}$	$1.200^{+0.010}_{-0.012}$	$0.3610^{+0.010}_{-0.012}$
10	J003550-431224	11	MLE	$-0.030^{+0.068}_{-0.068}$	$0.094^{+0.044}_{-0.032}$	$1.242^{+0.042}_{-0.040}$	$0.4030^{+0.042}_{-0.040}$
			TLS	$-0.041^{+0.057}_{-0.030}$	$0.047^{+0.014}_{-0.022}$	$1.233^{+0.036}_{-0.034}$	$0.3940^{+0.036}_{-0.034}$

[a] The number of quiescent cluster member galaxies used in computing the fit.

[b] The method used to derive fit parameters: maximum likelihood estimator (MLE) or total least squares (TLS).

[c] The slope of the rest-frame U-B color-magnitude relation.

[d] The intrinsic scatter of the rest-frame U-B color-magnitude relation.

[e] The zeropoint, i.e., the U-B color of the color-magnitude relation evaluated at M_B=-21.4, reported as an AB magnitude.

Table A.3. Color-mass relation fit parameters

Index	Cluster	N[a]	$\frac{\Delta(U-B)_{z=0}}{\Delta log(M_*/M_\odot)}$[b]	$\sigma(U-B)_{z=0}$[c]	c_0[d]
1	SpARCS J003442-430752	18	$0.043^{+0.166}_{-0.136}$	$0.033^{+0.024}_{-0.015}$	$1.211^{+0.020}_{-0.017}$
2	SpARCS J003645-441050	28	$0.173^{+0.405}_{-0.408}$	$0.088^{+0.034}_{-0.026}$	$1.267^{+0.095}_{-0.137}$
3	SpARCS J161314+564930	44	$0.086^{+0.085}_{-0.083}$	$0.127^{+0.017}_{-0.014}$	$1.209^{+0.024}_{-0.026}$
4	SpARCS J104737+574137	15	$0.079^{+0.235}_{-0.305}$	$0.083^{+0.042}_{-0.030}$	$1.252^{+0.050}_{-0.051}$
5	SpARCS J021524-034331	30	$0.048^{+0.168}_{-0.199}$	$0.048^{+0.026}_{-0.022}$	$1.298^{+0.022}_{-0.021}$
6	SpARCS J105111+581803	14	$0.234^{+0.130}_{-0.118}$	$0.058^{+0.026}_{-0.020}$	$1.271^{+0.035}_{-0.033}$
7	SpARCS J161641+554513	29	$0.048^{+0.065}_{-0.071}$	$0.033^{+0.014}_{-0.012}$	$1.225^{+0.018}_{-0.017}$
8	SpARCS J163435+402151	17	$0.338^{+0.182}_{-0.140}$	$0.030^{+0.019}_{-0.014}$	$1.263^{+0.033}_{-0.027}$
9	SpARCS J163852+403843	7	$0.314^{+0.226}_{-0.255}$	$0.085^{+0.054}_{-0.032}$	$1.217^{+0.053}_{-0.056}$
10	SpARCS J003550-431224	11	$0.181^{+0.139}_{-0.128}$	$0.076^{+0.040}_{-0.029}$	$1.240^{+0.032}_{-0.031}$

Note. — These fit parameters were derived using a Bayesian maximum likelihood estimator.

[a] The number of quiescent cluster member galaxies used in computing the fit.

[b] The slope of the rest-frame U-B color-mass relation.

[c] The intrinsic scatter of the rest-frame U-B color-mass relation.

[d] The zeropoint of the rest-frame U-B color-mass relation, in AB magnitudes.

Appendix B

Environmental Quenching Model

In this model, environmental quenching is characterized by a quenching timescale t_Q, defined as the length of time after accretion for a galaxy to be completely quenched. A galaxy's time in the cluster is divided into three evolutionary phases: a (blue) delay phase, wherein star formation continues as if unaffected by environment, a (green) fade phase, during which star formation declines, and a (red) quenched phase, after star formation has fully ceased. The observed colors of galaxies trace their star formation rate and therefore the galaxy's evolutionary phase (see Figure 3.4), and form the basis for labeling the delay, fade, and quenched phases as blue, green, and red, respectively.

We take as given the observed numbers of red, green, and blue galaxies in a given cluster (R, G, and B, respectively), at the redshift of the cluster, z_c. For our purposes, it is first necessary to correct for galaxies that were already quenched before they fell into the cluster. We calculate the total fraction of quiescent galaxies accreted from the field over the lifetime of the cluster using the field galaxy mass functions computed by Muzzin et al.

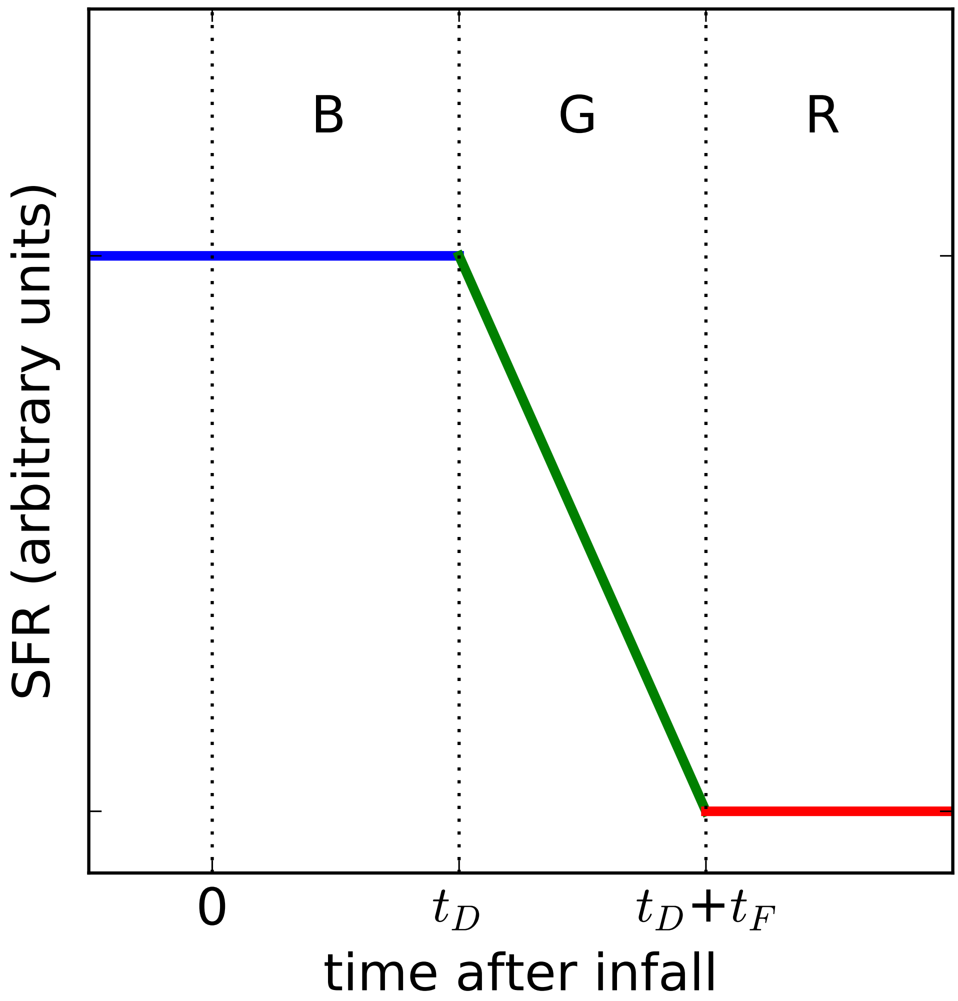

Figure B.1 Model star formation rate of a galaxy as a function of time relative to its accretion by the cluster. The galaxy's color reflects its star formation rate, such that star-forming galaxies are labeled blue, galaxies with declining star formation rate are labeled green, and quiescent galaxies are labeled red. All galaxies that fall into the cluster are assumed to be star-forming, and remain star-forming for a delay time t_D. Following the delay period, star formation begins to quench over a fade time, t_F, after which the galaxy is quiescent. The total quenching time t_Q is $t_D + t_F$.

(2013c). We then subtract this fraction from the observed number of red galaxies, leaving only galaxies that were blue when accreted by the cluster. This field-quenched correction is described in detail in B.1. For the rest of this discussion, we assume corrected number counts of galaxies, and that these galaxies were star-forming when accreted.

A (blue) star-forming galaxy that falls into the cluster will remain star-forming for a delay time, t_D. After the passage of one delay time t_D, the galaxy's star formation rate fades over the fade time, t_F. Subsequent to a total amount of time $t_Q = t_D + t_F$, a galaxy has completely ceased forming stars, and is considered quiescent. In Figure B.1, we show this evolution of galaxy type schematically as a function of time following infall.

From this, it follows that star-forming (blue) cluster members were accreted as recently as up to one t_D ago, and so are still in their star-forming "delay" phase. Intermediate (green) cluster members, in the "fade" phase, were accreted between t_D and $t_D + t_F$ ago. Quenched (red) cluster members are all galaxies accreted earlier than that. The quenching time t_Q is then the sum of the delay time, t_D, and a fade time, t_F.

The central assumption of this model is that all galaxies undergo the same evolutionary process, passing from blue to green to red once accreted by the cluster. Because of this, the numbers of blue and green galaxies found in the cluster trace the amount of time spent in the delay and fade phases of evolution, and red galaxies trace the integrated history of all galaxy accretion older than one quenching time.

Given a galaxy accretion rate $\mathrm{d}N/\mathrm{d}t$, the numbers of red, green, and blue galaxies can constrain the times t_D and t_F. Specifically,

$$
\begin{aligned}
B &= \int_{-t_D}^{0} \mathrm{d}N/\mathrm{d}t\ \mathrm{d}t \\
G &= \int_{-(t_D+t_F)}^{-t_D} \mathrm{d}N/\mathrm{d}t\ \mathrm{d}t \\
R &= \int_{-t_H}^{-(t_D+t_F)} \mathrm{d}N/\mathrm{d}t\ \mathrm{d}t
\end{aligned}
$$

where B, G, and R are the numbers of blue, green, and red cluster galaxies, respectively, observed at time $t = 0$, and t_H is the Hubble time. Note that the negative sign of the integration limits emphasizes the fact that these galaxies were accreted in the past. While we have begun by stating functions here in terms of time t relative to the cluster, later we will cast our equations in terms of redshift for easier use with real data.

In principle, the galaxy accretion rate $\mathrm{d}N/\mathrm{d}t$ is some fraction of the total halo mass accretion rate $\mathrm{d}M/\mathrm{d}t$, determined by the baryon and gas fractions of galaxies, and related to observed counts by the stellar mass function above the mass completeness of our sample. However, it is not necessary to calculate this factor if we consider ratios of galaxy counts instead of absolute numbers. Given that galaxy stellar mass is some fraction of the mass accreted by the cluster, such that $\mathrm{d}N/\mathrm{d}t = f_G\ \mathrm{d}M/\mathrm{d}t$, it follows that

$$
\frac{\int_{t_2}^{t_1} \mathrm{d}N/dt\ \mathrm{d}t}{\int_{t_3}^{t_2} \mathrm{d}N/\mathrm{d}t\ dt} = \frac{\int_{t_2}^{t_1} f_G\ \mathrm{d}M/\mathrm{d}t\ \mathrm{d}t}{\int_{t_3}^{t_2} f_G\ \mathrm{d}M/\mathrm{d}t\ \mathrm{d}t}
$$

for arbitrary times t_1, t_2, t_3. If we assume f_G remains relatively constant with time, we can cancel it from the right-hand side of the above equation, and can therefore express ratios of galaxy counts purely in terms of the mass accretion rate, $\mathrm{d}M/\mathrm{d}t$.

Cosmological N-body simulations can make predictions for the mass accretion histories of cluster-scale dark matter halos (Lacey & Cole, 1993). Fakhouri et al. (2010) has used merger histories in the Millennium-II simulation to fit an expression for the mean mass growth rate of halos of the form

$$\frac{\mathrm{d}M}{\mathrm{d}t} = 46.1\ \mathrm{M}_\odot\ \mathrm{yr}^{-1} \left(\frac{M}{10^{12}\ \mathrm{M}_\odot}\right)^{1.1} \times (1 + 1.11z)\sqrt{\Omega_\mathrm{m}(1+z)^3 + \Omega_\Lambda}$$

for a halo of mass M at redshift z.

A change of units yields

$$\begin{aligned} \frac{\mathrm{d}M}{\mathrm{d}z} &= \frac{-t_H}{46.1\ \mathrm{yr}} \times \left(\frac{1+1.11z}{1+z}\right)\left(\frac{M}{10^{12}\ \mathrm{M}_\odot}\right)^{1.1} \mathrm{M}_\odot \\ M(z = 1.6) &= 3 \times 10^{14}\ \mathrm{M}_\odot \end{aligned}$$

where we have used the mean cluster mass of the $z = 1.6$ cluster sample as a boundary condition. When calculating quenching timescales for the lower-redshift cluster sample, the mean cluster mass boundary condition is $M = 3.8 \times 10^{14}\ \mathrm{M}_\odot$ at $z = 1$. We note that our $z = 1.6$ cluster sample has a mean halo mass that is only slightly higher than that of progenitors of the $z = 1$ sample (Lidman et al., 2012b; Nantais et al., 2017), and our results do not depend strongly on the choice of host halo mass for a reasonable range of masses.

This system of equations can be solved numerically for $M(z)$, the total cluster mass as a function of redshift, and $\mathrm{d}M/\mathrm{d}z$, the mass accretion rate. By recasting our earlier set of equations to be functions of redshift, we can now write

$$\frac{B}{G+R} = \frac{\displaystyle\int_{z_c+\Delta z_D}^{z_c} \mathrm{d}M/\mathrm{d}z\ \mathrm{d}z}{\displaystyle\int_{\infty}^{z_c+\Delta z_D} \mathrm{d}M/\mathrm{d}z\ \mathrm{d}z}$$

$$\frac{G}{R} = \frac{\displaystyle\int_{z_c+\Delta z_D+\Delta z_F}^{z_c+\Delta z_D} \mathrm{d}M/\mathrm{d}z\ \mathrm{d}z}{\displaystyle\int_{\infty}^{z_c+\Delta z_D+\Delta z_F} \mathrm{d}M/\mathrm{d}z\ \mathrm{d}z}$$

where, for a cluster at $z = z_c$, $z_c + \Delta z_D$ is the redshift one delay time t_D ago, and $z_c + \Delta z_D + \Delta z_F$ is one delay plus fade time, $t_D + t_F$, ago. The relationship between these variables is summarized visually in Figure B.2.

With an expression for $M(z)$, the integral relations become

$$\frac{B}{G+R} = \frac{M(z_c) - M(z_c + \Delta z_D)}{M(z_c + \Delta z_D)}$$

$$\frac{G}{R} = \frac{M(z_c + \Delta z_D) - M(z_c + \Delta z_D + \Delta z_F)}{M(z_c + \Delta z_D + \Delta z_F)}$$

where we have used the fact that $M(z) = 0$ when $z \to \infty$.

Altogether we apply the following set of three equations with three unknowns, and one boundary condition:

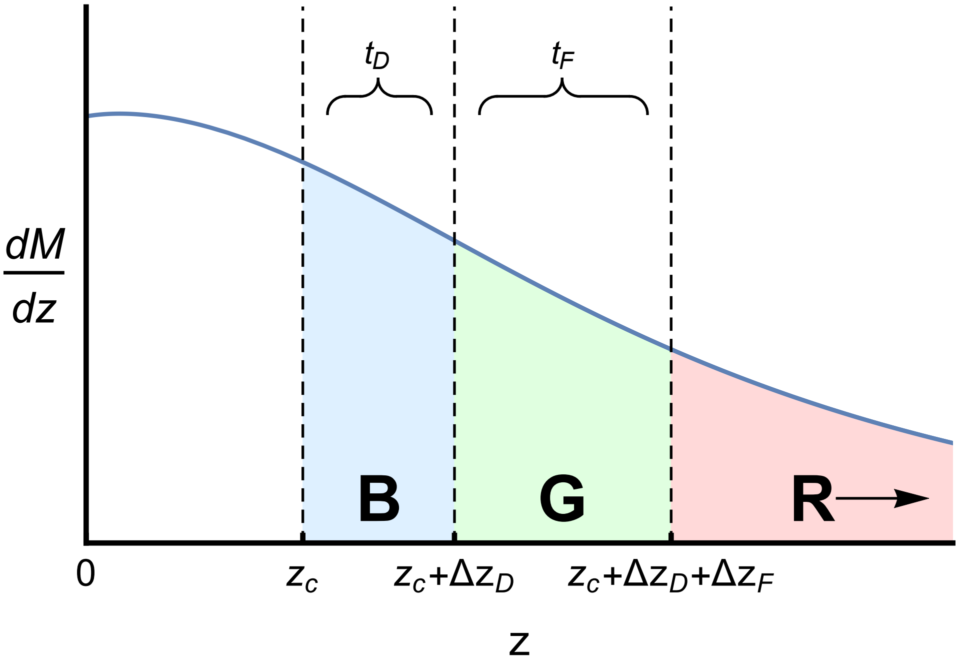

Figure B.2 Cluster mass accretion rate $\mathrm{d}M/\mathrm{d}z$ as a function of redshift, for a cluster observed at redshift z_c. The number of galaxies accreted over a given redshift interval is proportional to the area under the curve for that interval. Blue galaxies, being accreted no later than one t_D ago, have numbers proportional to the integral of the mass accretion rate between z_c and $z_c + \Delta z_D$, labeled B. Green galaxies have been in the cluster longer than one t_D but no longer than $t_D + t_F$ and so have been accreted over the interval between $z_c + \Delta z_D$ and $z_c + \Delta z_D + \Delta z_F$, labeled G. The number of red galaxies, R, is proportional to the integral of all mass accretion that occurred at redshifts greater than $z_c + \Delta z_D + \Delta z_F$.

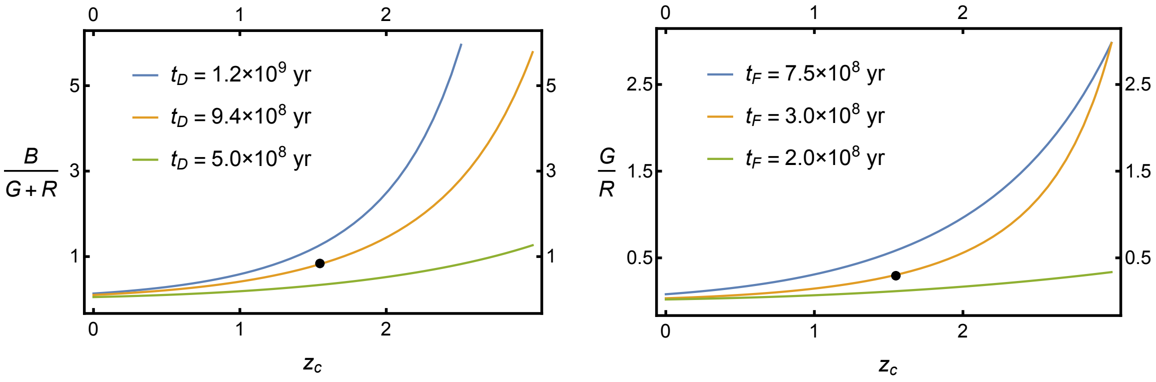

Figure B.3 Modeled evolution of the fractions $\frac{B}{G+R}$ and $\frac{G}{R}$. Lines show the evolution of these fractions for the indicated delay and fade times, t_D and t_F. Note that the fraction of blue galaxies increases with redshift, and with longer delay times, as expected. The black point indicates the measured value of these fractions for the stacked high-redshift sample, at the mean redshift of the sample, $z_c = 1.55$. From the left panel, it is clear that a delay time of $t_D = 9.4 \times 10^8$ yr is indicated in order to produce the observed fraction of blue galaxies. With this value for t_D we plot the redshift evolution of $\frac{G}{R}$ in the right panel, given that green galaxies were accreted between t_D and t_F ago, for selected values of t_F. A value of 3.0×10^8 yr is indicated for t_F.

$$\frac{\mathrm{d}M}{\mathrm{d}z} = \frac{-t_H}{46.1\ \mathrm{yr}} \times \left(\frac{1 + 1.11z}{1+z}\right)\left(\frac{M}{10^{12}\ \mathrm{M}_\odot}\right)^{1.1} \mathrm{M}_\odot \tag{B.1}$$

$$\frac{B}{G+R} = \frac{M(z_c) - M(z_c + \Delta z_D)}{M(z_c + \Delta z_D)} \tag{B.2}$$

$$\frac{B+G}{R} = \frac{M(z_c + \Delta z_D) - M(z_c + \Delta z_D + \Delta z_F)}{M(z_c + \Delta z_D + \Delta z_F)} \tag{B.3}$$

$$M(1.6) = 3 \times 10^{14}\ \mathrm{M}_\odot \tag{B.4}$$

Through Equations (B.1) – (B.4), the numbers of red, green, and blue galaxies at cluster redshift z_c constrain the delay and fade redshift intervals, Δz_D and Δz_F. For our purposes, we find it easiest to first solve the differential equation for $M(z)$ numerically with Mathematica using `NDSolve`. Knowing $M(z)$, it is then a matter of finding the redshift interval Δz_D that satisfies Equation B.2, which we accomplish with `FindRoot`. We repeat the process to then determine Δz_F from Equation B.3.

To illustrate the method, we plot the modeled evolution of the fractions $\frac{B}{G+R}$ and $\frac{G}{R}$ in Figure B.3 for selected values of t_D and t_F. From this plot, it is clear that the observed ratios of red, green, and blue galaxies constrain t_D and t_F.

Having determined Δz_D and Δz_F, we can apply standard cosmology to calculate the time intervals

$$\begin{aligned} t_D &= t_H \int_{z_c}^{z_c+\Delta z_D} \frac{\mathrm{d}z}{(1+z)\sqrt{\Omega_m(1+z)^3+\Omega_\Lambda}} \\ t_F &= t_H \int_{z_c+\Delta z_D}^{z_c+\Delta z_D+\Delta z_F} \frac{\mathrm{d}z}{(1+z)\sqrt{\Omega_m(1+z)^3+\Omega_\Lambda}} \end{aligned}$$

and thereby measure the quenching timescale, $t_Q = t_D + t_F$.

The technique we describe here relies on interpreting the integrated mass accretion history of a cluster, and so the resulting quenching timescales are time-averaged over the history of the cluster. This should not impact the results of this paper as the clusters we study here are still very young, but would need to be taken into consideration when applying this technique at low redshift.

B.1 Field-quenched Correction

Quenched galaxies exist in the field, and therefore some of the galaxies accreted by a cluster will already be quenched. If these galaxies are included when calculating t_Q, they will inflate the relative proportion of red galaxies, resulting in an apparently shorter quenching time. Correcting for this is a simple matter of calculating the fraction of galaxies that were quiescent when accreted, and subtracting them from the total number of red galaxies.

We start by calculating the quiescent fraction of field galaxies above the mass completeness limit of $10^{10.5}$ $\mathrm{M}_{\odot}$ as a function of redshift, $f_Q(z)$. Muzzin et al. (2013c) provides Schechter mass function fits to field galaxies in the COSMOS/UltraVISTA survey. These functions have the form

$$\Phi(M) = \ln 10 \times \Phi^{*} \times 10^{(M-M^{*})(1+\alpha)} \times \exp(-10^{(M-M^{*})})$$

and are parametrized by a normalization, Φ^{*}, a characteristic mass, M^{*}, and a low-mass-end slope, α. The masses M and M^{*} are logarithmic stellar masses of the form $M = \log_{10}(M_{star}/M_{\odot})$. Muzzin et al. (2013c) fits separate mass functions for star-forming and quiescent galaxies in seven redshift bins from $0.2 \leq z \leq 4.0$

From these mass functions we can define the field quiescent fraction $f_Q(z_i)$ at seven redshift points z_i,

$$f_Q(z_i) = \frac{\int_{10.5}^{\infty} \ \Phi_Q(M, z_i)\ \mathrm{d}M}{\int_{10.5}^{\infty} \ \Phi_Q(M, z_i)\ \mathrm{d}M + \int_{10.5}^{\infty} \ \Phi_A(M, z_i)\ \mathrm{d}M}$$

where $\Phi_Q(M, z_i)$ and $\Phi_A(M, z_i)$ are the quiescent and star-forming mass functions, respectively, and z_i is the mean redshift of the i^{th} redshift bin.

The fraction of quiescent field galaxies with masses above $10^{10.5}$ $\mathrm{M}_{\odot}$ evolves with cosmic time as the cluster accretes galaxies from the field. To determine the total fraction of quiescent field galaxies accreted over the lifetime of the cluster, we must integrate the galaxy accretion rate weighted by the field quiescent fraction. Therefore we interpolate $f_Q(z_i)$ between the seven redshift points by fitting 3$^{\rm rd}$-order polynomial curves between successive data points using the Mathematica function `Interpolation`. This creates a continuous and differentiable function $f_Q(z)$ suitable for integration.

Previously, we used the cluster mass accretion rate, $\mathrm{d}M/\mathrm{d}z$, as a proxy for the cluster galaxy accretion rate. The total accreted field quiescent fraction $f_{\rm Q,tot}(z)$ is therefore

$$f_{\rm Q,tot}(z) = \frac{\int_{-\infty}^{z} \mathrm{d}M/\mathrm{d}z' \; f_Q(z') \; \mathrm{d}z'}{\int_{-\infty}^{z} \mathrm{d}M/\mathrm{d}z' \; \mathrm{d}z'}. \tag{B.5}$$

where z is the redshift of the cluster. The evolution of $f_{\rm Q,tot}(z)$ and $f_Q(z)$ with redshift is shown in Figure B.4.

From Equation B.5, we can determine the fraction of quiescent galaxies in a cluster at redshift z that were already quenched at the time they were accreted. We therefore multiply the number of red galaxies in each cluster by $1 - f_{\rm Q,tot}(z_c)$ before applying Equations (B.1) – (B.4) and determining t_Q.

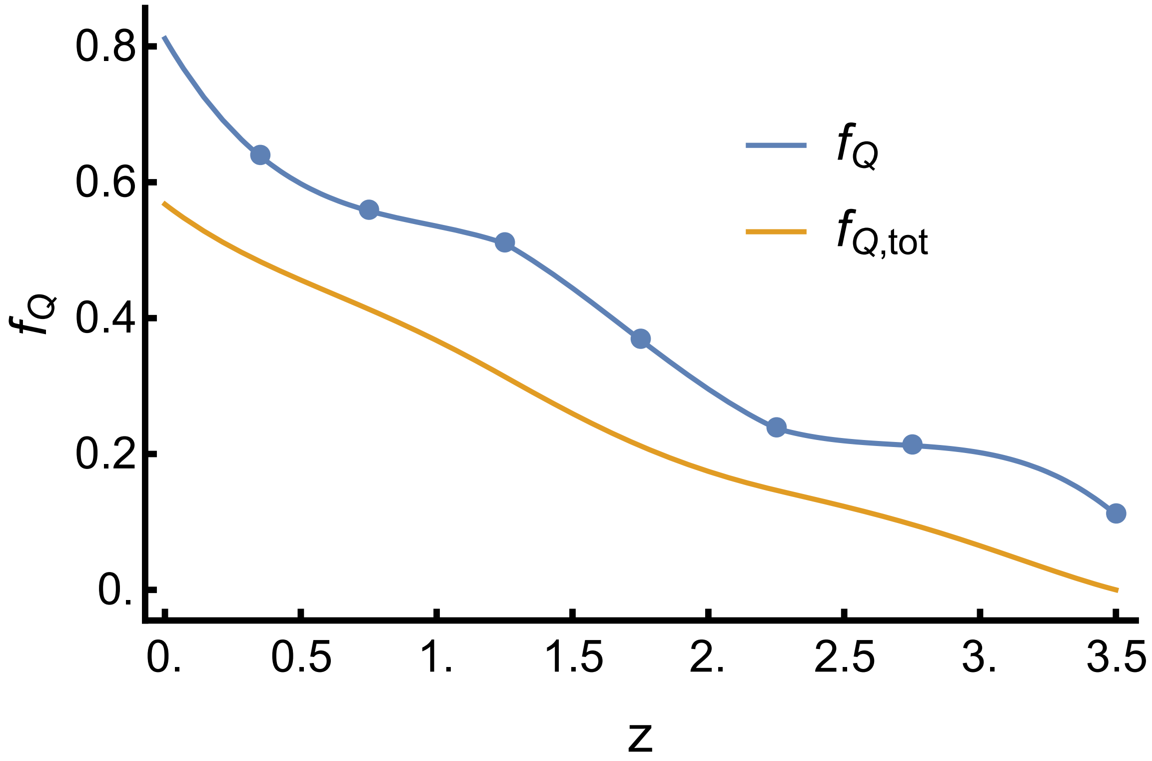

Figure B.4 Evolution of the field quiescent fraction with redshift. The field quiescent fraction is determined from the field mass function fits of Muzzin et al. (2013c) in seven redshift bins, for galaxies with masses $M \geq 10^{10.5}$ $\mathrm{M}_{\odot}$, plotted as points. The blue line depicts a function interpolated from the seven points. The orange line is the integrated mass accretion rate of a cluster weighted by the field quiescent fraction, or the total fraction of accreted quiescent field galaxies.

Appendix C

Where is the Green Valley in UVJ-Space?

Rest-frame *UVJ* color-color selection is frequently used to distinguish quiescent and star-forming galaxies, by dividing the space of rest-frame U-V versus V-J colors into a star-forming and a quiescent region. The cuts that define these regions have been empirically derived by Williams et al. (2009), being tuned to maximally reflect the bimodality of galaxy populations out to $z \sim 2.5$. The *UVJ* method accounts for dust reddening by using two colors that differ in their sensitivity to star formation and dust, to break the degeneracy between old-and-quiescent and star-forming-and-dusty galaxies. In Figure C.1, we plot the *UVJ* color-color diagram for all cluster members in our sample.

The *UVJ* method parallels the selection used in Section 3.2.2 to classify quiescent (red), star-forming (blue), and intermediate (green) galaxies. A natural question is whether similar values for t_Q are obtained when galaxies are classified according to their *UVJ* colors

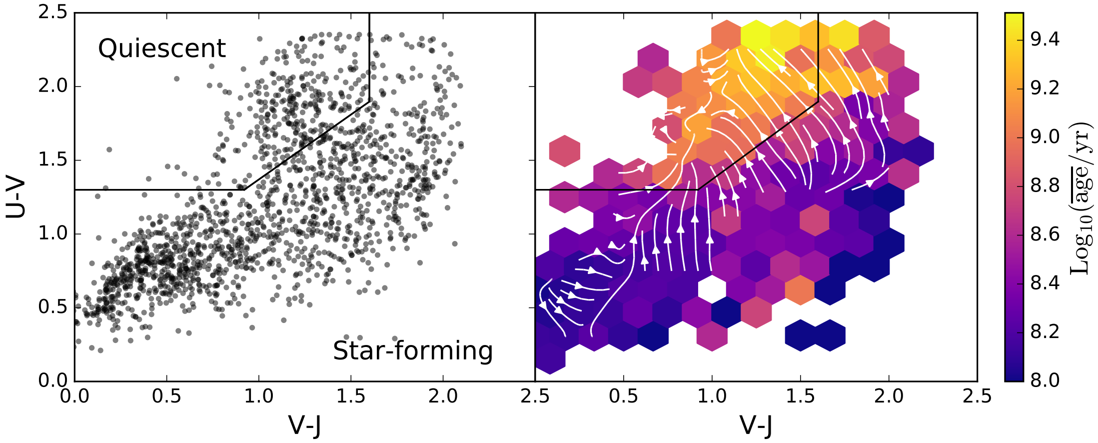

Figure C.1 Left panel: Rest-frame *U*-*V* versus *V*-*J* color-color diagram for all cluster members in the high-redshift sample. Right panel: 2D histogram of mean binned galaxy ages in rest-frame *UVJ* space. The ages depicted here are derived from SED fitting (see Section 3.1.4). The vector field plotted in white depicts the negative gradient of the mean binned ages, representing a possible approximation of evolutionary tracks. Almost all of these tracks depict galaxies moving from the star-forming to the quiescent bin, and therefore quenching (intermediate) galaxies. Note that these tracks take paths that cross all portions of the boundary between the star-forming and quiescent regions.

rather than the dust-corrected color-magnitude method. In this appendix we will perform this comparison and report the results. This subject will be expanded on in a letter (Foltz 2017, in prep).

Equations (B.1) – (B.4) are written in terms of the observed number of red, green, and blue galaxies in a cluster. The UVJ method (as it is commonly used) however only classifies galaxies as either star-forming or quiescent. The principal difficulty in identifying an intermediate UVJ region lies in the fact that a galaxy's location in UVJ space is strongly dependent on both its star formation rate and its dust reddening.

For example, a galaxy in the upper-right region of the star-forming bin is both star-forming and very dust-reddened. If it quenches, after some time it will end up in the quiescent bin, where star formation rates are low and dust-reddening is low. The galaxy will need to decrease in dust-reddening as it decreases its star formation rate, and its precise trajectory in UVJ space will depend on the details of how both of these values change in time. The UVJ green valley is therefore defined not only by intermediate star formation rates, but also by intermediate dust-reddening values.

This point is illustrated further in Figure C.1. The right panel of this figure depicts mean binned ages of galaxies in rest-frame UVJ space, and the gradient of these mean ages is shown as a white vector field. Intermediate galaxies, by definition, are those moving from the star-forming to the quiescent bin, and the age bins indicate many possible paths such galaxies might take as they age. This makes it difficult to know where to look in UVJ space for galaxies that have recently shut off their star formation, although it is natural to suppose that they must lie along the boundary of the quiescent and star-forming regions, especially since that boundary was drawn precisely to separate these two populations. At the very least, there is reasonable doubt about the specific evolutionary tracks of quenching galaxies in a *UVJ* diagram, in light of the lack of a prescription for modeling how dust reddening will change following the cessation of star formation. In contrast, the evolution of quenched galaxies in Figure 3.4 is unambiguous, allowing a straightforward identification of blue, green, and red galaxies.

There have been some attempts to augment the *UVJ* method with the addition of a third bin. Whitaker et al. (2012) subdivides the quiescent bin into young and old sections, in light of the fact that the color sequence of *UVJ*-quiescent galaxies is driven by the ages of their stellar populations (Whitaker et al., 2010, 2012). We wish to emphasize that this *V-J* cut is successful for the purposes of Whitaker et al. (2010, 2012) in that it identifies young, quiescent galaxies. We simply caution against others interpreting this cut as a general intermediate bin, as the age-color relation does not extend to the full population of galaxies, where the picture is complicated by dust reddening. There is a difference between young quiescent galaxies and intermediate galaxies in general. For the purposes of our quenching model, it is necessary to identify intermediate galaxies that have just left the star-forming blue cloud.

In a different approach, by adapting the method described in Appendix B, we can measure a quenching time using only numbers of star-forming and quiescent galaxies. The general approach is to omit the number of intermediate galaxies (G) by assuming they are included in the number of star-forming galaxies (B), under the assumption that their declining but nonzero star formation rates will count them among the star-forming galaxies in the UVJ diagram. We then reformulate our equations under this assumption as follows: the loss of the known variable G comes at the cost being unable to solve for t_D and t_F separately, and so we solve for t_Q directly without separating it into delay and fade times.

Mathematically, if we apply the follow transformation:

$$\begin{aligned} R' &= R \qquad & t'_D &= t_D + t_F = t_Q \\ G' &= 0 \qquad & t'_F &= 0 \\ B' &= B + G \end{aligned}$$

then the earlier integral relations simplify to

$$\frac{B'}{R'} = \frac{\displaystyle\int_{z_c+\Delta z_Q}^{z_c} \mathrm{d}M/\mathrm{d}z \ \mathrm{d}z}{\displaystyle\int_{\infty}^{z_c+\Delta z_Q} \mathrm{d}M/\mathrm{d}z \ \mathrm{d}z}$$

where Δz_Q is the redshift interval that spans one quenching time t_Q, B' is the number of UVJ-star-forming galaxies, and R' is the number of UVJ-quiescent galaxies. From here, the arguments of Appendix B follow, and we can use the UVJ-derived number counts to constrain a quenching time with the following set of equations:

$$\begin{aligned} &\frac{\mathrm{d}M}{\mathrm{d}z} = \frac{-t_H}{46.1\ \mathrm{yr}} \times \left(\frac{1+1.11z}{1+z}\right)\left(\frac{M}{10^{12}\ \mathrm{M}_\odot}\right)^{1.1} \mathrm{M}_\odot \\ &M(1.6) = 3 \times 10^{14}\ \mathrm{M}_\odot \\ &\frac{B}{R} = \frac{M(z_c) - M(z_c + \Delta z_Q)}{M(z_c + \Delta z_Q)} \end{aligned}$$

Table C.1. Effect of UVJ selection on inferred quenching timescales

Sample	N	$\bar{z}$	Quiescent	Star-Forming	UVJ $t_Q{}^a$ (Gyr)	RGB $t_Q{}^b$ (Gyr)
GCLASS	10	1.04	187	58	$1.11^{+0.16}_{-0.20}$	$1.50^{+0.19}_{-0.18}$
SpARCS high-redshift	4	1.55	85	75	$1.16^{+0.12}_{-0.14}$	$1.24^{+0.23}_{-0.20}$

[a] Quenching timescale derived using UVJ classification

[b] Quenching timescale derived using dust-corrected U-B color-magnitude classification, for comparison (see Section 3.2.2)

As in Section 3.3, we stack each cluster sample by taking the total numbers of UVJ-quiescent and UVJ-star-forming galaxies at the mean redshift of both cluster samples. These number counts then constrain a quenching timescale as described in Appendix B. Poisson counting statistics and a Monte Carlo simulation with 200 iterations provides the 68% confidence interval, as described in Section 3.2.5. The results are reported in Table C.1, alongside the results of the main analysis for comparison.

The quenching timescales derived by both methods very nearly agree within uncertainties. For the GCLASS sample at $z = 1.0$, we find $1.11^{+0.16}_{-0.20}$ Gyr, compared to ~ 1.5 Gyr for the RGB classification method. In the higher-redshift sample at $z = 1.55$, we find $1.16^{+0.12}_{-0.14}$ Gyr, compared to ~ 1.2 Gyr for the RGB method. Our error bars are likely under-estimated when adapting the Monte Carlo method to the UVJ classification, as it describes uncertainty in only two variables (RB) instead of the RGB method's full three. The UVJ method yields a t_Q that is lower in both cases because it finds a slightly higher passive fraction. This is indicative of the way both classification schemes treat intermediate galaxies, which are necessarily split between the UVJ-star-forming and UVJ-quiescent categories.

Bibliography

Abell, G. O., Corwin, Jr., H. G., & Olowin, R. P. 1989, ApJS, 70, 1

Andrews, B. H., & Martini, P. 2013, ApJ, 765, 140

Appenzeller, I., Fricke, K., Fürtig, W., et al. 1998, The Messenger, 94, 1

Arnouts, S., Walcher, C. J., Le Fèvre, O., et al. 2007, A&A, 476, 137

Ascaso, B., Benítez, N., Fernández-Soto, A., et al. 2015, MNRAS, 452, 549

Baldry, I. K., Balogh, M. L., Bower, R. G., et al. 2006, MNRAS, 373, 469

Baldry, I. K., Glazebrook, K., Brinkmann, J., et al. 2004a, ApJ, 600, 681

—. 2004b, ApJ, 600, 681

Balogh, M. L., McGee, S. L., Mok, A., et al. 2014, MNRAS, 443, 2679

—. 2016, MNRAS, 456, 4364

Barnes, J. E. 1992, ApJ, 393, 484

Bassett, R., Papovich, C., Lotz, J. M., et al. 2013, ApJ, 770, 58

Bauermeister, A., Blitz, L., & Ma, C.-P. 2010, ApJ, 717, 323

Beers, T. C., Flynn, K., & Gebhardt, K. 1990, AJ, 100, 32

Bekki, K., & Couch, W. J. 2011, MNRAS, 415, 1783

Bell, E. F., Wolf, C., Meisenheimer, K., et al. 2004a, ApJ, 608, 752

—. 2004b, ApJ, 608, 752

Bernardi, M., Sheth, R. K., Annis, J., et al. 2003, AJ, 125, 1866

Bertin, E., & Arnouts, S. 1996, A&AS, 117, 393

Bertin, E., Mellier, Y., Radovich, M., et al. 2002, in Astronomical Society of the Pacific Conference Series, Vol. 281, Astronomical Data Analysis Software and Systems XI, ed. D. A. Bohlender, D. Durand, & T. H. Handley, 228

Blakeslee, J. P., Franx, M., Postman, M., et al. 2003a, eapj@ApJLetters, 596, L143

—. 2003b, eapj@ApJLetters, 596, L143

Blanton, M. R. 2006, ApJ, 648, 268

Blanton, M. R., & Moustakas, J. 2009, ARA&A, 47, 159

Blanton, M. R., & Roweis, S. 2007, AJ, 133, 734

Bleem, L. E., Stalder, B., de Haan, T., et al. 2015, ApJS, 216, 27

Blumenthal, G. R., Faber, S. M., Primack, J. R., & Rees, M. J. 1984, Nature, 311, 517

Borch, A., Meisenheimer, K., Bell, E. F., et al. 2006, A&A, 453, 869

Bower, R. G., Kodama, T., & Terlevich, A. 1998, MNRAS, 299, 1193

Bower, R. G., Lucey, J. R., & Ellis, R. S. 1992, MNRAS, 254, 601

Brammer, G. B., van Dokkum, P. G., & Coppi, P. 2008, ApJ, 686, 1503

Brammer, G. B., Whitaker, K. E., van Dokkum, P. G., et al. 2011, ApJ, 739, 24

Brammer, G. B., van Dokkum, P. G., Franx, M., et al. 2012, ApJS, 200, 13

Brown, M. J. I., Dey, A., Jannuzi, B. T., et al. 2007, ApJ, 654, 858

Bruzual, G., & Charlot, S. 2003a, MNRAS, 344, 1000

—. 2003b, MNRAS, 344, 1000

Bundy, K., Ellis, R. S., Conselice, C. J., et al. 2006, ApJ, 651, 120

Byrd, G., & Valtonen, M. 1990, ApJ, 350, 89

Calzetti, D. 2001, PASP, 113, 1449

Cardamone, C. N., Urry, C. M., Schawinski, K., et al. 2010, eapj@ApJLetters, 721, L38

Cerulo, P., Couch, W. J., Lidman, C., et al. 2016, MNRAS, 457, 2209

—. 2017, MNRAS, 472, 254

Chabrier, G. 2003, eapj@ApJLetters, 586, L133

Childress, M. J., Lidman, C., Davis, T. M., et al. 2017, MNRAS, 472, 273

Cimatti, A., Brusa, M., Talia, M., et al. 2013, eapj@ApJLetters, 779, L13

Coil, A. L., Newman, J. A., Croton, D., et al. 2008, ApJ, 672, 153

Cole, S., Lacey, C. G., Baugh, C. M., & Frenk, C. S. 2000, MNRAS, 319, 168

Cooper, M. C., Newman, J. A., Croton, D. J., et al. 2006, MNRAS, 370, 198

Cooper, M. C., Newman, J. A., Coil, A. L., et al. 2007, MNRAS, 376, 1445

Davis, M., Efstathiou, G., Frenk, C. S., & White, S. D. M. 1985, ApJ, 292, 371

De Lucia, G., Weinmann, S., Poggianti, B. M., Aragón-Salamanca, A., & Zaritsky, D. 2012, MNRAS, 423, 1277

DeGroot, A. J. 2016, PhD thesis, University of California Riverside

Demarco, R., Rosati, P., Lidman, C., et al. 2005, A&A, 432, 381

—. 2007, ApJ, 663, 164

Demarco, R., Wilson, G., Muzzin, A., et al. 2010, ApJ, 711, 1185

Donahue, M., Mack, J., Scharf, C., et al. 2001, eapj@ApJLetters, 552, L93

Dressler, A. 1980, ApJ, 236, 351

Eisenhardt, P. R. M., Brodwin, M., Gonzalez, A. H., et al. 2008, ApJ, 684, 905

Ellis, R. S., Smail, I., Dressler, A., et al. 1997, ApJ, 483, 582

Erb, D. K., Shapley, A. E., Pettini, M., et al. 2006, ApJ, 644, 813

Evrard, A. E., Bialek, J., Busha, M., et al. 2008, ApJ, 672, 122

Faber, S. M., Willmer, C. N. A., Wolf, C., et al. 2007, ApJ, 665, 265

Fadda, D., Girardi, M., Giuricin, G., Mardirossian, F., & Mezzetti, M. 1996, ApJ, 473, 670

Fakhouri, O., Ma, C.-P., & Boylan-Kolchin, M. 2010, MNRAS, 406, 2267

Fazio, G. G., Hora, J. L., Allen, L. E., et al. 2004, ApJS, 154, 10

Fillingham, S. P., Cooper, M. C., Wheeler, C., et al. 2015, MNRAS, 454, 2039

Finlator, K., & Davé, R. 2008, MNRAS, 385, 2181

Foltz, R., Rettura, A., Wilson, G., et al. 2015, ApJ, 812, 138

Font, A. S., Johnston, K. V., Ferguson, A. M. N., et al. 2008a, ApJ, 673, 215

Font, A. S., Bower, R. G., McCarthy, I. G., et al. 2008b, MNRAS, 389, 1619

Ford, H., Postman, M., Blakeslee, J. P., et al. 2004, in Astrophysics and Space Science Library, Vol. 319, Penetrating Bars Through Masks of Cosmic Dust, ed. D. L. Block, I. Puerari, K. C. Freeman, R. Groess, & E. K. Block (Springer Netherlands), 459

Fossati, M., Wilman, D. J., Mendel, J. T., et al. 2017, ApJ, 835, 153

Franx, M., & van Dokkum, P. G. 2001, in Astronomical Society of the Pacific Conference Series, Vol. 230, Galaxy Disks and Disk Galaxies, ed. J. G. Funes & E. M. Corsini, 581–588

Gal, R. R., de Carvalho, R. R., Odewahn, S. C., Djorgovski, S. G., & Margoniner, V. E. 2000, AJ, 119, 12

Gal, R. R., Lemaux, B. C., Lubin, L. M., Kocevski, D., & Squires, G. K. 2008, ApJ, 684, 933

Genzel, R., Tacconi, L. J., Lutz, D., et al. 2015, ApJ, 800, 20

George, M. R., Leauthaud, A., Bundy, K., et al. 2011, ApJ, 742, 125

Gioia, I. M., & Luppino, G. A. 1994a, ApJS, 94, 583

—. 1994b, ApJS, 94, 583

Girardi, M., Biviano, A., Giuricin, G., Mardirossian, F., & Mezzetti, M. 1993, ApJ, 404, 38

Gladders, M. D., & Yee, H. K. C. 2000, AJ, 120, 2148

—. 2005, ApJS, 157, 1

Gnedin, O. Y., Kravtsov, A. V., Klypin, A. A., & Nagai, D. 2004, ApJ, 616, 16

Gobat, R., Daddi, E., Béthermin, M., et al. 2015, A&A, 581, A56

Gott, III, J. R., & Rees, M. J. 1975a, A&A, 45, 365

—. 1975b, A&A, 45, 365

Grogin, N. A., Kocevski, D. D., Faber, S. M., et al. 2011, ApJS, 197, 35

Gunn, J. E., & Gott, III, J. R. 1972, ApJ, 176, 1

Gunn, J. E., Hoessel, J. G., & Oke, J. B. 1986, ApJ, 306, 30

Haines, C. P., Pereira, M. J., Smith, G. P., et al. 2015, ApJ, 806, 101

Hasselfield, M., Hilton, M., Marriage, T. A., et al. 2013, J. Cosmology Astropart. Phys., 7, 8

Henriques, B. M. B., White, S. D. M., Thomas, P. A., et al. 2017, MNRAS, 469, 2626

Hicks, A. K., Pratt, G. W., Donahue, M., et al. 2013, MNRAS, 431, 2542

Hilton, M., Stanford, S. A., Stott, J. P., et al. 2009, ApJ, 697, 436

Holden, B. P., Franx, M., Illingworth, G. D., et al. 2006, eapj@ApJLetters, 642, L123

Huertas-Company, M., Aguerri, J. A. L., Tresse, L., et al. 2010, A&A, 515, A3

Kauffmann, G., White, S. D. M., Heckman, T. M., et al. 2004, MNRAS, 353, 713

Kelly, B. C. 2007, ApJ, 665, 1489

Kewley, L. J., & Ellison, S. L. 2008, ApJ, 681, 1183

Kodama, T., & Arimoto, N. 1997, A&A, 320, 41

Koekemoer, A. M., Faber, S. M., Ferguson, H. C., et al. 2011, ApJS, 197, 36

Kravtsov, A. V., & Borgani, S. 2012, ARA&A, 50, 353

Kriek, M., van Dokkum, P. G., Labbé, I., et al. 2009, ApJ, 700, 221

Kriek, M., Labbé, I., Conroy, C., et al. 2010, eapj@ApJLetters, 722, L64

Kriek, M., Shapley, A. E., Reddy, N. A., et al. 2014, ArXiv e-prints, arXiv:1412.1835

Kuijken, K. 2008, A&A, 482, 1053

Lacey, C., & Cole, S. 1993, MNRAS, 262, 627

Larson, R. B., Tinsley, B. M., & Caldwell, C. N. 1980, ApJ, 237, 692

Lavery, R. J., & Henry, J. P. 1988, ApJ, 330, 596

Lidman, C., Suherli, J., Muzzin, A., et al. 2012a, MNRAS, 427, 550

—. 2012b, MNRAS, 427, 550

Lidman, C., Iacobuta, G., Bauer, A. E., et al. 2013, MNRAS, 433, 825

Lidman, C. E., & Peterson, B. A. 1996, AJ, 112, 2454

Lonsdale, C. J., Smith, H. E., Rowan-Robinson, M., et al. 2003, PASP, 115, 897

Maiolino, R., Nagao, T., Grazian, A., et al. 2008, in Astronomical Society of the Pacific Conference Series, Vol. 396, Formation and Evolution of Galaxy Disks, ed. J. G. Funes & E. M. Corsini, 409

Maraston, C. 2005, MNRAS, 362, 799

McCarthy, I. G., Frenk, C. S., Font, A. S., et al. 2008, MNRAS, 383, 593

McGee, S. L., Balogh, M. L., Bower, R. G., Font, A. S., & McCarthy, I. G. 2009, MNRAS, 400, 937

McGee, S. L., Balogh, M. L., Wilman, D. J., et al. 2011, MNRAS, 413, 996

McGee, S. L., Bower, R. G., & Balogh, M. L. 2014, MNRAS, 442, L105

McLean, I. S., Steidel, C. C., Epps, H., et al. 2010, in Proc. SPIE, Vol. 7735, Ground-based and Airborne Instrumentation for Astronomy III, 77351E–77351E–12

McLean, I. S., Steidel, C. C., Epps, H. W., et al. 2012, in Proc. SPIE, Vol. 8446, Ground-based and Airborne Instrumentation for Astronomy IV, 84460J

Mei, S., Holden, B. P., Blakeslee, J. P., et al. 2006, ApJ, 644, 759

—. 2009, ApJ, 690, 42

Menci, N., Rosati, P., Gobat, R., et al. 2008, ApJ, 685, 863

Merritt, D. 1983, ApJ, 264, 24

Mok, A., Balogh, M. L., McGee, S. L., et al. 2014, MNRAS, 438, 3070

Moore, B., Katz, N., Lake, G., Dressler, A., & Oemler, A. 1996, Nature, 379, 613

Moore, B., Lake, G., & Katz, N. 1998, ApJ, 495, 139

Moresco, M., Pozzetti, L., Cimatti, A., et al. 2013, A&A, 558, A61

Muzzin, A., Wilson, G., Demarco, R., et al. 2013a, ApJ, 767, 39

Muzzin, A., Wilson, G., Yee, H. K. C., et al. 2009, ApJ, 698, 1934

—. 2012, ApJ, 746, 188

Muzzin, A., Marchesini, D., Stefanon, M., et al. 2013b, ApJS, 206, 8

—. 2013c, ApJ, 777, 18

Muzzin, A., van der Burg, R. F. J., McGee, S. L., et al. 2014a, ApJ, 796, 65

—. 2014b, ApJ, 796, 65

Nantais, J. B., van der Burg, R. F. J., Lidman, C., et al. 2016, A&A, 592, A161

Nantais, J. B., Muzzin, A., van der Burg, R. F. J., et al. 2017, MNRAS, 465, L104

Narlikar, J. V., & Padmanabhan, T. 2001, ARA&A, 39, 211

Navarro, J. F., Frenk, C. S., & White, S. D. M. 1995, MNRAS, 275, 56

Newman, A. B., Ellis, R. S., Andreon, S., et al. 2014, ApJ, 788, 51

Noble, A. G., Webb, T. M. A., Muzzin, A., et al. 2013, ApJ, 768, 118

Oke, J. B., & Gunn, J. E. 1983, ApJ, 266, 713

Oman, K. A., & Hudson, M. J. 2016, MNRAS, 463, 3083

Ostrander, E. J., Nichol, R. C., Ratnatunga, K. U., & Griffiths, R. E. 1998, AJ, 116, 2644

Paccagnella, A., Vulcani, B., Poggianti, B. M., et al. 2016, eapj@ApJLetters, 816, L25

—. 2017, ApJ, 838, 148

Papovich, C. 2008, ApJ, 676, 206

Papovich, C., Momcheva, I., Willmer, C. N. A., et al. 2010, ApJ, 716, 1503

Patel, S. G., Holden, B. P., Kelson, D. D., et al. 2012, eapj@ApJLetters, 748, L27

Patel, S. G., Holden, B. P., Kelson, D. D., Illingworth, G. D., & Franx, M. 2009, eapj@ApJLetters, 705, L67

Peebles, P. J. E. 2002, in Astronomical Society of the Pacific Conference Series, Vol. 283, A New Era in Cosmology, ed. N. Metcalfe & T. Shanks, 351

Peeples, M. S., & Shankar, F. 2011, MNRAS, 417, 2962

Peng, Y.-j., Lilly, S. J., Kovač, K., et al. 2010, ApJ, 721, 193

Planck Collaboration, Ade, P. A. R., Aghanim, N., et al. 2014, A&A, 571, A29

Presotto, V., Iovino, A., Scodeggio, M., et al. 2012, A&A, 539, A55

Press, W. H., & Schechter, P. 1974, ApJ, 187, 425

Quadri, R., van Dokkum, P., Gawiser, E., et al. 2007, ApJ, 654, 138

Quilis, V., Moore, B., & Bower, R. 2000, Science, 288, 1617

Reichardt, C. L., Stalder, B., Bleem, L. E., et al. 2013, ApJ, 763, 127

Rettura, A., Rosati, P., Strazzullo, V., et al. 2006, A&A, 458, 717

Rettura, A., Rosati, P., Nonino, M., et al. 2010, ApJ, 709, 512

Rettura, A., Mei, S., Stanford, S. A., et al. 2011, ApJ, 732, 94

Rettura, A., Martinez-Manso, J., Stern, D., et al. 2014, ApJ, 797, 109

Romeo, A. D., Napolitano, N. R., Covone, G., et al. 2008, MNRAS, 389, 13

Romer, A. K., Nichol, R. C., Holden, B. P., et al. 2000, ApJS, 126, 209

Rosati, P., della Ceca, R., Norman, C., & Giacconi, R. 1998, eapj@ApJLetters, 492, L21

Rudd, D. H., Zentner, A. R., & Kravtsov, A. V. 2008, ApJ, 672, 19

Rudnick, G. H., Tran, K.-V., Papovich, C., Momcheva, I., & Willmer, C. 2012, ApJ, 755, 14

Rykoff, E. S., McKay, T. A., Becker, M. R., et al. 2008, ApJ, 675, 1106

Rykoff, E. S., Rozo, E., Busha, M. T., et al. 2014, ApJ, 785, 104

Saintonge, A., Kauffmann, G., Kramer, C., et al. 2011, MNRAS, 415, 32

Scharf, C. A., Jones, L. R., Ebeling, H., et al. 1997, ApJ, 477, 79

Schawinski, K., Urry, C. M., Simmons, B. D., et al. 2014, MNRAS, 440, 889

Schlafly, E. F., & Finkbeiner, D. P. 2011, ApJ, 737, 103

Schlegel, D. J., Finkbeiner, D. P., & Davis, M. 1998, ApJ, 500, 525

Snyder, G. F., Brodwin, M., Mancone, C. M., et al. 2012, ApJ, 756, 114

Springel, V., Frenk, C. S., & White, S. D. M. 2006, Nature, 440, 1137

Springel, V., White, S. D. M., Jenkins, A., et al. 2005, Nature, 435, 629

Stanford, S. A., Eisenhardt, P. R., Brodwin, M., et al. 2005, eapj@ApJLetters, 634, L129

Stanford, S. A., Brodwin, M., Gonzalez, A. H., et al. 2012, ApJ, 753, 164

Strateva, I., Ivezić, Ž., Knapp, G. R., et al. 2001, AJ, 122, 1861

Strazzullo, V., Rosati, P., Pannella, M., et al. 2010, A&A, 524, A17

Strazzullo, V., Gobat, R., Daddi, E., et al. 2013, ApJ, 772, 118

Tacconi, L. J., Genzel, R., Saintonge, A., et al. 2017, ArXiv e-prints, arXiv:1702.01140

Tanaka, M., Finoguenov, A., Lilly, S. J., et al. 2012, PASJ, 64, 22

Taranu, D. S., Hudson, M. J., Balogh, M. L., et al. 2014, MNRAS, 440, 1934

Thomas, P. A., & Couchman, H. M. P. 1992, MNRAS, 257, 11

Tinker, J. L., & Wetzel, A. R. 2010, ApJ, 719, 88

Toomre, A., & Toomre, J. 1972, ApJ, 178, 623

Tremonti, C. A., Heckman, T. M., Kauffmann, G., et al. 2004, ApJ, 613, 898

van der Burg, R. F. J., Muzzin, A., Hoekstra, H., et al. 2014, A&A, 561, A79

—. 2013a, A&A, 557, A15

—. 2013b, A&A, 557, A15

van Dokkum, P. G., Franx, M., Fabricant, D., Illingworth, G. D., & Kelson, D. D. 2000, ApJ, 541, 95

van Dokkum, P. G., Franx, M., Kelson, D. D., et al. 1998, ApJ, 500, 714

Vazdekis, A., Kuntschner, H., Davies, R. L., et al. 2001, eapj@ApJLetters, 551, L127

Vulcani, B., De Lucia, G., Poggianti, B. M., et al. 2014, ApJ, 788, 57

Weinberg, D. H., Davé, R., Katz, N., & Hernquist, L. 2004, ApJ, 601, 1

Weinmann, S. M., Kauffmann, G., von der Linden, A., & De Lucia, G. 2010, MNRAS, 406, 2249

Weinmann, S. M., Lisker, T., Guo, Q., Meyer, H. T., & Janz, J. 2011, MNRAS, 416, 1197

Werner, M. W., Roellig, T. L., Low, F. J., et al. 2004, ApJS, 154, 1

Wetzel, A. R., Tinker, J. L., Conroy, C., & van den Bosch, F. C. 2013, MNRAS, 432, 336

Wheeler, C., Phillips, J. I., Cooper, M. C., Boylan-Kolchin, M., & Bullock, J. S. 2014, MNRAS, 442, 1396

Whitaker, K. E., Kriek, M., van Dokkum, P. G., et al. 2012, ApJ, 745, 179

Whitaker, K. E., van Dokkum, P. G., Brammer, G., et al. 2010, ApJ, 719, 1715

Whitaker, K. E., Labbé, I., van Dokkum, P. G., et al. 2011, ApJ, 735, 86

Whitaker, K. E., van Dokkum, P. G., Brammer, G., et al. 2013, eapj@ApJLetters, 770, L39

White, S. D. M., & Frenk, C. S. 1991, ApJ, 379, 52

White, S. D. M., & Rees, M. J. 1978, MNRAS, 183, 341

Williams, R. J., Quadri, R. F., Franx, M., van Dokkum, P., & Labbé, I. 2009, ApJ, 691, 1879

Wilson, G., Muzzin, A., Yee, H. K. C., et al. 2009, ApJ, 698, 1943

Wuyts, S., Labbé, I., Franx, M., et al. 2007, ApJ, 655, 51

Wylezalek, D., Galametz, A., Stern, D., et al. 2013, ApJ, 769, 79

York, D. G., Adelman, J., Anderson, Jr., J. E., et al. 2000, AJ, 120, 1579

Yuan, F., Tucker, B. E., Lidman, C., et al. 2015, The Astronomer's Telegram, 8464

Zeimann, G. R., Stanford, S. A., Brodwin, M., et al. 2012, ApJ, 756, 115